

**Parametric Study on Moment-Rotation
Characteristics of Reverse Channel Connections
(RCC) to Tubular Columns**

Hashem Al Hendi

Submitted to the
Institute of Graduate Studies and Research
in Partial fulfillment of the requirements for the degree of

Doctor of Philosophy
in
Civil Engineering

Eastern Mediterranean University
February 2015
Gazimağusa, North Cyprus

Approval of the Institute of Graduate Studies and Research

Prof.Dr Serhan Çiftçiođlu
Director

I certify that this thesis satisfies the requirements as a thesis for the degree of Doctor of Philosophy in Civil Engineering.

Prof. Dr. Özgür Eren
Chair, Department of Civil Engineering

We verify that we have read this thesis and that in our opinion it is fully adequate in scope and quality as a thesis for the degree of Doctor of Philosophy in Civil Engineering.

Asst. Prof. Dr. Mürüde Çelikađ
Supervisor

Examining Committee

1. Prof. Dr. Ayşe Dalođlu

2. Prof. Dr. Gülay Altay

3. Asst. Prof. Dr. Giray Özay

4. Asst. Prof. Dr. Mürüde Çelikađ

5. Asst. Pror. Dr. Serhan Şensoy

ABSTRACT

The significance of this parametric study initiates from the need for further understanding of the behaviour of semi-rigid/partial-strength I-beam to tubular column connections. This research attempted to gain a qualitative understanding of the influence of the geometrical configurations and materials properties of reverse channel connections (RCC) on the moment-rotation ($M-\phi$) response. It also introduces a double reverse channel connection (DRCC), where the reverse channel is split into two pieces, by leaving a gap in between, for better access to bolts. Hence, ABAQUS (v.6.12) software was used to develop three-dimensional (3-D) FE models for 206 specimens. The FE models developed were validated against the experimental results available from literature where 268 FE models were used for sensitivity analysis. The main emphasis of this research was on the stiffness, strength, sources of deformability, rotational capacity and failure mechanisms of the RCC. Based on the results of numerical $M-\phi$ curves, a standardized moment-rotation function for reverse channel flush end-plate connection (RCC) was introduced. This function is expressed in terms of the geometric parameters for the purposes of either predicting the connection behavior or incorporating the behavior into a frame analysis computer program. Out of the six currently available functions, the Kishi-Chen and Richard-Abbott models were proved appropriate for fitting experimental $M-\phi$ data for RCC. The two functions were successfully used in this parametric study to express the relationships for 140 specimens, where the analytical and predicted data are in very good agreement. However, the results of the fitted functions indicate that the dimensionless form of Richard-Abbott function provides more accuracy than Kishi-Chen function. Furthermore, the comparison of Eurocode-

3 model with numerical $M-\phi$ curves illustrated a significant overestimation of the knee region behaviour for most of the cases, particularly for RCC with low initial stiffness.

Keywords: reverse channel, double reverse channel, moment–rotation curve, tubular column, HSS, stiffness, moment capacity, rotational capacity, standardized function, Kishi-Chen model, Richard-Abbott model.

ÖZ

Bu parametrik çalışmanın önemi yarı rijid/kısmi mukavemetli I-kirişinin boru kolona bağlantısının davranışını daha iyi anlama ihtiyacından kaynaklanmaktadır. Bu araştırma girişiminin nedeni geometrik biçimlerin ve malzeme özelliklerinin ters kanal bağlantısı (TKB) moment-rotasyon ($M-\phi$) tepkisi üzerindeki etkilerini nitelikli olarak anlamak için yapılmıştır. Ayrıca çift ters kanal bağlantısı (ÇTKB) bu çalışmada ilk kez sunulmuştur. Bu bağlantıda, civatalara daha kolay erişim için, ters kanal iki parçaya bölünmüş ve bu parçalar arasında bir boşluk bırakılmıştır. Bundan dolayı ABAQUS (v.6.12) yazılımı kullanılarak, 3 boyutlu 206 örnek, sonlu elemler kullanılarak modellenmiştir. Geliştirilen modeller literatürde mevcut deney sonuçlarına karşı onaylanmıştır. Hassasiyet çalışmasında 268 sonlu eleman modeli kullanılmıştır. Bu araştırma ters kanal bağlantısının sertlik, dayanma gücü, deformabilite kaynağı, rotasyon kapasitesi ve kırılma mekanizması üzerine ana vurgu yapmaktadır. Sayısal $M-\phi$ eğrileri sonuçları kullanılarak standardize edilmiş ters kanal uç plaka bağlantısının moment-rotasyon fonksiyonu sunulmuştur. Bağlantının davranışını tahmin edebilmek veya davranışı çerçeve analizi yazılımlarında kullanabilmek için moment-rotasyon fonksiyonu geometrik parametreler olarak ifade edilmiştir. Günümüzde mevcut olan 6 fonksiyon arasından Kishi-Chen ve Richard-Abbott modelleri deneysel ters kanal bağlantısı $M-\phi$ datalarına en iyi uydurulabilecek modeller olarak saptandı. İki fonksiyon, 140 örneğin ilişkisini ifade etmek için başarılı bir şekilde parametrik çalışmada kullanıldı. Analitik ve tahmin edilen data iyi bir uyum içerisindeydi. Ancak uygunlaştırılan fonksiyonların sonuçları boyutsuz şekliyle Richard-Abbott fonksiyonunun Kishi-Chen fonksiyonundan daha doğru olduğuna işaret etti. İlaveten, Eurocode 3 modelinin

sayısal $M-\phi$ eğrisi ile yapılan karşılaştırmalarında birçok durum için, özellikle de ilk sertliği düşük olan ters kanal bağlantısı için, diz bölgesinde ciddi abartılı davranış olduğu görüldü.

Anahtar Kelimeler: ters kanal, çift ters kanal, moment–rotasyon eğrisi, boru kolon, Yüksek mukavemetli çelik, sertlik, moment kapasitesi, rotasyon kapasitesi, standardize edilmiş fonksiyon, Kishi-Chen modeli, Richard-Abbott modeli

To my wife, my daughter and my parents

ACKNOWLEDGMENT

I would like to thank first of all almighty Allah who granted me the strength, patience, and power and knowledge after all to fulfill this study. I would like to express my great appreciation and gratitude to my supervisor, Asst. Prof. Dr. Mürüde Çelikağ, for her endless assistance and support in carrying out this study, taking to heart the responsibility of keeping the flow of research, presentation, avoiding obscurity, and strengthening consistency in the best way possible, I would also like to thank the Civil Engineering Department and members of the monitoring and examining committee for their suggestions.

I extend my gratitude to my lovely wife for her endless patience, support and understanding all through the period of my study.

My sincere reverence and thankfulness also go to my brothers Dr. Darwish Al Hendi and Eng. Dorgham Faidi, for their constant advice, guidance and positive attitude throughout my PhD research.

Finally, I would like to give thanks to all who supported me, particularly; my brothers Dr. Mahmoud Nazzal, Eng. Abd Mahmoud and Eng. Onur Ejder.

TABLE OF CONTENTS

ABSTRACT.....	iii
ÖZ	v
DEDICATION	vii
ACKNOWLEDGMENT	viii
LIST OF TABLES	xiii
LIST OF FIGURES	xv
NOMENCLATURE	xx
1 INTRODUCTION	1
1.1 Introduction.....	1
1.2 Research Significance.....	4
1.3 Objective of Study	5
1.4 Outline of Thesis.....	6
2 LITERATURE REVIEW	9
2.1 Connection Classification	9
2.2 Types of Beam to Tubular Column Connections	11
2.2.1 Double-Angle Shear Connections.....	12
2.2.2 Shear Tab Connections	14
2.2.3 Through-Plate Connections.....	16
2.2.4 End-Plate Connections	18
2.2.5 Top- and Seat-Angle Connections	22
2.2.6 Reverse Channel Connections (RCC).....	24
2.3 Moment-Rotation Models of Semi-rigid Connections	26
2.3.1 Empirical Models	28

2.3.2 Analytical Models	29
2.3.3 Mechanical Models	30
2.3.4 Numerical Models	31
2.3.5 Experimental Models	31
3 NUMERICAL MODELLING OF REVERSE CHANNEL CONNECTIONS (RCC) TO TUBULAR COLUMNS	33
3.1 Introduction.....	33
3.2 A Brief Summary of Previous Experimental Work.....	33
3.3 Finite Element Modeling	35
3.3.1 Boundary Conditions and Contact	37
3.3.2 Material Properties	38
3.3.3 Moment-Rotation Curves.....	40
3.3.4 Sensitivity Study Results	41
3.3.4.1 Mesh Sensitivity.....	41
3.3.4.2 Effect of Friction.....	42
3.3.4.3 Load Speed Sensitivity	43
3.4 Verification of Finite Element Simulations	44
4 EFFECT OF GEOMETRICAL PARAMETERS ON $M-\phi$ CHARACTERISTICS OF RCC	47
4.1 Introduction.....	47
4.2 Parametric Study.....	47
4.3 Finite Element Results and Observations	52
4.3.1 Effect of Flush End-Plate Thickness (G1)	56
4.3.2 Effect of the Wall Thickness of Reverse Channel (G2).....	57
4.3.3 Effect of the Width of Reverse Channel (G3).....	58

4.3.4 Effect of the Ratio of Reverse Channel Depth to SHS Width (G4).....	58
4.3.5 Effect of the Nominal Bolt Diameter and the Gage Distance (G5)	59
4.3.6 Sensitivity Chart.....	59
5 EFFECT OF MATERIALS STRENGTH ON $M-\phi$ CHARACTERISTICS OF RCC	
.....	61
5.1 Introduction.....	61
5.2 Parametric Study.....	63
5.3 FE results and Discussions.....	64
5.3.1 Effect of Reverse-Channel Material Property on the Response of RCC and	
DRCC.....	68
5.3.2 Comparison between the Behaviour of RCC and DRCC	71
5.3.3 Effect of the Variation of Clear Distance between the Split Reverse	
Channels on the Behaviour of DRCC	72
6 MATHEMATICAL MODELING OF $M-\phi$ RELATIONSHIP OF RCC.....	76
6.1 General.....	76
6.2 Mathematical Modeling of Moment-Rotation Curve	77
6.2.1 The Non-linear Moment-Rotation Models	77
6.2.2 Modelling Functions	78
6.2.3 The Kishi and Chen Model (Three-Parameter Power Model).....	82
6.2.4 The Richard-Abbott Model.....	83
6.2.5 Model Suggested by Eurocode-3	84
6.3 Mathematical Function of RCC	87
6.3.1 Selection of Parametric Study Cases	87
6.3.2 Normalized Moment-Rotation Function.....	90
6.3.3 Standardized Function of RCC	90

6.3.4 Comparison between Numerical $M-\phi$ Curves and the Model Suggested by Eurocode-3	99
7 CONCLUSION AND RECOMMENDATIONS FOR FUTURE WORK.....	101
7.1 Conclusions.....	101
7.2 Recommendations for Future Work.....	105
REFERENCES	107
APPENDICES	123
Appendix A: Schedule of RCC Dimensions, main parameters of the $M-\phi$ curves and the observed failure modes.....	124
Appendix B: Von Mises Stress Distributions of Selected RCC and DRCC Prior to Failure	135
Appendix C: Dimensionless Forms of Experimental Moment-Rotation Curves with Fitted Models	144

LIST OF TABLES

Table 1: Schedule of test specimens (Wang & Xue, 2013)	36
Table 2: Materials properties of reverse channel connection specimens (Wang & Xue, 2013).....	36
Table 3: Comparison between test and finite element results.....	45
Table 4: Schedule of test specimens in the parametric study	49
Table 5: Main parameters of the moment-rotation curves and the observed failure modes	53
Table 6: Schedule of test specimens in the parametric study	65
Table 7: Main parameters of the moment-rotation curves and the observed failure modes	66
Table 8: Comparison of RCC and DRCC with varied clear distance (h) between the split reverse channels in terms of $M_{j,ult,FE}$, $S_{j,in,FE}$, $\phi_{j,ult,FE}$ and the observed failure modes	75
Table 9: Comparison of different mathematical representations for the ($M-\phi$) curve (Chan & Chui, 2000, Faella, Piluso, & Rizzano, 2000).....	79
Table 10: Different non-linear $M-\phi$ models (Chan & Chui, 2000, Faella, Piluso, & Rizzano, 2000, Mohamadi-Shoore & Mofid, 2011)	80
Table 11: Coefficient of determination and standard error of estimate: comparison between fitted models of RCC	81
Table A.1: Schedule of RCC dimensions of Set1 in the parametric study.	125
Table A.2: Schedule of RCC dimensions of Set2 in the parametric study.	126
Table A.3: Schedule of RCC dimensions of Set3 in the parametric study.	127
Table A.4: Schedule of RCC dimensions of Set4 in the parametric study.	128

Table A.5: Schedule of RCC dimensions of Set5 in the parametric study.	129
Table A.6: Main parameters of the moment-rotation curves and the observed failure modes of Set1.....	130
Table A.7: Main parameters of the moment-rotation curves and the observed failure modes of Set2.....	131
Table A.8: Main parameters of the moment-rotation curves and the observed failure modes of Set3.....	132
Table A.9: Main parameters of the moment-rotation curves and the observed failure modes of Set4.....	133
Table A.10: Main parameters of the moment-rotation curves and the observed failure modes of Set5.....	134

LIST OF FIGURES

Figure 1: Typical components of reverse channel connection (RCC).....	3
Figure 2: Classification boundaries according to Eurocode 3 for: (a) stiffness and (b) strength (CEN, 2005).....	10
Figure 3: Double-angle shear connection (Kurobane, Packer, Wardenier, & Yeomans, 2004).....	12
Figure 4: Double-angle shear connection with small hollow structural section column (Gong, 2008).....	14
Figure 5: Shear tab connection (Kurobane, Packer, Wardenier, & Yeomans, 2004)	15
Figure 6: Through-plate connection (Kurobane, Packer, Wardenier, & Yeomans, 2004).....	17
Figure 7: The through plate moment connection: (a) Planar-form configuration, (b) Planar-form assembly (Mirghaderi, Torabian, & Keshavarzi, 2010).....	18
Figure 8: Typical extended endplate connections: (a) 4-bolt unstiffened, (b) 4-bolt stiffened, (c) 8-bolt unstiffened, and (d) 8-bolt stiffened.....	20
Figure 9: (a) Detail of five-part Holo-Bolt, (b) Stages of the Flowdrill process (British Steel, 1997).....	21
Figure 10: Top- and seat-angle connection (Kurobane, Packer, Wardenier, & Yeomans, 2004).....	23
Figure 11: Typical moment-rotation curves of common connections (Chen, Kishi, & Komuro, 2011).....	27
Figure 12: Reverse channel connection geometries.....	34
Figure 13: Typical finite element mesh of RCC assembly.....	37

Figure 14: Boundary conditions, reference points used to measure the vertical displacements, and loading direction of RCC assembly.....	38
Figure 15: Idealized material behavior used in the FEM analysis for: (a) Beam, column, channel, and end plate (b) High-strength bolts (Mohamadi-shooreh & Mofid, 2008)	39
Figure 16: Main characteristics of the moment-rotation curves	41
Figure 17: Effect of number of elements in the mesh on the calculation time and the RCC response of Test 1	42
Figure 18: Effect of friction on the RCC response of Test 1	43
Figure 19: Effect of loading speed on the RCC response of Test 1.....	44
Figure 20: Moment-rotation curves from experimental and FE models for RCC connections of: (a) Test 1, (b) Test 3 and (c) Test 5	46
Figure 21: The cantilever arrangement and locations of the reference points that are used to measure the displacement.....	48
Figure 22: The typical FE mesh for the cantilever arrangement.....	50
Figure 23: Moment-rotation curves for: (a) G1, (b) G2, (c) G3, (d) G5, (e) First series of G4 and (f) Second series of G4	54
Figure 24: Joint general response before and after failure: (a) Bolt's head pull-out from reverse channel (BPO) of S7 and (b) End-plate pulled outwards (EPO) of S11	55
Figure 25: Strain measurements, between tension bolts, in x and y-directions; extreme specimens in each group	56
Figure 26: The sensitivity chart on the characteristics of moment-rotation of RCC .	60
Figure 27: Double reverse channel connection (DRCC).....	62

Figure 28: Comparison of moment-rotation curves from FE models between RCC and DRCC with and without HSS.	67
Figure 29: Strain measurements between tension bolts in x and y directions; (a) S12 and HSS-S12 and (b) DRS12 and DRHSS-S12	68
Figure 30: Joint general response prior to failure: Bolt's head pull-out from reverse channel (BPO) of (a) S1, (b) HSS-S1, (c) DR-S1 and (d) DRHSS-S1	69
Figure 31: Joint general response prior to failure: End-plate pulled outwards (EPO) of (a) S11, (b) HSS-S11, (c) DR-S11 and (d) DRHSS-S11.....	71
Figure 32: Effects of the variation of clear distance (h) between the split reverse channels for (a) S15, (b) S31 and (c) S32	74
Figure 33: The effect of change in beam depth on the DRCC $M-\phi$ response for two constant percentage values of h for (a) 20% and (b) 50%	74
Figure 34: The Eurocode 3 representation of the moment-rotation curve (Faella, Piluso, & Rizzano, 2000)	85
Figure 35: Comparison between EC3 Annex J model and Moment-rotation curves from experimental: (a) Test 1, (b) Test 2, (c) Test 3, (d) Test 4 and (e) Test 5	86
Figure 36: General description of the geometrical parameters used in parametric study.....	88
Figure 37: Moment-rotation curves from FE models for RCC: (a) Set1, (b) Set2, (c) Set3, (d) Set4 and (e) Set5	91
Figure 38: Normalized form of moment-rotation curves: (a) Set1, (b) Set2, (c) Set3, (d) Set4 and (e) Set5	92
Figure 39: Comparison of analytical $M-\phi$, Kishi-Chen and Richard-Abbott curve fit and Eurocode 3-(revised) Annex J for RCC with low, medium and high initial stiffness	95

Figure 40: Comparison of analytical and predictive functions: (a) $M_{j,R}$, (b) $\phi_{j,R}$, (c) $M_{j,ult,n}$, (d) n for Kishi-Chen model, (e) $S_{j,P,n}$ and (f) n for Richard-Abbott model	98
Figure B.1: Von Mises stress distributions of RCC joints prior to failure: (a) S37, (b) S38, (c) S39, (d) S40, (e) S41 and (f) S42.	136
Figure B.2: Von Mises stress distributions of RCC joints prior to failure: (a) S73, (b) S74, (c) S75, (d) S76, (e) S77 and (f) S78.	137
Figure B.3: Von Mises stress distributions of RCC joints prior to failure: (a) S91, (b) S92, (c) S93, (d) S94, (e) S95 and (f) S96.	138
Figure B.4: Von Mises stress distributions of RCC joints prior to failure: (a) S133, (b) S134, (c) S135, (d) S136, (e) S137 and (f) S138.	139
Figure B.5: Von Mises stress distributions of RCC joints prior to failure: (a) S157, (b) S158, (c) S159, (d) S160, (e) S161 and (f) S162.	140
Figure B.6: Von Mises stress distributions of HSS-RC joints prior to failure: (a) HSS-S7, (b) HSS-S8, (c) HSS-S9, (d) HSS-S10, (e) HSS-S11 and (f) HSS-S12. ..	141
Figure B.7: Von Mises stress distributions of BR-RC joints prior to failure: (a) BR-S1, (b) BR-S2, (c) BR-S6, (d) BR-S7, (e) BR-S11 and (f) BR-S12.	142
Figure B.8: Von Mises stress distributions of HSS-BR-RC joints prior to failure: (a) BRHSS-S1, (b) BRHSS-S2, (c) BRHSS-S6, (d) BRHSS-S7, (e) BRHSS-S11 and (f) BRHSS-S12.	143
Figure C.1: Normalized moment-rotation curve of Test 1 with fitted models; (a) Ang-Morris Model, (b) Kishi-Chen Model, (c) Yee-Melcher Model, (d) Chisala Model, (e) Richard-Abbut Model and (f) Wu-Chen Model	145
Figure C.2: Normalized moment-rotation curve of Test 2 with fitted models; (a) Ang-Morris Model, (b) Kishi-Chen Model, (c) Yee-Melcher Model, (d) Chisala Model, (e) Richard-Abbut Model and (f) Wu-Chen Model.	146

Figure C.3: Normalized moment-rotation curve of Test 3 with fitted models; (a) Ang-Morris Model, (b) Kishi-Chen Model, (c) Yee-Melcher Model, (d) Chisala Model, (e) Richard-Abbut Model and (f) Wu-Chen Model. 147

Figure C.4: Normalized moment-rotation curve of Test 4 with fitted models; (a) Ang-Morris Model, (b) Kishi-Chen Model, (c) Yee-Melcher Model, (d) Chisala Model, (e) Richard-Abbut Model and (f) Wu-Chen Model. 148

Figure C.5: Normalized moment-rotation curve of Test 5 with fitted models; (a) Ang-Morris Model, (b) Kishi-Chen Model, (c) Yee-Melcher Model, (d) Chisala Model, (e) Richard-Abbut Model and (f) Wu-Chen Model. 149

NOMENCLATURE

Acronyms

AISC	American Institute of Steel Construction
BF	Bolt Failure
BPO	Bolt's head Pull-Out from reverse channel
COV	Coefficient of Variation
DC	Deformation in Channel
DE	Deformation in End plate
DRCC	Double Reverse Channel Connections
EC3	Eurocode 3
EPO	End-plate Pulled Outwards
FEMA	Federal Emergency Management Agency
FEM	Finite Element Modelling
GRG	Generalized Reduced Gradient
HSS	High Strength Steels
RCC	Reverse Channel Connections
SHS	Square Hollow Sections
SCDB	Steel Connection Data Bank

Notations

D	Depth of beam
d_{bolt}	Bolt diameter
D_{col}	Depth of column
h	Clear distance between double reverse channels

h_b	Overall depth of beam
h_{EP}, h_p	Height of end plate
H_{col}	Height of the column
I_c	Second moment of area of the column
g	Gage distances
l_{en}	Length of elements close to the connection
l_{ef}	Length of the elements far from the connection
L_{load}	Distance between the load application point and the face of the reverse channel
m	Channel width
M	Applied bending moment
$M_{j,R}$	Plastic flexural resistance of the joint
$M_{j,Rd}$	Joint design moment resistance
$M_{j,ult}$	Ultimate flexural resistance of the joint
n	Shape parameter
n_{et}	Number of elements through the thickness
P	Applied load
p_f	Bolt pitch
R^2	Coefficient of determination
S_j	Secant stiffness
$S_{j,in}$	Initial stiffness of the joint
$S_{j,P}$	Post-yield stiffness
$S_{\phi,M}$	Standard error of estimate of ϕ on M
$S_{M,\phi}$	Standard error of estimate of M on ϕ
$S_{P,A}$	Standard error of estimate of P on A

t_{fb}	Flange thickness of beam
t_f, t_{fc}	Channel flange thickness
t_p	Flush end-plate thickness
t_{wb}	Web thickness of beam
t_w, t_{wc}	Channel web thickness
w_b	Width of beam
w_p	Width of end plate
Z_b	Beam plastic modulus

Greek Letters

$\delta_{b,el(x_{B_i})}$	Elastic deflection of beam
γ	Shear deformation of the column web panel zone
θ_c	Connection rotational deformation
ϕ	Rotational deformation of this joint
$\phi_{j,R}$	Rotation corresponding to the plastic flexural resistance
$\phi_{j,x}$	Rotation at which the moment resistance first reaches the design moment resistance of the joint
$\phi_{j,ult}$	Rotation corresponding to the ultimate flexural resistance
Ψ	Shape factor
ε_y	Yield strain
ε_u	Ultimate strain
σ	True stress
ε_{pl}	True plastic strain

Chapter 1

INTRODUCTION

1.1 Introduction

In recent years, changes in moment-resisting frame design practice have seen increased use of steel hollow sections as structural members instead of conventional open sections. This was partly due to their superior torsional rigidity and hence resistance to flexural-torsional and torsional buckling modes. In addition, when they are employed as columns in long-span steel structures, they can be designed to have similar strength and stiffness about each horizontal axis (Anderson & Linderman, 1991). This popularity of steel hollow sections is also due to the numerous advantages they provide when compared to conventional open sections. For example; they typically have lower-surface area and lighter weight, which results in cost savings in painting, transportation to site and erection (Kosteski & Packer, 2003). Being a closed section it is also more resistant to corrosion, particularly when exposed to severe weather conditions.

However, there are difficulties with the detailing of the connections, particularly when I-beams are connected to tubular columns in traditional structures. Accessibility problems seriously affect the use of widely known semi-rigid/partial-strength bolted beam to tubular column connections. Therefore, various types of connections are proposed either by fitting a structural section, such as, longitudinal plate, double angle, tee, reverse channel, top and bottom angle, to the tubular column

face by fully welding or by employing blind-bolts with sleeves that expand inside the tube.

For the past few decades, extensive research had been carried out to understand the actual behavior of beam-to-tubular column connections and to establish the moment-rotation relationship for the completeness of the new simplified analysis and practical connection design. The connection classification is mainly dependent on the moment-rotation characteristics. Since experimental research is lengthy and expensive process for understanding such behaviour then the availability of powerful computer facilities can be a suitable alternative for modeling structural behaviour of complex and lengthy parametric studies. Therefore, the finite element modeling was used to carry out the parametric studies based on computer simulation in many research.

In 2007, Ding and Wang (2007) suggested the use of reverse channel connection (RCC) to connect I-beam to tubular column (Figure 1), where the reverse channel is welded in shop to the tubular column, the flush/extended endplate is welded to the beam and the beam is connected to the reverse channel on site by using bolts. This assembly overcomes the difficulty of access to the internal face of tubular columns by giving access from inside of the channel.

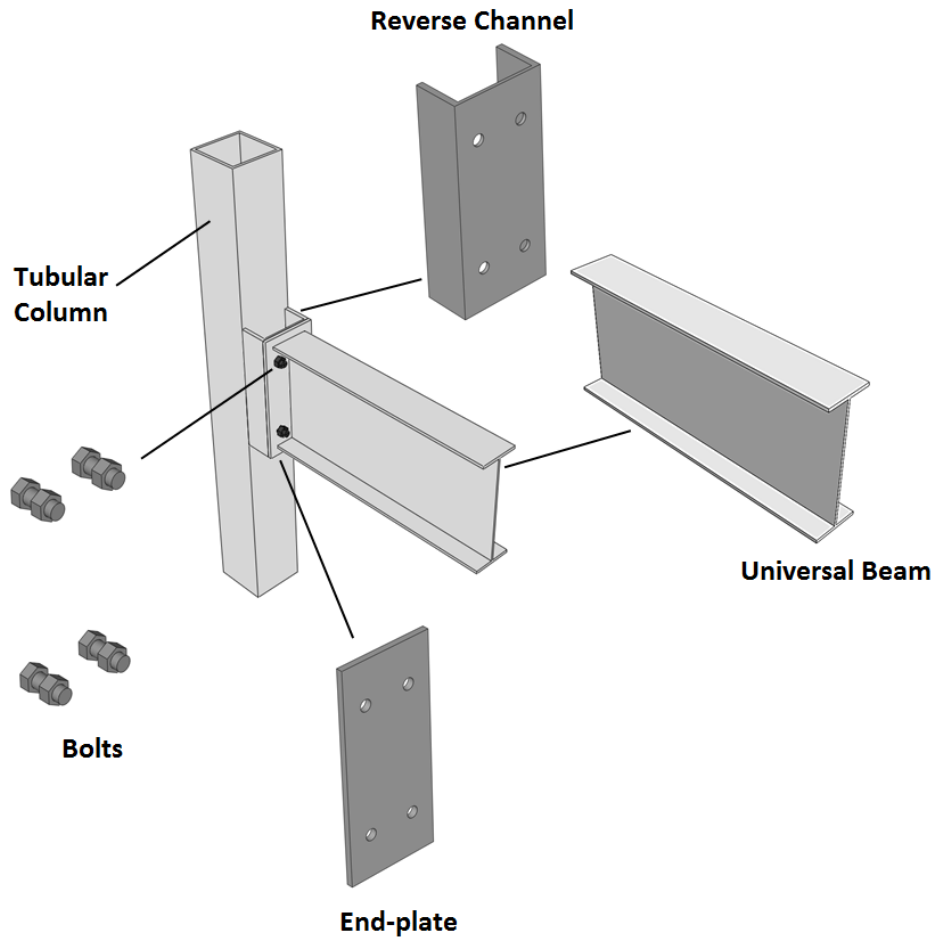


Figure 1: Typical components of reverse channel connection (RCC)

Since then numerous researches (Ding & Wang, 2007), (Elghazouli , Málaga-Chuquitaype, Castro, & Orton, 2009), (Málaga-Chuquitaype & Elghazouli, 2010a), (Elsawaf, Wang, & Mandal, 2011), (Liu, Málaga-Chuquitaype, & Elghazouli, 2012a), (Elsawaf & Wang, 2012), (Liu, Málaga-Chuquitaype, & Elghazouli, 2012), (Xue, 2012), (Huang, Davison, & Burgess, 2013a), (Elsawaf & Wang, 2013), (Huang , Davison, & Burgess, 2013) and (Wang & Xue, 2013) have been carried out, which were mainly concentrated on the fire and earthquake resistance of RCC and very limited research on its basic structural behaviour.

1.2 Research Significance

The failure of welded connections (Northridge connections) in numerous steel moment resisting frames during the 1994 Northridge Earthquake raised many questions regarding the validity of the design and construction procedures used at that time. After the earthquake, a comprehensive research effort funded by the Federal Emergency Management Agency (FEMA) through the SAC Joint Venture contributed greatly to the understanding of the seismic behavior of steel moment resisting frames. As a result, practical design guidelines were published in a series of FEMA documents, which cover details of a number of pre-qualified connections. The pre-qualified connections are only for I-section (W) column since tubular (Box) columns were not considered because they were not very common in US design practice at that time (ASCE, 2000). The tubular column is the column-of-choice in Japanese steel building design practice (AIJ, 1997), (Nakashima, Roeder, & Maruoka, 2000). The detailing of the connections and design of Japanese tubular columns are sufficiently different from European practice.

The current European steel design standards also lack guidance on semi-rigid/partial-strength bolted beam to tubular column connections (Liu, Málaga-Chuquitaype, & Elghazouli, 2012a). On the other hand, CIDECT provides design guidelines (Kurobane, Packer, Wardenier, & Yeomans, 2004) and Eurocode 3 Part 1-8 (CEN, 2005) proposes rules for determining the resistance of beam-to-tubular column fully-rigid/fully welded connections (Málaga-Chuquitaype & Elghazouli, 2010a).

Hence, the necessity for more investigation on beam to tubular column connection behavior has encouraged researchers to find out suitable connection configurations and to ensure that they are feasible for practical application.

With reference to reverse channel connections (RCC), there is still need for further investigation of the effect of the geometrical configurations and materials properties which may affect the moment-rotation characteristics. Moreover, for the purposes of either predicting the RCC behavior or incorporating the behavior into a frame analysis computer program, the moment-rotation ($M-\phi$) curves have to be modeled by using mathematical representation.

1.3 Objective of Study

The main objective of this research is to investigate the monotonic behaviour of reverse channel flush end-plate connections by evaluating the characteristics of the moment-rotation ($M-\phi$) relationship. In order to facilitate this object, the effect of the geometrical configurations and materials properties of RCC on the moment-rotation ($M-\phi$) relationship were minutely monitored. On the other hand, for the purpose of predicting the response of RCC directly from its geometrical and mechanical properties, mathematical representation of the moment-rotation ($M-\phi$) curve of RCC was developed.

In this study, the geometric parameters include; the thickness of flush end-plate, the wall thickness of reverse channel cut from hot-rolled square hollow sections (SHS), the ratio of flush end-plate thickness to the wall thickness of reverse channel, the width of hot-rolled reverse channels, the ratio of reverse channel depth to SHS width for different types of channel, the nominal bolt diameter and the gage distance.

Concerning the effect of materials properties, HSS and mild steel reverse channel to tubular column connections are investigated in terms of strength, stiffness and ductility.

The general-purpose finite element program, ABAQUS/ Standard (v.6.12), was employed to conduct 3-D nonlinear FE simulations for the parametric studies. 206 models with different connection configurations; varying dimensions of column sizes, beam sections and channel types were modeled in this study.

This study is a basic step towards establishing the requirements for the design of semi-rigid/partial-strength I-beam to tubular column connections and it is also trying to contribute to the development of a simple and accurate moment-rotation ($M-\phi$) relationship for the purpose of structural design and elastic-plastic analysis.

1.4 Outline of Thesis

This thesis contains seven chapters' the details of which are given below:

- Chapter 2: Literature Review. In this chapter, literature survey gives a general introduction to the connection classification according to Eurocode 3 (1993) Annex J, followed by an overview about beam to tubular column connections and highlight on the research done on the behaviour of such joints. Finally, moment-rotation models of semi-rigid connections are highlighted.
- Chapter 3: Numerical Modelling of Reverse Channel Connections (RCC) to Tubular Columns. This chapter presents a brief description of five RCC tests recently conducted by Wang and Xue (2013) and presents the methodology employing the general finite element software ABAQUS for numerical modeling of the monotonic behaviour of reverse channel flush end-plate

connections. Since this model is subsequently used as the tool for further analyses in this research, this chapter includes the results of sensitivity studies on the mesh size, the effect of friction and the effect of loading speed on moment-rotation response.

- Chapter 4: Effect of Geometrical parameters on $M-\phi$ Characteristics of RCC. This chapter attempts to give a qualitative view of the influence of the geometrical configurations of reverse channel connections (RCC) on the moment-rotation ($M-\phi$) response. These geometric parameters include; the thickness of flush end-plate, the wall thickness of reverse channel cut from hot-rolled square hollow sections (SHS), the ratio of flush end-plate thickness to the wall thickness of reverse channel, the width of hot-rolled reverse channels, the ratio of reverse channel depth to SHS width for different types of channel, the nominal bolt diameter and the gage distance. For this purpose, ABAQUS (v.6.12) software is used to develop three-dimensional (3-D) FE models for thirty specimens.
- Chapter 5: Effect of Materials Strength on $M-\phi$ Characteristics of RCC. This chapter reports on the possible achievements on moment-rotation ($M-\phi$) characteristics of reverse channel flush end-plate connections (RCC) by using HSS reverse channel under monotonic loading. It also introduces a double reverse channel connection (DRCC), where the reverse channel is split into two pieces, by leaving a gap in between, for better access to bolts. Subsequent sections of this chapter describe the specimens considered in parametric study. The effect of material properties of DRCC and the variation of clear distance between the split reverse channels; and then the results are compared with those of RCC.

- Chapter 6: Mathematical Modeling of $M-\phi$ Relationship of RCC.

The sections of this chapter describe the methodology used for selecting the modeling function; which will be adopted in this study to represent the moment-rotation ($M-\phi$) relationship of RCC. The characteristics of the standardized function and the procedures for deriving its parameters, in terms of geometric RCC parameters, are also illustrated. Finally, the suitability of Eurocode 3-Annex J representation for moment-rotation curve for RCC is discussed.

- Chapter 7: Conclusions and Recommendations for Future Work

This chapter presents the conclusions drawn from this particular research and recommends further future works to investigate the behaviour of RCC and DRCC.

Chapter 2

LITERATURE REVIEW

2.1 Connection Classification

In construction of steel framed buildings, beam-to-column connections are widely used. Depending on the moment–rotation characteristic connections between I- and H-sections can be classified as rigid connections; which transmit full moment from beam to column, simple or shear connections; which transmit shear from beam to column, or semi-rigid connections; which are known to have finite stiffness and strength and therefore transmit some moments from the beams to the columns.

The Eurocode 3 (CEN, 2005) Annex *J* Clause 2.2.2 classifies connections in terms of strength and stiffness. The stiffness classification is performed by simply comparing the initial design joint stiffness, $S_{j,in}$, with the two stiffness boundaries (Figure 2.a). On the other hand, the strength classification consists of the comparison of the joint design moment resistance, $M_{j,Rd}$, with the "full-strength" and "pinned" boundaries (Figure 2.b). For the sake of simplicity, the Eurocode (2005) Annex *J* Clause 2.1.1 provides a direct mathematical comparison with both the initial design joint stiffness, $S_{j,in}$, and the joint design moment resistance, $M_{j,Rd}$ for the joint classification.

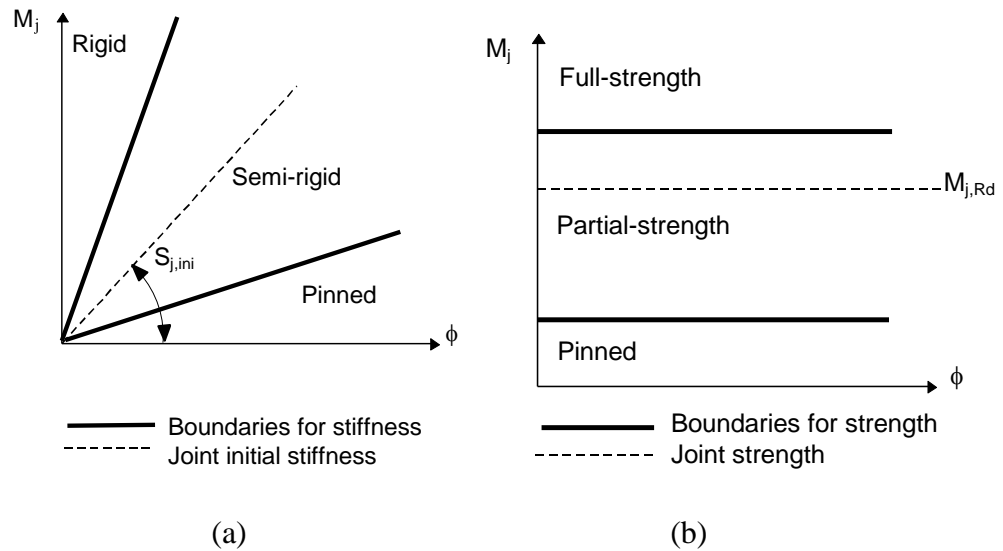


Figure 2: Classification boundaries according to Eurocode 3 for: (a) stiffness and (b) strength (CEN, 2005)

The stiffness and strength boundaries for the joint classification are given as follows:

Classification by stiffness

- rigid joint $S_{j,in} \geq 25 EI/L$ (unbraced frames)
 $S_{j,in} \geq 8 EI/L$ (braced frames)
- semi-rigid joint $0,5EI/L < S_{j,in} < 25EI/L$ (unbraced frames)
 $0,5EI/L < S_{j,in} < 8EI/L$ (braced frames)
- pinned joint $S_{j,in} \leq 0,5EI/L$

Classification by strength

- full-strength joint $M_{j,Rd} \geq M_{full-strength}$
- partial strength joint $0,25M_{full-strength} < M_{j,Rd} < M_{full-strength}$
- pinned joint $M_{j,Rd} \leq 0,25M_{full-strength}$

However, all this information is not yet widely available for tubular beam-to-column connections (Kurobane, Packer, Wardenier, & Yeomans, 2004). On the other hand, depending on the stiffness, the connections can be classified as (nearly) rigid or (nearly) pinned.

2.2 Types of Beam to Tubular Column Connections

As already stated in Section 1.1, tubular columns are increasingly used as structural members since they offer high capacities coupled with relatively high bending stiffness. Additionally, they have superior resistance to axial compression loads, which is important for axially loaded members subject to reversal of loads (Gorenc, Tinyou , & Syam, 2005). However, the connections between such columns and beams need careful attention with their detailing and assembly, particularly when traditional bolts and nuts are fastened to the face of column. The restricted access to the internal face of the column is considered as a potential problem. In consequence, various kinds of connections were proposed in literature to connect beams to tubular columns to overcome this problem. Possible solutions can be obtained either by fully welding a structural section, such as, longitudinal plate, double angle, tee, reverse channel and top and bottom angle to the tubular column face or by employing blind-bolts with sleeves that expand inside the tube.

The design guidelines provided by CIDECT (Kurobane, Packer, Wardenier, & Yeomans, 2004) classifies the types of beam to tubular column connections under two title; simple shear connections and rigid or moment connections. In this section, the most common types of simple or shear connections are briefly presented.

2.2.1 Double-Angle Shear Connections

Double-angle shear connections are among the most commonly used simple connections in steel construction. It provides the strength of bolts in double shear combined with excellent connection flexibility. A double-angle connection is made with two angles (Figure 3), one on each side of the web of the supported beam. The leg of the angles connected to the web of the supported beam is called the web-framing leg, while the other leg connected to the support is called the outstanding leg (Gong, 2008).

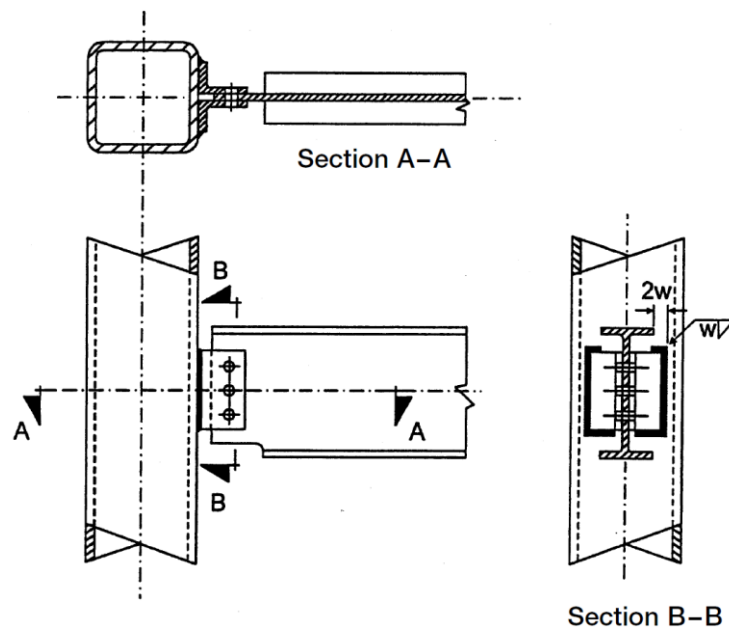


Figure 3: Double-angle shear connection (Kurobane, Packer, Wardenier, & Yeomans, 2004)

Many previous studies were carried out on the behavior of double angle connections, particularly, when the angles are welded to the H-section column, (McMullin & Astaneh , 1988), (De Stefano & Astaneh, 1991), (Sherman, 1995), (Guravich & Dawe, 1998), (Yang, Murray, & Plaut, 2000), (Hong, Yang, & Lee, 2001), (Hong, Yang, & Lee, 2002), (Gong & Gillies, 2008), etc.. Most of them were focused on the moment–rotation relationship under shear loads. Various analytical models and design formulas were also proposed to describe this relationship.

A lot of experiments have been carried out to investigate the parameters that affect the behavior of double angle connections. It was found that there are various parameters, including the thickness, length and material properties of the angles, the gage distances, the type and size of the fasteners, the depth and length of the beam and the properties of the column (Yang, Murray, & Plaut, 2000).

Yang et al. (2000) studied the responses of double angle connections welded to the beam web and bolted to the column flange for monotonically-applied shear loads, axial loads and combined loads with three different thicknesses of steel angles. A three-dimensional finite element analysis using ABAQUS has been developed and an experimental test program was carried out to study this response. Load–displacement curves, moment–rotation curves and stress distributions were obtained. The results showed that the angle thickness has significant effect on the behavior of the connection; the initial stiffness (i.e. the initial slope of the curves) increases and the level of the load or moment required to produce a given displacement or rotation increases greatly as the thickness of the angle increased. A conclusion was drawn that the behavior of double angle connections under axial and/or shear loading is complex, due to inelastic behavior, prying forces, loss of contact between components and the actions of bolts (e.g. prestressing, slip, and contact forces).

On the other hand, Hong et al. (2001, 2002) considered the effect of bolt gage distance and angle thickness on the moment–rotation relationship of double angle connections welded to the beam web and bolted to the column flange. To establish this effect, the 3D nonlinear finite element analysis and the actual tests were carried out, where the connections were loaded monotonically-applied shear loads. The results demonstrated that the initial stiffness of the moment–rotation curves increases

as the gage distance gets shorter or the angle grows thicker. However, tests proved that an excessive reduction of gage distance and increase of angle thickness caused an earlier failure because of stress concentration.

Considering the researchers that investigated the rotation capacity of double-angle shear connections, Gong (2008) studied the behavior of double-angle shear connections with small-size structural hollow section columns (Figure 4). He conducted an experimental study, which consisted of 12 full-scale connection tests. In his study, the connections were loaded simultaneously under a shear load and a target rotational demand of 0.04 rad. The connection specimens were brought to their theoretical shear failure strengths without any premature failure. The tested connections had a rotational capacity of at least 0.037 rad.

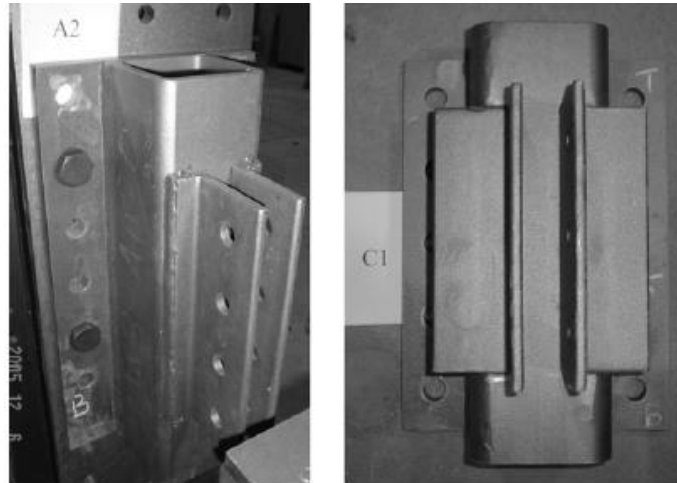


Figure 4: Double-angle shear connection with small hollow structural section column (Gong, 2008)

2.2.2 Shear Tab Connections

The shear tab connection consists of a plate welded to the supporting column and typically bolted to the supported beam (Figure 5). It is highly popular due to its ease of fabrication and cost-efficiency in terms of construction and material. Through

experimental investigations of nine types of simple framing connections between I-section beams and RHS columns subjected shear force, Sherman (1995) proved that the shear tab connection was the cheapest among the others connections in terms of the cost of the connecting materials and the fabrication. With such connections, the plate is typically shop welded to the column and then, for erection convenience, field bolted to the end of the beam.

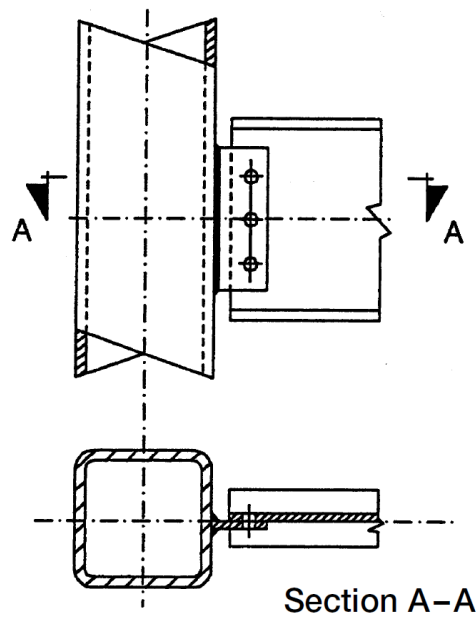


Figure 5: Shear tab connection (Kurobane, Packer, Wardenier, & Yeomans, 2004)

The work done by White and Fang (1966) can be considered as one of the earliest experimental studies on simple connections. Five different types of connections between I-section beams and square and rectangular structural steel tubular columns were tested. Shear tab was one of the connection types tested. The results indicated that, when longitudinal plate was welded to the tubular column section and subject to a shear load, the tube wall had tendency to induce excessive local deformation and weakening of the tubular column section. Thereafter, the research on this topic indicated one more possible failure mode for the connection which was warping of

the tab (longitudinal plate) due to twisting of the beam end. In the latter case, it was recommended to provide lateral support in the vicinity of the connection.

For the hollow section column in a shear tab connection, tests have shown that flexural failure associated with connection rotation was never a critical limit state for the connection. This is due to the restraint on the distortion of the column face and the limit on the end slope of the simply-supported beam. It has also shown that if a thick shear tab is joined to a relatively thin column then this may lead to a punching shear failure of the column connection face (Jarmai & Farkas, 1998).

2.2.3 Through-Plate Connections

This connection consists of a vertical plate passing through the column, welded in shop to the column flanges and the beam is connected to the plate called Through Plate (Figure 6). The through-plate connection is more than twice as expensive as the shear tab connection in terms of the cost of the connecting materials and the fabrication. Furthermore, it may be considered as the most expensive simple connection (Sherman, 1995). Consequently, the usage of this connection may be limited when single plate is preferred and the column is a “slender” section (Kurobane, Packer, Wardenier, & Yeomans, 2004).

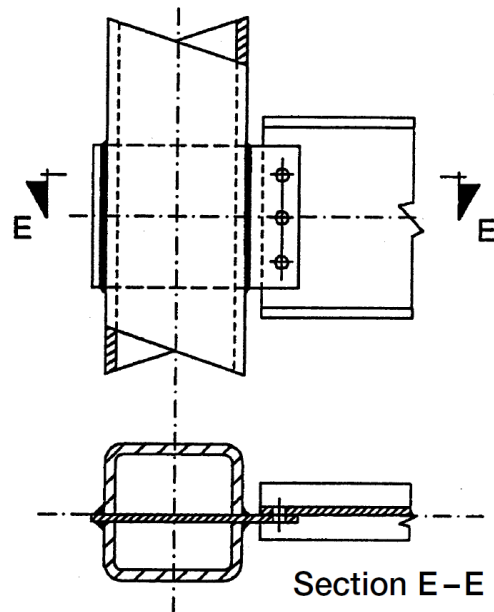


Figure 6: Through-plate connection (Kurobane, Packer, Wardenier, & Yeomans, 2004)

Limited numbers of studies were done on this type of connection due to its high cost of material and fabrication. However, a remarkable number of these tests tried to capture and monitor the connection seismic behavior in terms of ductility. For instance, Keshavarzi et al. (2008) investigated the seismic behavior of through-plate moment connections to box columns and the results established the effectiveness of the through plate in mitigating local stress concentrations and forming the plastic hinge zone in the beam away from the beam to column interface. On the other hand, Mirghaderi et al. (2010) proposed a new through plate moment connection to eliminate the continuity plates and facilitate the connection construction (Figure 7). This connection consists of a vertical plate (through plate) that passes through two aligned slots on the column flanges and is connected to them. The beam connection to the through plate is provided by the longitudinal connection of the flanges to both sides of the through plate, after trimming the beam web in this region and also the two web connection plates on both sides of the through plate.

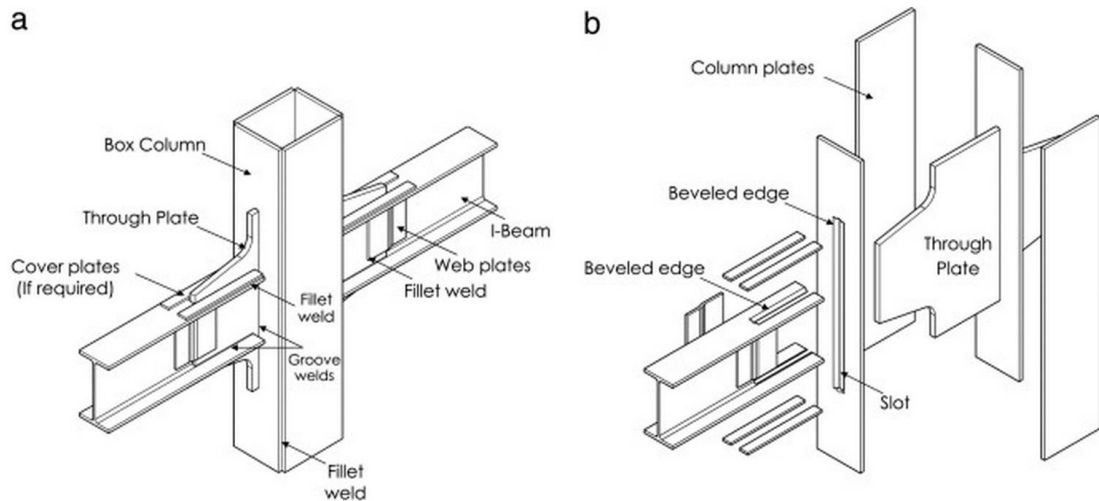


Figure 7: The through plate moment connection: (a) Planar-form configuration, (b) Planar-form assembly (Mirghaderi, Torabian, & Keshavarzi, 2010)

They conducted an experimental study, which consisted of the test of two relatively identical cyclically loaded connections. Consequently, the results showed that the specimens reached at least 0.06 rad total story drift before experiencing strength degradation which was more than 0.04 story drift criterion specified by AISC seismic provisions for qualifying connections for seismic use.

2.2.4 End-Plate Connections

In recent years, the end-plate connection has gained popularity in steel building construction due to its economy, simplicity of fabrication and good performance. A simple end-plate connection consists of a rectangular steel plate welded in shop to the beam end, then bolted to the column flange on site. Adjustments can be made to a simple end-plate connection to meet the requirements of different situations. For example, stiffeners can be added to maintain the stiffness of a connection while reducing the end-plate thickness. The family of end-plate connections can be classified into two basic categories: flush end-plate connections and extended end-plate connections. A flush end-plate connection comprises of an end-plate of nearly the same height as the beam depth, while the extended end-plate connection has an end-plate with its height beyond the beam depth and utilizes the space above and

below the beam for additional rows of bolts. Some popular types of extended endplate connections without the column-side are shown in Figure 8. These connections are commonly classified by the number of bolts in the tension flange region. Among them, the four-bolt connections (Figure 8 (a-b)) are generally limited by bolt strength and are designed to use less than one-half of the available beam strength. If a connection with higher capacity is desired, the eight-bolt connection should be used. The first alternative shown in Figure 8 (c) is suitable for beams and columns with relatively wide flanges to accommodate four bolts in a row with the benefit that all bolts contribute equally in defining the strength of the connection. On the other hand, the second alternative shown in Figure 8 (d) requires a lesser flange width of beams and columns, and is more practical (Gorenc, Tinyou , & Syam, 2005).

Due to lack of access inside the hollow section column to tighten the conventional bolts, blind bolts or purpose-designed bolts, which can be installed from one side, gives a choice to overcome this problem. Flowdrill and Hollo-Bolt (Lindapter) are well-established blind-bolting technologies suitable for structural jointing applications (British Steel, 1997).

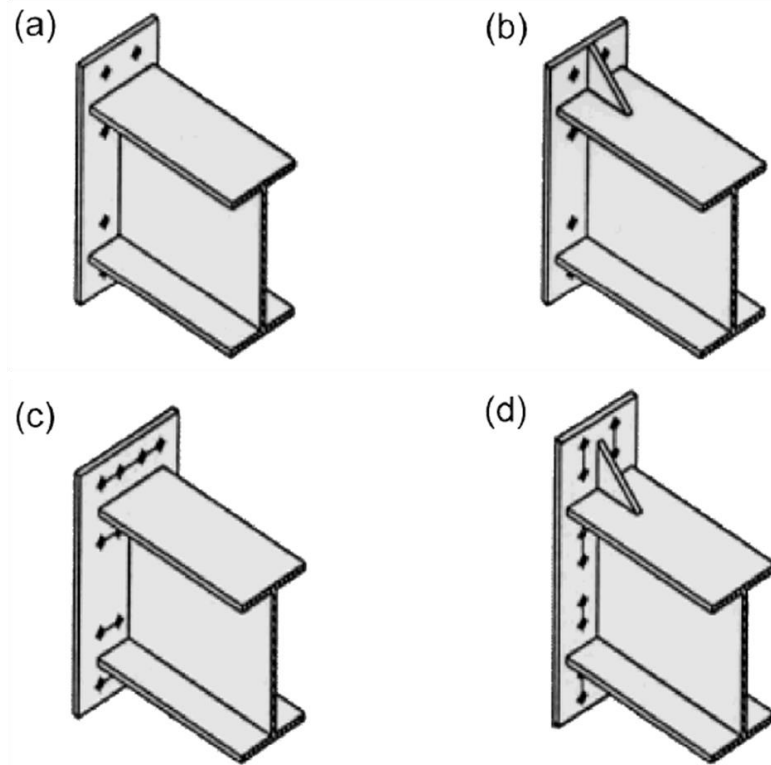


Figure 8: Typical extended endplate connections: (a) 4-bolt unstiffened, (b) 4-bolt stiffened, (c) 8-bolt unstiffened, and (d) 8-bolt stiffened

Figure 9(a) illustrates the main parts of Hollo-Bolt. The installation process of Hollo-Bolt required two spanners; one is used to hold the collar and another to tighten the central bolt. On the other hand; the flowdrill process is demonstrated in Figure 9(b). This process allows a thread to be incorporated into relatively thin steel by locally displacing the metal and increasing the thickness of the thread in the first stage and then permit tapping of a thread into the steel in the second stage (France, Davison, & Kirby, 1999).

A considerable amount of literature has been published on the behavior of end-plate connections; (Korol, Ghobarah, & Mourad, 1993), (France, Davison, & Kirby, 1999), (France, Davison, & Kirby, 1999a).

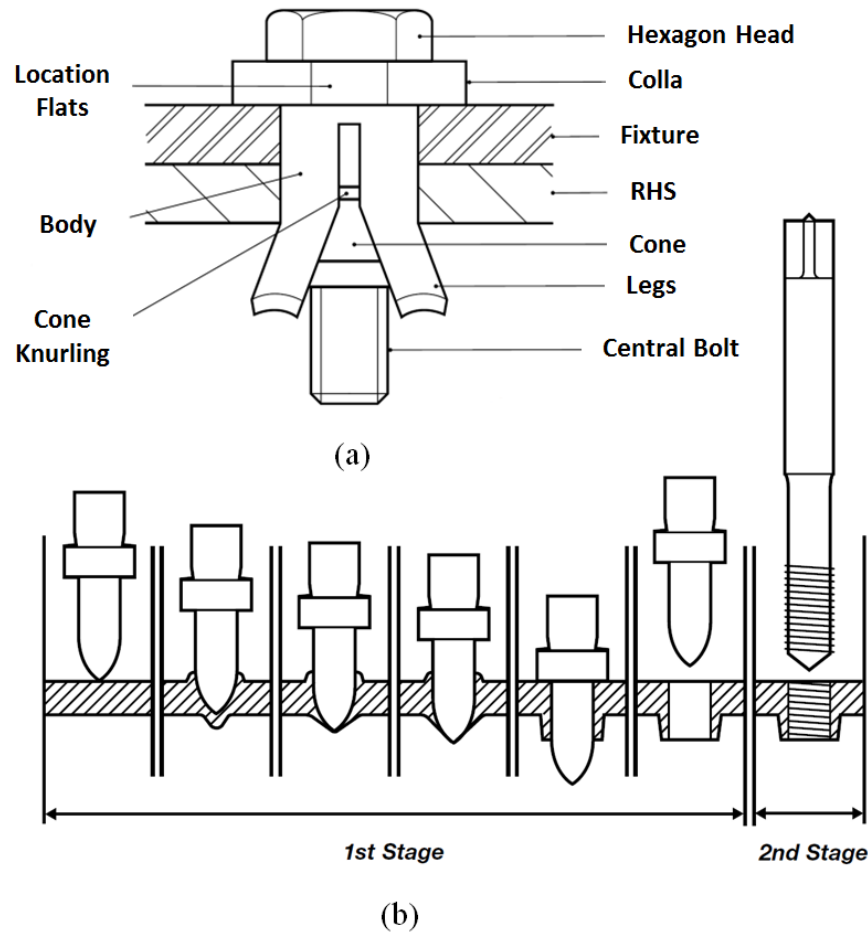


Figure 9: (a) Detail of five-part Hollo-Bolt, (b) Stages of the Flowdrill process (British Steel, 1997)

As part of an extensive research, France et al. (1999) tested fourteen specimens of partial depth and flush endplate connections with various details bolted to tubular columns using flowdrill connectors. The influences of connection details on the moment capacity and rotational stiffness of the connections were investigated. In addition, the effect of column axial load on the joint moment–rotation characteristic was examined. The specimens included different connection details, such as, endplate type (partial depth or flush), beam size, column tube thickness and bolt cross-centres. Tests results confirmed that these connections satisfy the EC3 criteria for pinned connections. From the moment–rotation characteristic of the end-plate connections it was concluded that the stiffness and strength enhanced significantly with the increase in endplate thickness, column wall thickness and beam depth.

Consequently, the designer may control the stiffness and strength of such joints by varying the end plate depth, end plate width, end plate thickness, bolt locations and column wall thickness.

Similarly, France et al. (1999a) reported on another series of tests of moment-resisting connections bolted to tubular columns. The specimens included details of various extended endplates, flush endplates and wall thicknesses of tubular column sections. The results indicated that this connections type is semi-rigid and it is in line with the design methods suggested by EC3.

2.2.5 Top- and Seat-Angle Connections

Top and seat angle connection consists of a seat angle and a top angle, as demonstrated in Figure 10. Top and seat angles can be fully bolted or bolted to the beam and welded to the face of column.

The AISC Specifications (1997) describe top- and seat-angle connection as follows: (1) the top-angle is used to provide lateral support for the compression flange of the beam; and (2) the seat-angle transfers only the vertical reaction of the beam to the column and should not be given a significant restraining moment at the end of the beam. However, according to the experimental results, this connection can transfer vertical reaction as well as some end moment from the beam to the column.

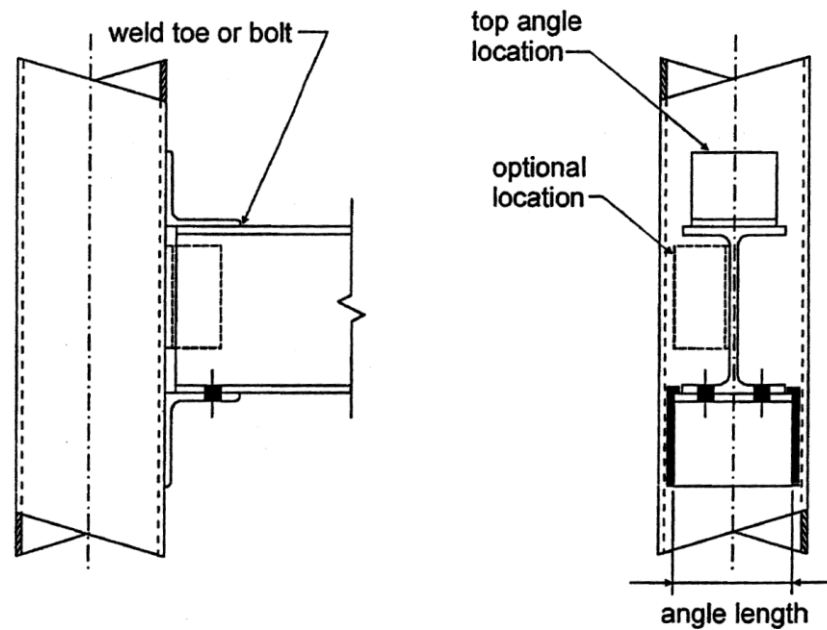


Figure 10: Top- and seat-angle connection (Kurobane, Packer, Wardenier, & Yeomans, 2004)

Based on the experiments done by Yang et al. (1999) on the unstiffened seated angle connections, the seat angle strength is significantly influenced by beam setback, angle thickness and the bolts that connect the angle to the flange of the supporting beam. Moreover, the thickness of the angle and the distance from the heel of the angle to the column flange bolts cause the most significant effect on $(M-\phi)$ behavior for top and seat angle connections.

Elghazouli et al. (2009) studied the experimental behaviour of top and seat angles connections bolted to tubular columns using blind connectors. A series of connection tests with different geometric arrangements and bolt properties were selected. The stiffness, strength, energy dissipation and failure mechanism were monitored and captured to assess the monotonic and cyclic response of such connections. They found that this form of connection is suitable for secondary or primary frame systems, depending on the specific structural configuration and loading conditions under consideration.

Málaga-Chuquitaype et al. (2010) proposed a new analytical model to evaluate the monotonic and cyclic response of top and seat angles connections bolted to tubular columns using blind connectors. The component method was used to estimate the initial stiffness and moment capacity of such connection. Moreover, the experimental study carried out by Elghazouli et al. (2009) was used to verify the analytical results. Based on the tests results, they conclude that the blind-bolt grade, angle thickness, column face slenderness and gauge distance can be considered as the key factors influencing the behaviour of semi-rigid blind-bolted connections.

2.2.6 Reverse Channel Connections (RCC)

As already stated in Section 1.1, the RCC can be considered as one of the most reliable solution to overcome the difficulty of access to the internal face of tubular columns by giving access from inside of the channel. Consequently, a considerable amount of literature has been published which were mainly concentrated on the fire and earthquake resistance of RCC and very limited research on its basic structural behaviour.

Experimental and numerical studies of RCC behaviour during fire were carried out by a number of researchers. For example, Ding and Wang (2007) conducted fire tests and reported that RCC has the potential to be developed into a robust connection characterized by high stiffness, strength, rotational capacity and ductility. Elsayaf et al. (2011) and Elsayaf and Wang (2012) (2013) used finite element modeling to study the behaviour of restrained structural subassemblies of RCC in fire. A series of experimental tests at elevated temperatures were carried out by Huang et al. (2013a) (2013). They confirmed that RCC not only provide a practical solution for connecting steel beams to composite columns but they also possess high ductility and strength. On the other hand, the structural behaviour of RCC under monotonic and

cyclic load was investigated by a number of researchers, such as, Elghazouli et al. (2009), Málaga-Chuquitaype and Elghazouli (2010a), Liu et al. (2012a) (2012) .

As a part of an extended experimental work, Liu et al. (2012a) conducted three tests on combined channel/angle configurations to examine the stiffness and capacity of their response under predominant shear loading conditions. The three tests comprised of two reverse channel connections with top and seat angles, which one of these with double web angels. Two different reverse channels cut from hot-rolled SHS tubes and different angle dimensions were also used. The test results show that the wall thickness of the reverse channel has significant effect on the connection stiffness and capacity. In addition, there was a great enhancement in stiffness and resistance of the reverse channel connections with double web angels compared with those of the connections with top and seat angles only. Similarly, Liu et al. (2012) also monitored the stiffness and capacity of combined channel/angle configurations under axial loading conditions. The results indicate that increasing the wall thickness of reverse channel gave a remarkable increase in both the initial stiffness and the stiffness and capacity of RCC. Moreover, the occurrence of inelastic axial mechanisms is proportional to the ratio of the relative widths of the column/reverse channel and beam/angle components.

In contrast, the recent research by Wang and Xue (2013) and AlHendi and Celikag (2015) appear to be the only publications to have included the influence of the geometrical configurations of reverse channel connections (RCC) on the moment-rotation ($M-\phi$) relationship. Wang and Xue (2013) carried out a limited number of experiments on RCC where all the tested connections were able to reach a rotational capacity of at least 0.03 rad, commonly found to be sufficient for plastic design.

They considered a number of parameters, such as, connection type (extended or flush endplate), reverse channel dimensions (thickness, width), orientation of the rectangular tube with or without concrete infill and their effect on the moment-rotation response of RCC. The mentioned parameters found to have significant effect on the connection stiffness, moment resistance and the rotational capacity. It was concluded that these connections can be designed to achieve semi-rigid/partial strength connections. Nevertheless, AlHendi and Celikag (2015) carried out an extensive parametric study which further investigated the above mentioned parameters and additional geometrical parameters. These geometric parameters include; the thickness of flush end-plate, the wall thickness of reverse channel cut from hot-rolled square hollow sections (SHS), the ratio of flush end-plate thickness to the wall thickness of reverse channel, the width of hot-rolled reverse channels, the ratio of reverse channel depth to SHS width for different types of channel, the nominal bolt diameter and the gage distance.

2.3 Moment-Rotation Models of Semi-rigid Connections

Beam-to-column connections have been the focus of research since the 1930's when the first major investigation was carried out to understand their behaviour. A significant amount of experimental research has been performed on semi-rigid connections where most of the steel beam-to-column connections act as semi-rigid connections (Jarmai & Farkas, 1998). Generally, the flexural behavior of a connection is best described by the moment-rotation ($M-\phi$) curve. The moment-rotation curve can be defined as a curve expressing the moment transmitted by the connection as a function of the relative rotation of the elastic lines of the connected members at their point of interaction. Figure 11 shows the typical moment-rotation

curves of most commonly used connections where rotational deformation of the connections are due to flexural action.

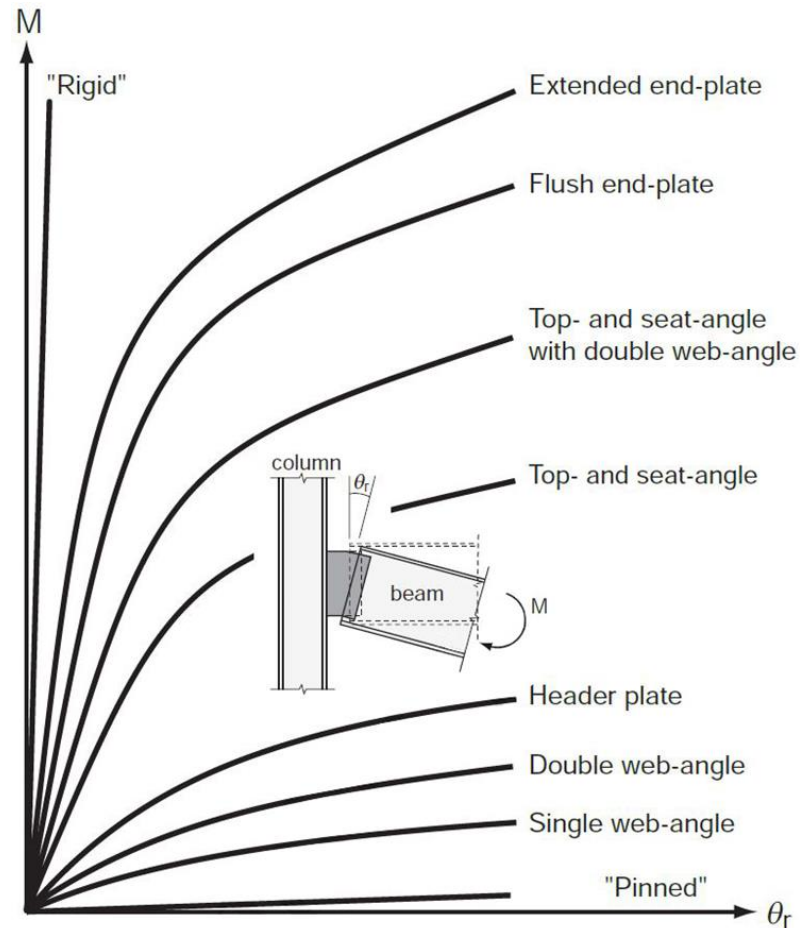


Figure 11: Typical moment-rotation curves of common connections (Chen, Kishi, & Komuro, 2011)

As illustrated in Figure 11, the extended end-plate connection behaves as a rigid connection and is considered to be the stiffest type of joint connection. The single web-angle behaves as a flexible connection and it is found to be the most flexible type of connection. In general, all ($M-\phi$) curves for the connections are nonlinear over the entire range of loadings.

In general, much effort has been focused in recent years toward determining connection ($M-\phi$) relationships experimentally and using the results to model the

connection behavior to be incorporated into the frame analysis computer program. There are several models which can be used for predicting the behaviour of beam-to-column joints, these are: empirical, analytical, mechanical, numerical and experimental.

2.3.1 Empirical Models

Empirical models are mainly based on empirical formulations which are used to express the parameters of the mathematical representation of the moment–rotation curve in terms of the geometrical and mechanical properties of beam-to-column joints. These formulations can be obtained using regression analyses of data which can be derived in different ways, such as: experimental testing, parametric analyses developed by means of Finite Element (FE) models, analytical models or mechanical models (Faella, Piluso, & Rizzano, 2000).

The early attempts; which used this approach to determine the effects of different connection geometries on moment-rotation behavior; have been made by Sommer (1969), Frye and Morris (1975), Picard et al. (1976), Altman et al. (1982), Ang and Morris (1984) and Goverdhan (1984). These attempts were made to fit standardized functions to the available experimental data. Frye-Morris model (1975) and Attiogbe-Morris model (1991) can be considered as examples about empirical models based on experimental results.

On the other hand, empirical formulations based on wide parametric studies by means of the FE Method (FEM) have been adopted by Krishnamurthy (1978a) and (1978), Krishnamurthy and Graddy (1976), Krishnamurthy et al. (1979), Kukreti et al. (1987).

As example of developing empirical models, based on a mechanical model, Faella et al. (1997) predicted both the flexural resistance and rotational stiffness of extended end-plate beam-to-column joints using component approach. In their study, more than 110,000 different configurations of extended end-plate joint were analyzed to provide the data required for regression analysis. The resulted empirical models were adopted by Eurocode 3 (CEN, 2005).

Recently, remarkable number of studies have been adopted empirical models to investigate the effect of semi-rigid joints on steel frame structures; such as, (Kameshki & Saka, 2001), (Hadianfard, 2003), (Hayalioglu MS, 2005), (Prabha , Marimuthu, Saravanan, & Jayachandran, 2010).

The empirical functions have proven to be applicable only to joints configurations used in deriving them (Attiogbe & Morris, 1991). This drawback has limited the pool of data that can be used in deriving the functions. It was shown also that the contribution of each parameter in the empirical model on the overall behaviour is obscure.

2.3.2 Analytical Models

Analytical models are constructed and used by several authors to obtain the initial stiffness and the ultimate moment capacity by means of the basic concepts of elastic structural analysis and limit design. On the basis of experimental observations, the sources of deformability and failure mechanisms of the connections are required to be identified as starting point. Then, the elastic analysis is used to predict the initial stiffness while the ultimate moment capacity is predicted by the method of virtual work; which depends on the balance between the internal and external work. Finally, the formulation of ($M-\phi$) relationships is provided based on the predicted initial

stiffness and ultimate moment capacity (Faella, Piluso, & Rizzano, 2000). Example of adopting this approach include Yee and Melchers (1985) model for bolted extended end-plate connections and Kishi and Chen model (1987) for top and seat angles with double web angles connections.

2.3.3 Mechanical Models

Mechanical or spring models conceive the joint by using a set of rigid and deformable components representing the behaviour of single elements. Each one is represented by an elastic spring characterized by a specific stiffness and strength which obtained from empirical relationships. The appropriate coupling of these springs in parallel and series provides the global stiffness of the connection.

Three main steps are required in order to develop a mechanical model; (1) identify the components of the joint that will provide significant deformation and failure of the joint; (2) determine the constitutive laws for each component of the joint using analytical, experimental or numerical means, and (3) assemble all of the components together to produce the moment–rotation curve for complete joint (Díaz, Martí, Victoria, & Querin, 2011).

Comparing with analytical model, mechanical model has the ability to simulate the curvilinear of the knee region of $M-\phi$ curve, while the modeling of such a region using analytical model required a curve fitting which in turn limited to the calibration of a shape factor (Faella, Piluso, & Rizzano, 2000).

The early attempts of adopting this model include Wales and Rossow (1983) for double web angle connections, Kennedy and Hafez (1984) for header-plate connections, and Chmielowiec and Richard (1987) for all types of cleated

connection. Since then, worthy research has been carried out to study the behaviour of joints and to introduce their effect in the analysis of structure; such as, Pucinotti (2001), Simões da Silva and Girão Coelho (2001), and Urbonas and Daniunas (2006).

2.3.4 Numerical Models

Numerical simulation started being used as a way to overcome the lack of experimental results; The use of FEM to study connection behaviour started in early 1970s, as the application of computers in solving structural problems became evident.

Since experimental research is lengthy and expensive process for understanding the connection behaviour then the availability of powerful computer facilities can be a suitable alternative for modeling structural behaviour of complex and lengthy parametric studies. Therefore, the finite element modeling was used to carry out several parametric studies based on computer simulation. Examples include Bose et al. (1972), Krishnamurthy and Graddy (1976), Chasten et al. (1992), Gebbeken et al. (1994), Sherbourne and Bahaari (1996), Troup et al. (1998), Yu et al. (2008), and Díaz et al. (2011).

2.3.5 Experimental Models

Since the aim of the experimental tests of beam-to-column joints is to account for their rotational behaviour, it is proven that experimental approach, despite being lengthy and expensive, provides the most accurate knowledge about this issue. Several researchers have tried to overcome these drawbacks by using different techniques, such as; empirical, analytical, mechanical, numerical models and then verify their reliability with existing experimental results. Consequently, there was a need to exploit and make real use of the available experimental data on beam-to-

column joints, so that researchers and designers are able to employ realistic representation of connections behaviour into the analysis and design of steel frame.

In 1984, Goverdhan collected the moment-rotation curves of 230 test results from the USA. These tests were carried out between 1950 and 1983 which were digitized to form Goverdhan data bank (1984). It includes tests on double web angle connections, single web angle/plate connections, header-plate connections, endplate connections and top and seat angle connections with or without web angles.

The first European data bank on steel connections was developed in 1985. Nethercot (1985) conducted a literature survey for more than 70 experimental studies between 1951 and 1985. Nethercot data bank includes those examined by Goverdhan as well as T-stub connections with and without web angles.

In the USA, Kishi and Chen (1986) developed Steel connection data bank (SCDB) which collected over 303 experimental tests from all over the world carried out from 1936 to 1986. Various connection typologies, such as; single angle web cleat/plate connections, double angle web cleat connections, top and seat angle cleats connections with or without web angles, extended and flush end-plate connections and header-plate connections are included in the SCDB data bank.

In 1992, the second European data bank on steel connections was developed by Arbed Recherches (1991) and Aachen University (1992). They developed SERICON data bank which covered only the European test results including single joint

Chapter 3

NUMERICAL MODELLING OF REVERSE CHANNEL CONNECTIONS (RCC) TO TUBULAR COLUMNS

3.1 Introduction

The aim of this research is to gain a qualitative understanding of the influence of geometrical configurations and materials properties of reverse channel connections (RCC) on the moment-rotation ($M-\phi$) response. Therefore, this chapter will employ the general finite element software ABAQUS (v.6.12) to numerically model the monotonic behaviour of reverse channel flush end-plate connections. The simulations were conducted using 3-D brick elements to enable detailed structural behaviour to be obtained. For validation, this research compared the simulation and test results for five RCC tests recently conducted by Wang and Xue (2013). As part of the validation study, sensitivity studies on the mesh size, the effect of friction and the effect of loading speed on moment-rotation response were performed and their results will be presented in this chapter.

3.2 A Brief Summary of Previous Experimental Work

The tests on RCC conducted by Wang and Xue (2013) were aimed to study the moment-rotation characteristics of reverse channel connections to tubular columns. They considered a number of parameters, such as, connection type (extended or flush endplate), reverse channel dimensions (thickness, width), orientation of the rectangular tube with or without concrete infill and their effect on the moment-rotation response of RCC. Table 1 and 2 summarize the measured dimensions and material properties of test connections. The test setup is well explained in reference

(Xue, 2012) where all the tests were arranged in a double-sided joint configuration, as shown in Figure 12. The ends of the beams were set on roller supports while a displacement-controlled loading was applied at the central stub column. The following parameters were used to investigate the effects of different geometric parameters on moment-rotation responses of RCC: the flush end-plate thickness (t_p), height (h_{EP}) and the reverse channel leg length (m), web width (w_c) and thickness (t_w).

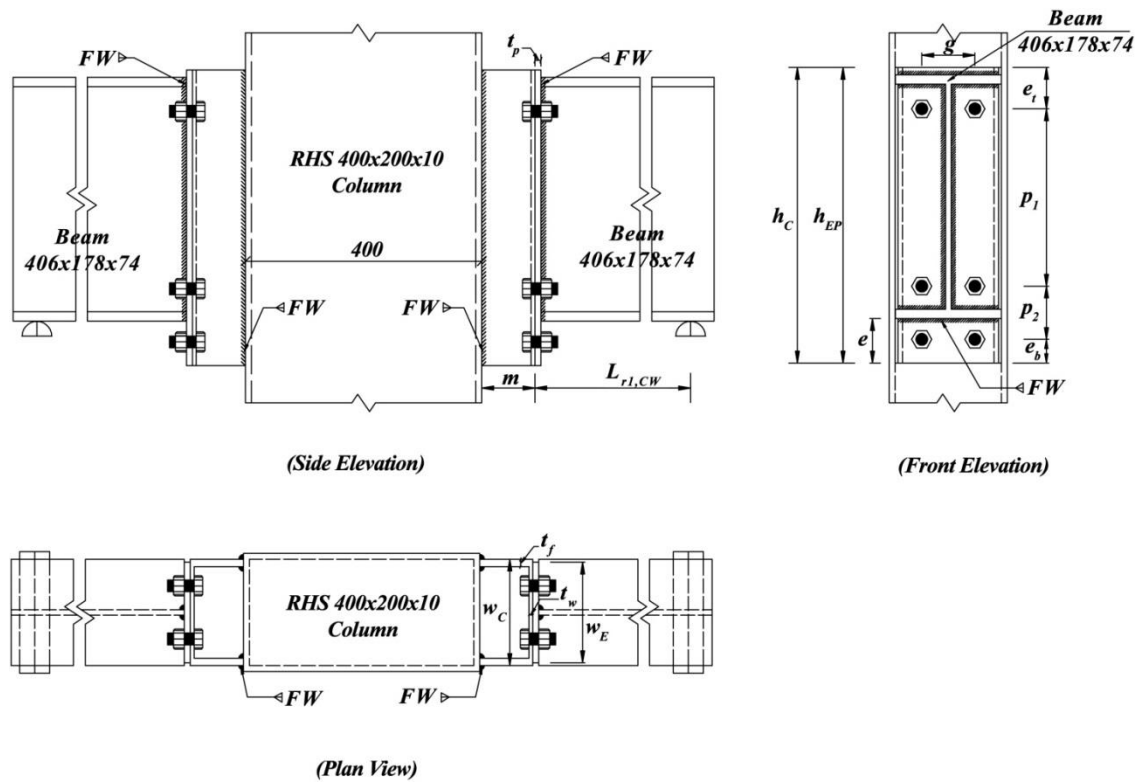


Figure 12: Reverse channel connection geometries

Among all test specimens, five connections were selected where flush end-plate was connected to the narrow side of column. These specimens were used in the verification denoted as Test 1-5. The beam and column sections used were UB 406x178x74 and RHS 400x200x10, respectively, for all tests. Three different reverse channel sections of 180x90x26, 180x75x20 and 150x90x24 and different flush end-plate dimensions were also used (Table 1). The mechanical properties of

different steel components of RCC were obtained from tensile coupon tests. The details of yield and ultimate stress, Young's modulus and ultimate strain are given in Table 2. The steel grade used for beams and columns was S355 and for flush end-plates and channel sections was S275. Grade 8.8 M20 (20 mm diameter) standard bolts were employed in all tests. All of these bolts were hand tightened without any preloads.

3.3 Finite Element Modeling

The general-purpose finite element explicit solver, ABAQUS/ Standard (2012), was employed to conduct 3-D nonlinear FE simulations. This solver is beneficial for solving not only the complicated contact problems but also the model with large rotations and large deformations without generating numerical convergence difficulties (Yu, Burgess, Davison, & Plank, 2008). In order to capture the large deformation and local instability effects in the 3-D FE models, both material and geometric non-linearities were considered. The solid element C3D8R available in the ABAQUS (2012) element library was used to model the reverse channel connection components.

Table 1: Schedule of test specimens (Wang & Xue, 2013)

Test	Channel Section (S275)	Endplate dimensions (mm)	Number of bolts	Dimensions (mm) (Figure 12)														
				$L_{r1,CW}$	h_C	w_C	m	t_f	t_w	h_{EP}	w_E	t_p	e_t	p_1	p_2	e_b	e	g
1	180 × 90 × 26	500 × 10 × 170	12	810	500	180	90	12.5	6.5	500	170	10	70	300	90	40	75	90
2	180 × 90 × 26	500 × 5 × 170	12	600	500	180	90	12.5	6.5	500	170	5	70	300	90	40	75	90
3	180 × 75 × 20	500 × 10 × 170	12	825	500	180	75	10.5	6.0	500	170	10	70	300	90	40	75	90
4	150 × 90 × 24	500 × 10 × 170	12	810	500	150	90	12.0	6.5	500	170	10	70	300	90	40	75	90
5	180 × 90 × 26	440 × 10 × 170	8	600	440	180	90	12.5	6.5	440	170	10	70	300	-	70	15	90

Note: Beam Section (Grade S355, UB 406 × 178 × 74 (flange width 179.5 mm, overall depth 412.8 mm, flange thickness 16 mm, web thickness 9.5 mm));

Column Section (Grade S355, Rectangular Hollow Section (RHS) 400 × 200 × 10 mm) were used for all specimens.

Table 2: Materials properties of reverse channel connection specimens (Wang & Xue, 2013)

Coupon	Test involved	Young's modulus (MPa)	Yield stress (MPa)	Ultimate stress (MPa)	Ultimate strain (%)
Beam web	Test 1-5	218,660	389	611	20.00
Beam flange	Test 1-5	218,123	389	612	18.30
Column tube	Test 1-5	192,415	425	656	19.80
Channel web (180 × 90 × 26)	Test 1, 2, 5	220,054	352	625	17.69
Channel flange (180 × 90 × 26)	Test 1, 2, 5	214,524	315	637	20.25
Channel (180 × 75 × 20)	Test 3	215,917	311	599	19.63
Endplate (10 mm thk)	Test 1, 3-5	202,538	300	689	21.00
Endplate (5 mm thk)	Test 2	232,373	346	630	27.05

Figure 13 shows a typical finite element mesh for the structural assembly. There are three parameters that control the generation of the FE; the number of elements through the thickness (n_{et}), the length of elements close to the connection (l_{en}) and the length of the elements far from the connection (l_{ef}). The mesh used has $n_{et} = 3$, $l_{en} = 7$ mm and $l_{ef} = 25$ mm. The analysis was continued until the ratio of the kinetic energy to the internal energy increased to more than 10% or the reaction force at the support suddenly dropped (Yu, Burgess, Davison, & Plank, 2008).

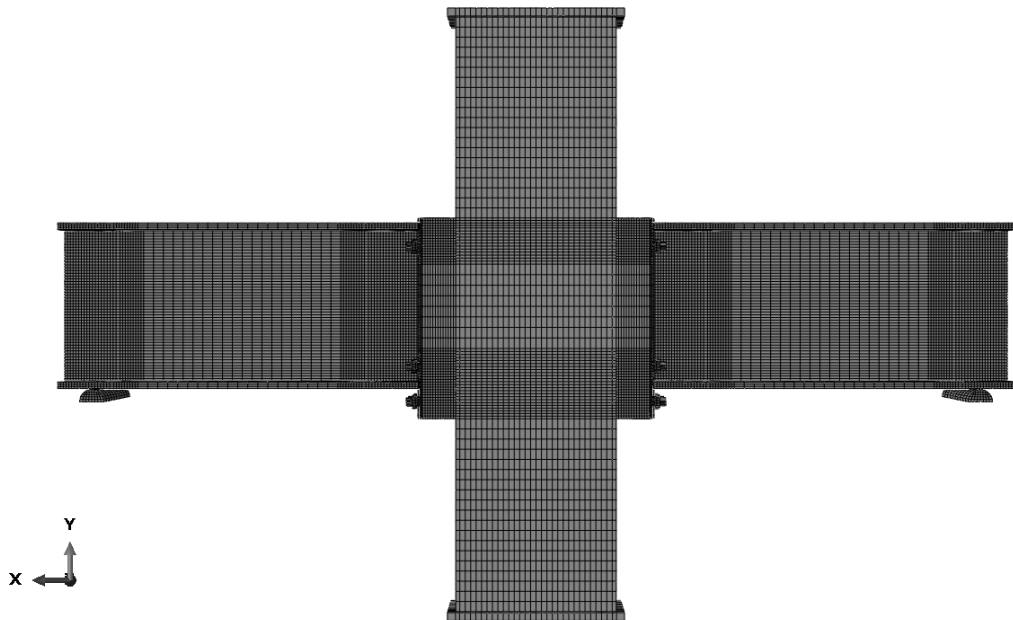


Figure 13: Typical finite element mesh of RCC assembly

3.3.1 Boundary Conditions and Contact

The boundary conditions of the FE models were in line with those in the tests. Since the beams were supported on two rollers, which allowed the beams to rotate about Z-direction (Figure 14), the bottom faces of these rollers were fixed in all three directions. Moreover, the top and bottom flanges of the beams over the roller supports were restrained against lateral movement of the beams in Z-direction, which simulated lateral bracing supports in tests.

The contact interaction of the RCC components was defined as surface-to-surface contact, with a small sliding option. ‘Hard contact’ was used for the normal contact behaviour with a friction coefficient of 0.33 in the tangential direction. The contact pairs between the bolt shanks-to-bolt holes, bolt heads-to-interior channel web, nuts-to-flush end-plate, end-plate-to-channel web and roller support-to-lower flange of beam were assigned. No prestressing to the bolts was considered. To represent the welded connection of the flush end-plate-to-the beam and the channel flanges-to-the column face, the tie constraints available in the ABAQUS (2012) constraints library were applied to all nodal degrees of freedom along the weld lines.

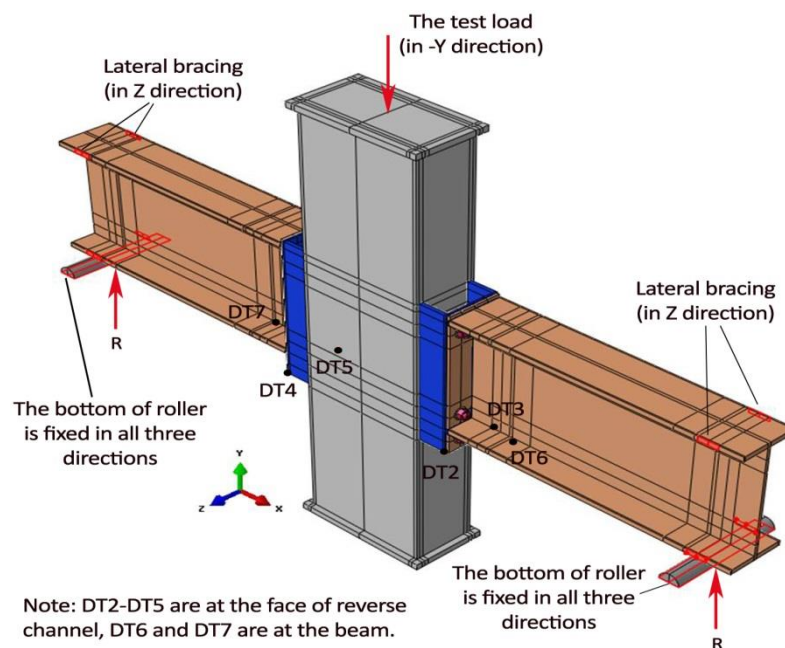


Figure 14: Boundary conditions, reference points used to measure the vertical displacements, and loading direction of RCC assembly

3.3.2 Material Properties

The material behavior used for joint (beam, column, channel, flush end-plate, and bolts) was modeled by means of the quadrilinear stress–strain curve as given by

Mohamadi-shooreh and Mofid (2008) in Figure 15. This stress–strain model was adopted with measured values of the yield stress and ultimate stress obtained from coupon tests (Table 2). For the materials of steel sections, the tangential stiffness beyond the yield point was defined as 2% of the initial modulus of elasticity up to $11\varepsilon_y$. The relevant strain for the ultimate stress was $120\varepsilon_y$ (Figure 15(a)). For the bolt material, including shank and head, the proof strain was considered to occur at a strain of $3\varepsilon_y$ followed by its related ultimate stress at $8\varepsilon_y$. The flat line up to the strain $1.05\varepsilon_u$ was considered (Figure 15 (b)) (Mohamadi-shooreh & Mofid, 2008).

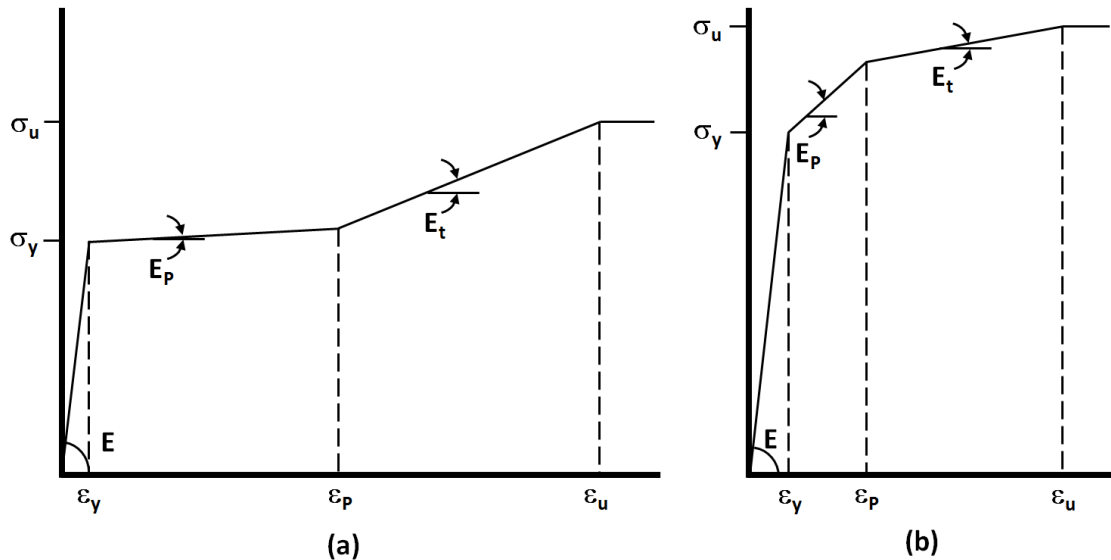


Figure 15: Idealized material behavior used in the FEM analysis for: (a) Beam, column, channel, and end plate (b) High-strength bolts (Mohamadi-shooreh & Mofid, 2008)

In order to represent the material nonlinear effects, the isotropic elastic-plastic multi-linear properties combined with the von Mises yield criterion were used. The classical metal plasticity model in ABAQUS (ABAQUS, 2012) was used to define the non-linear behavior of materials. The nominal stress and nominal strain in the stress–strain curve of the coupon tests were converted into the multi-linear curve of true stress (σ) and true plastic strain (ε_{pl}). The *ELASTIC option was used to assign

the value of the Young's modulus and the Poisson's ratio. The *PLASTIC option was also used for defining the plastic part of the stress–strain curve.

3.3.3 Moment-Rotation Curves

The flexural behavior of RCC is best described by the moment-rotation (M - ϕ) curve where the applied bending moment, M , is a function of the relative rotation of the connected members, ϕ . For verification process, the beam rotation was assumed to be equal to the connection rotation. Hence, the difference between the vertical displacements at beam location (DT6) and at the face of reverse channel (average of DT2-DT3) divided by the horizontal distance between the two points were used to calculate the connection rotation (Figure 14). Connection moment was calculated by multiplying the beam end reaction with its distance to the face of the reverse channel. These data were used to obtain the moment-rotation curves. The main parameters that were used to define the moment-rotation relationship in this study are given in Figure 16 and the characteristics are defined as follows:

- a. Stiffness: the initial stiffness of the joint, $S_{j,in}$, the post-yield stiffness, $S_{j,P}$, the secant stiffness, S_j , which is equal to one-third of the initial stiffness (CEN, 2005).
- b. Resistance: the plastic flexural resistance of the joint, $M_{j,R}$, the design moment resistance of the joint, $M_{j,Rd}$, the ultimate flexural resistance of the joint, $M_{j,ult}$.
- c. Rotation: the rotation corresponding to the plastic flexural resistance, $\phi_{j,R}$, the rotation at which the moment resistance first reaches the design moment resistance of the joint, $\phi_{j,x}$, the rotation corresponding to the ultimate flexural resistance, $\phi_{j,ult}$.

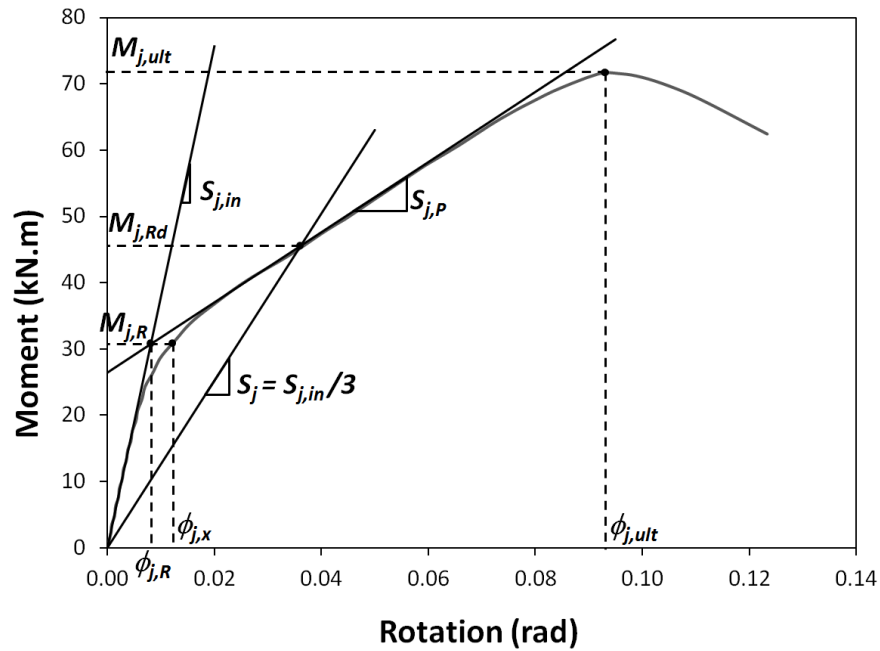


Figure 16: Main characteristics of the moment-rotation curves

3.3.4 Sensitivity Study Results

The calculation time and accuracy of numerical simulation results are significantly affected by many factors, such as, the mesh size, friction, loading speed, etc. 268 FE joint models were used for sensitivity analysis. The RCC in Test 1 is a reference test used by Wang and Xue (2013). Therefore, it is used as an example to show how the sensitivity study was performed on the mesh size, the effect of friction and the effect of loading speed on moment-rotation response.

3.3.4.1 Mesh Sensitivity

Since explicit solver was used for numerical simulations, this may raise serious concern about the mesh size (Yu, Burgess, Davison, & Plank, 2008). On the other hand, the use of refined mesh will increase the number of degrees of freedom which in consequence consume too much computer time. Hence, a mesh sensitivity study was carried out to choose an optimal mesh. Four mesh sizes were considered; coarse, regular, fine and extra-fine. The characteristics of these mesh sizes are as given by Díaz et al. (2011). The results of this sensitivity study are presented in Figure 17,

where the ordinates represent the calculation time required in hours on right side and the ratio of the design moment resistance values ($M_{j,Rd,FE} / M_{j,Rd,Exp}$) on the left side and the abscissa gives the number of elements in the mesh.

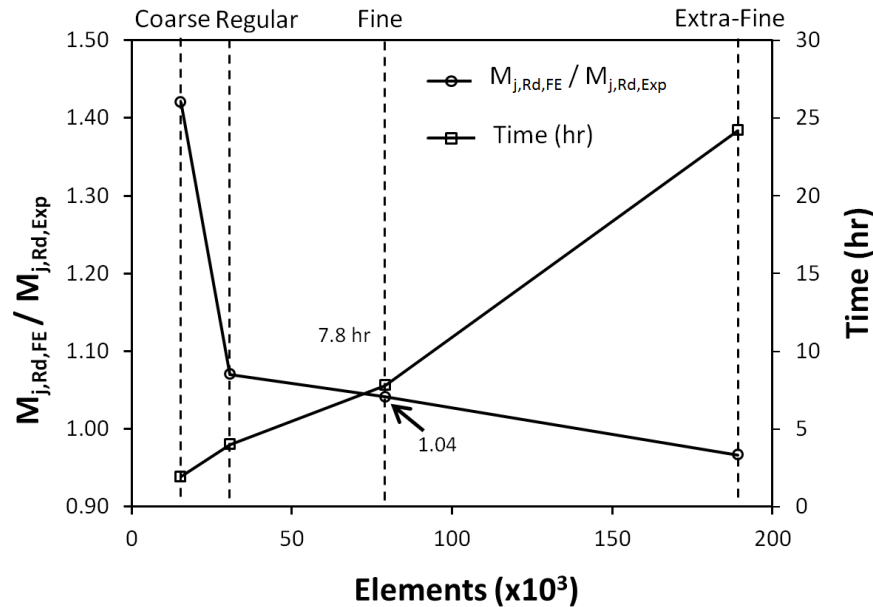


Figure 17: Effect of number of elements in the mesh on the calculation time and the RCC response of Test 1

It can be seen that the fine mesh produced an error of 0.4% in 7.8 h whereas the regular mesh took 4 h to produce an error of 0.7% (Figure 5). On the other hand, the extra-fine mesh took 24.2 h to produce an error of 0.3%. Since the fine mesh uses three elements across all thicknesses, which is minimum recommended number of elements by Yu et al. (2008), then it was accepted as an optimal mesh size and selected for this study. The mesh selected has $n_{et} = 3$, $l_{en} = 7\text{mm}$ and $l_{ef} = 25\text{mm}$.

3.3.4.2 Effect of Friction

The friction between components can substantially affect the moment-rotation relationship of steel connection, especially with higher moments and stiffer connecting elements (Citipitioglu, Haj-Ali, & White, 2002). To evaluate this effect, a model is used to study the effect of friction on the response of the RCC by varying

the friction coefficient from 0.25 to 0.6. Compared with the experimental results of reference (Wang & Xue, 2013), the errors in predicting initial rotational stiffness ($S_{j,in,FE}$) and the design moment resistance value ($M_{j,Rd,FE}$) with different friction coefficients are demonstrated in Figure 18.

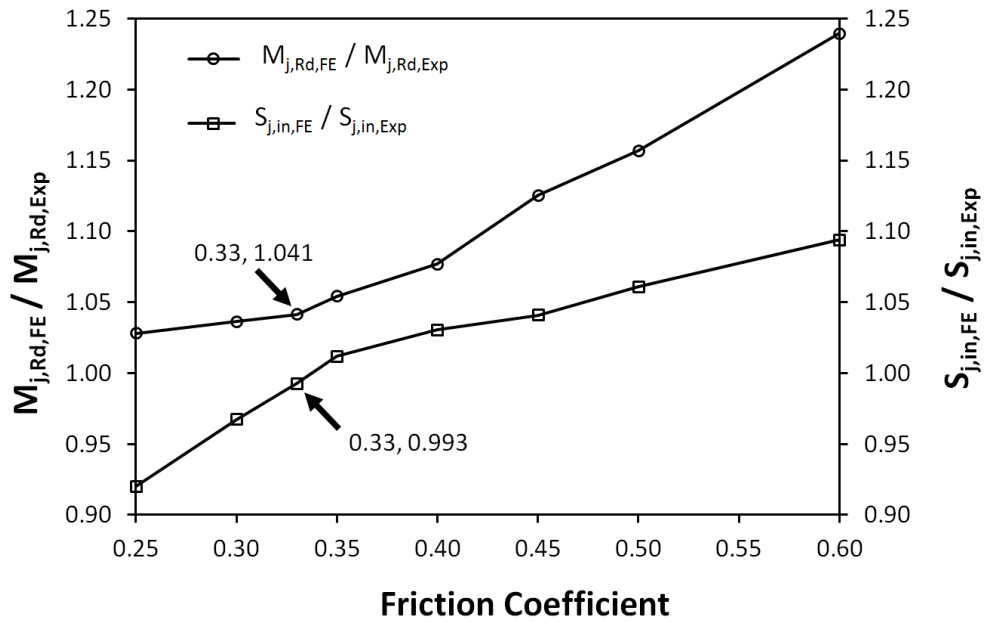


Figure 18: Effect of friction on the RCC response of Test 1

As shown in Figure 18, the friction coefficient value of 0.33 produced an error of 0.4% in the value of initial rotational stiffness and 0.03% in the design moment resistance value, where less predicted error than other coefficient values were produced. It may be concluded that the results were particularly sensitive to the magnitude of the friction coefficient and the value of 0.33 is suggested for numerical analysis.

3.3.4.3 Load Speed Sensitivity

For simulations of RCC, it is proposed to control the loading speed because this allows accurate response without generating numerical convergence difficulties. For this purpose, as suggested by Yu et al. (2008), different loading durations varied from 0.1 to 1 second were used to assess the maximum viable loading speed. The

results of this sensitivity study suggested that the appropriate loading time would be 0.16 second for simulations of RCC hence it provides a satisfactory solution if accuracy is required (Figure 19).

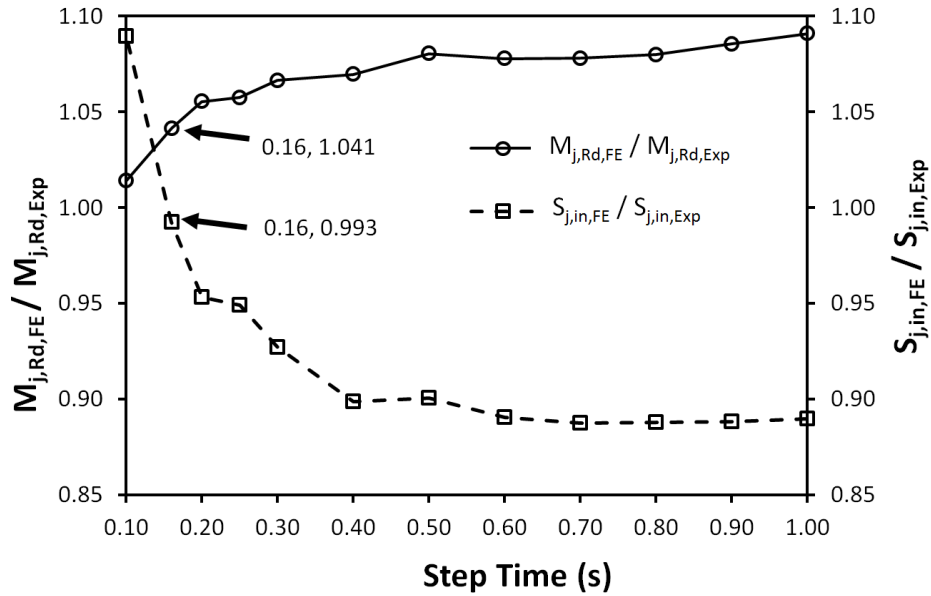


Figure 19: Effect of loading speed on the RCC response of Test 1

3.4 Verification of Finite Element Simulations

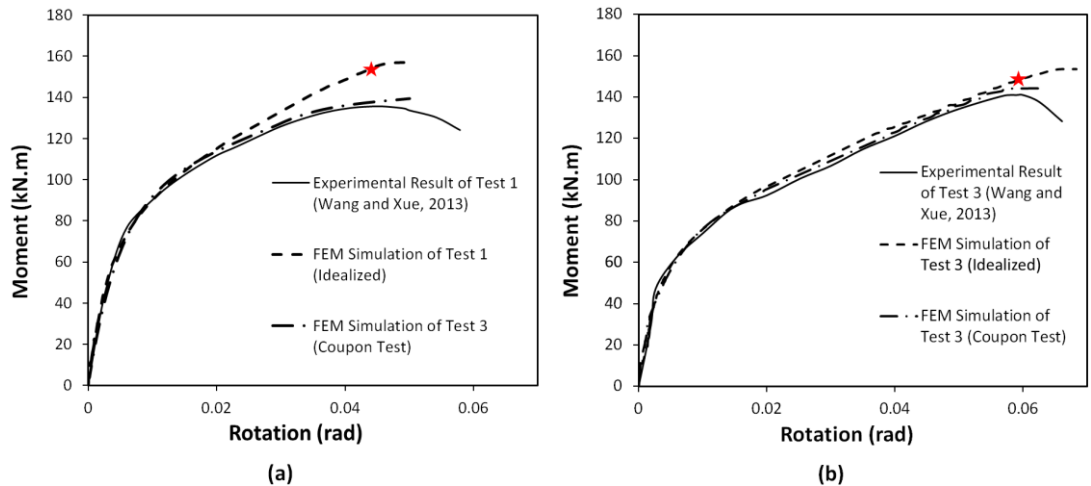
The finite element model of RCC developed in this study was verified against the aforementioned tests in section 3.2 by Wang and Xue (2013). The test results included the failure modes, initial stiffness, $S_{j,in}$, the design moment resistance, $M_{j,Rd}$, and the ultimate flexural resistance, $M_{j,ult}$, of the joint. There were variations in the results of Tests 2 and 4 owing to the lack of data given for material properties of bolts and channel, as stated in reference (Wang & Xue, 2013). Furthermore, the slippage observed at the ends of beams, between the beam and the roller supports, could potentially cause reduction in reaction values and therefore abrupt decrease in the stiffness and moment capacity. Consequently, Tests 2 and 4 were not included in the comparison between the tests and finite element analysis summarized in Table 3. Figure 20 compares the $M-\phi$ behaviour of the FE simulations of RCC with

experimental RCC Tests 1, 3 and 5. The FE simulations consider both the idealized curve and the stress-strain relationships of the coupon tests (Xue, 2012). According to Figure 20, the $M-\phi$ curve obtained by using stress-strain relationship of the coupon tests is in very good agreement with the experimental $M-\phi$ curves. This indicates that the FE modeling is satisfactory.

Table 3: Comparison between test and finite element results

Test	Test (Wang & Xue, 2013)				FE				$\frac{S_{j,in,Exp}}{S_{j,in,FE}}$	$\frac{M_{j,RD,Exp}}{M_{j,RD,FE}}$	$\frac{M_{j,ult,Exp}}{M_{j,ult,FE}}$
	$S_{j,in,Exp}$ (kN.m/rad)	$M_{j,RD,Exp}$ (kN.m)	$M_{j,ult,Exp}$ (kN.m)	Failure mode	$S_{j,in,FE}$ (kN.m/rad)	$M_{j,RD,FE}$ (kN.m)	$M_{j,ult,FE}$ (kN.m)	Failure mode			
1	17908	108.50	136.01	CWF	17775	113.00	153.86	CWF	0.99	1.04	1.13
3	20076	79.10	141.03	BPO	18807	83.98	148.49	BPO	0.94	1.06	1.05
5	7498	80.17	95.18	CWF	7622	85.59	105.16	CWF	1.02	1.07	1.10
Mean	-	-	-	-	-	-	-	-	0.98	1.06	1.10
COV	-	-	-	-	-	-	-	-	0.04	0.01	0.04

Note: CWF denotes Channel Web Fracture, BPO denotes Bolt Pull-Out
CWF evaluated by fracture index (PEEQ Index in ABAQUS)



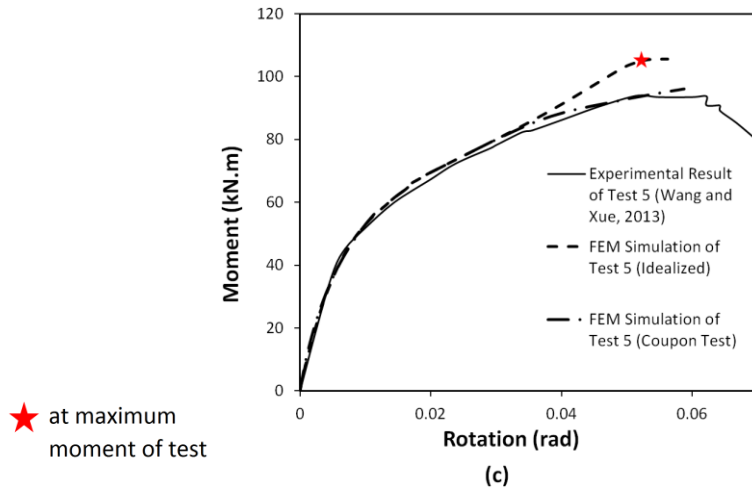


Figure 20: Moment-rotation curves from experimental and FE models for RCC connections of: (a) Test 1, (b) Test 3 and (c) Test 5

On the other hand, it can also be seen from Table 3 that the tests results and the FE simulations with idealized stress-strain curve are in very good agreement. The predicted failure modes are agreed well with the observed failure modes for all test specimens. Moreover, the mean values of $S_{j,in,Exp} / S_{j,in,FE}$, $M_{j,Rd,Exp} / M_{j,Rd,FE}$ and $M_{j,ult,Exp} / M_{j,ult,FE}$ ratios are 0.98, 1.06 and 1.10 and the coefficient of variation (COV) values are 0.04, 0.01 and 0.04, respectively (Table 3).

Chapter 4

EFFECT OF GEOMETRICAL PARAMETERS ON $M-\phi$ CHARACTERISTICS OF RCC

4.1 Introduction

The effect of geometrical configurations of reverse channel flush end-plate connections on the moment-rotation ($M-\phi$) relationship under monotonic loading are presented in this chapter. The results of this numerical study were obtained by using ABAQUS. For this purpose, the following geometric parameters were considered; the thickness of flush end-plate, the wall thickness of reverse channel cut from hot-rolled square hollow sections (SHS), the ratio of flush end-plate thickness to the wall thickness of reverse channel, the width of hot-rolled reverse channels, the ratio of reverse channel depth to SHS width for different types of channel, the nominal bolt diameter and the gage distance. Therefore, thirty reverse-channel joints with different connection configurations; varying dimensions of column sizes, beam sections and channel types were investigated.

4.2 Parametric Study

Following the successful verification process in the previous chapter, a new 3D finite element model was developed by using ABAQUS (v.6.12) to investigate the effects of reverse channel geometry and thickness of flush end-plate on the behavior and strength of RCCs. In order to avoid possible reduction in stiffness and moment capacity due to slippage and also to facilitate the direct monitoring of the deformation of the column web panel zone, a cantilever arrangement as suggested by Díaz et al. (2011) (Figure 21), was used for the new 3-D FEM. The height of the

column, H_{col} , and the length of the beam were set to be equal to 3625 mm and 1550 mm, respectively. In addition, the stiffener thickness of the beam under the applied load was considered to be equal to that of the flange thickness of the beam (Díaz, Victoria, Martí, & Querin, 2011).

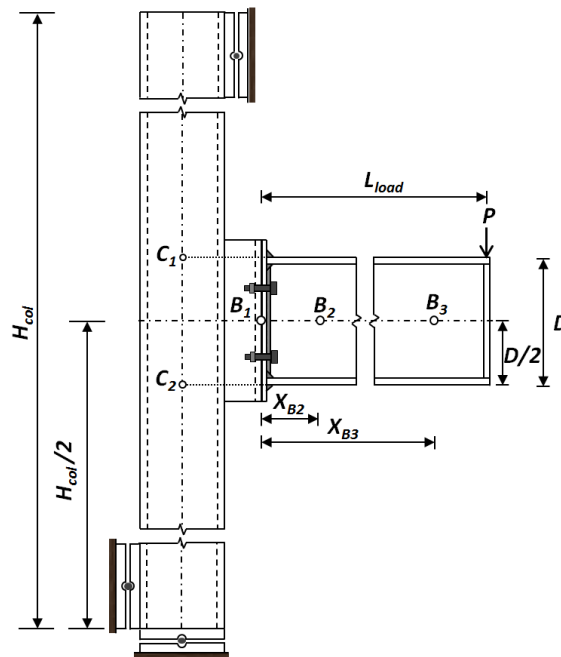


Figure 21: The cantilever arrangement and locations of the reference points that are used to measure the displacement

Table 4 summarizes the dimensions of the 30 reverse-channel joints considered in this study. All tests were divided into five groups (G1 to G5). The first group of connections (G1) had varied flush end-plate thicknesses from 12 to 25 mm so the effect of flush end-plate thickness on the joint behaviour can be assessed. The groups G2-G4 were formed to investigate the influence of reverse-channel geometry; in G2, reverse channels of five different sizes, cut from hot-rolled SHS tubes, were modeled to investigate the effect of wall thickness of channel.

Table 4: Schedule of test specimens in the parametric study

Group	Specimen	Column Section (S355)	Beam Section (S355)	Channel (S355)						Endplate (S355)				
				Section	h_c	w_c	m	t_f	t_w	h_{EP}	w_E	t_p	e_t	g
G1	S1	SHS180 × 10	UKB356 x 127 x 33	UKPFC180 x 90 x 26	400	180	90	12.5	6.5	400	180	12	72	90
	S2	SHS180 × 10	UKB356 x 127 x 33	UKPFC180 x 90 x 26	400	180	90	12.5	6.5	400	180	15	72	90
	S3	SHS180 × 10	UKB356 x 127 x 33	UKPFC180 x 90 x 26	400	180	90	12.5	6.5	400	180	18	72	90
	S4	SHS180 × 10	UKB356 x 127 x 33	UKPFC180 x 90 x 26	400	180	90	12.5	6.5	400	180	20	72	90
	S5	SHS180 × 10	UKB356 x 127 x 33	UKPFC180 x 90 x 26	400	180	90	12.5	6.5	400	180	22	72	90
	S6	SHS180 × 10	UKB356 x 127 x 33	UKPFC180 x 90 x 26	400	180	90	12.5	6.5	400	180	25	72	90
G2	S7	SHS200 × 10	UKB305 x 165 x 40	cut from SHS200 × 6.3	339	200	90	6.3	6.3	339	200	18	67	100
	S8	SHS200 × 10	UKB305 x 165 x 40	cut from SHS200 × 8	339	200	90	8.0	8.0	339	200	18	67	100
	S9	SHS200 × 10	UKB305 x 165 x 40	cut from SHS200 × 10	339	200	90	10.0	10.0	339	200	18	67	100
	S10	SHS200 × 10	UKB305 x 165 x 40	cut from SHS200 × 12.5	339	200	90	12.5	12.5	339	200	18	67	100
	S11	SHS200 × 10	UKB305 x 165 x 40	cut from SHS200 × 16	339	200	90	16.0	16.0	339	200	18	67	100
G3	S12	SHS260 × 10	UKB533 x 210 x 92	cut from SHS260 × 10	583	260	50	10.0	10.0	583	259	25	75	100
	S13	SHS260 × 10	UKB533 x 210 x 92	cut from SHS260 × 10	583	260	75	10.0	10.0	583	259	25	75	100
	S14	SHS260 × 10	UKB533 x 210 x 92	cut from SHS260 × 10	583	260	90	10.0	10.0	583	259	25	75	100
	S15	SHS260 × 10	UKB533 x 210 x 92	cut from SHS260 × 10	583	260	100	10.0	10.0	583	259	25	75	100
	S16	SHS260 × 10	UKB533 x 210 x 92	cut from SHS260 × 10	583	260	125	10.0	10.0	583	259	25	75	100
	S17	SHS260 × 10	UKB533 x 210 x 92	cut from SHS260 × 10	583	260	130	10.0	10.0	583	259	25	75	100
	S18	SHS260 × 10	UKB533 x 210 x 92	cut from SHS260 × 10	583	260	150	10.0	10.0	583	259	25	75	100
	S19	SHS260 × 10	UKB533 x 210 x 92	cut from SHS260 × 10	583	260	150	10.0	10.0	583	259	25	75	100
G4	S19	SHS200 × 10	UKB356 x 127 x 33	UKPFC180 x 90 x 26	400	180	90	12.5	6.5	400	180	15	72	90
	S20	SHS250 × 10	UKB356 x 127 x 33	UKPFC180 x 90 x 26	400	180	90	12.5	6.5	400	180	15	72	90
	S21	SHS300 × 10	UKB356 x 127 x 33	UKPFC180 x 90 x 26	400	180	90	12.5	6.5	400	180	15	72	90
	S22	SHS400 × 10	UKB356 x 127 x 33	UKPFC180 x 90 x 26	400	180	90	12.5	6.5	400	180	15	72	90
	S23	SHS250 × 10	UKB305 x 165 x 40	cut from SHS200 × 10	339	200	90	10.0	10.0	339	200	18	67	100
	S24	SHS400 × 10	UKB305 x 165 x 40	cut from SHS200 × 10	339	200	90	10.0	10.0	339	200	18	67	100
	S25*	SHS260 × 10	UKB457 x 191 x 106	UKPFC260 x 90 x 35	513	260	90	14.0	8.0	513	238	22	82	140
S26*	SHS260 × 10	UKB457 x 191 x 106	UKPFC260 x 90 x 35	513	260	90	14.0	8.0	513	238	22	82	140	
S27*	SHS260 × 10	UKB457 x 191 x 106	UKPFC260 x 90 x 35	513	260	90	14.0	8.0	513	238	22	82	140	
S28	SHS250 × 10	UKB457 x 191 x 106	cut from SHS250 × 12.5	513	250	100	12.5	12.5	513	238	22	72	140	
S29	SHS250 × 10	UKB457 x 191 x 106	cut from SHS250 × 12.5	513	250	100	12.5	12.5	513	238	22	72	120	
S30	SHS250 × 10	UKB457 x 191 x 106	cut from SHS250 × 12.5	513	250	100	12.5	12.5	513	238	22	72	100	

*Note: S25-S27 had varied bolt diameter from 16, 20 and 24 mm, respectively.

In G3, hot-rolled reverse channels of seven different widths were used to examine the influence of width of channel. Two different sizes of reverse channels, hot rolled standard section and cut from hot-rolled SHS tubes, were also used to examine the

influence of the ratio of channel depth to SHS width in G4. The remaining group G5 is formed to investigate the influence of the diameter of bolt and the gage distance; the first series (S25-S27) had varied bolt diameter of 16, 20 and 24 mm, respectively and the second series (S28-S30) had varied gage distance of 100, 120 and 140 mm, respectively.

The finite element models for all joints were prepared according to section 3.3. The steel grade used for beams, columns, flush end-plates and channel sections was S355 and Grade 8.8 was used for standard bolts. The quadri-linear stress–strain curve (Figure 15) was adopted with the values of the yield stress and ultimate stress obtained from Eurocode 3 Part 1-1 (CEN, 2005). The typical FE mesh for the cantilever arrangement is given in Figure 22.

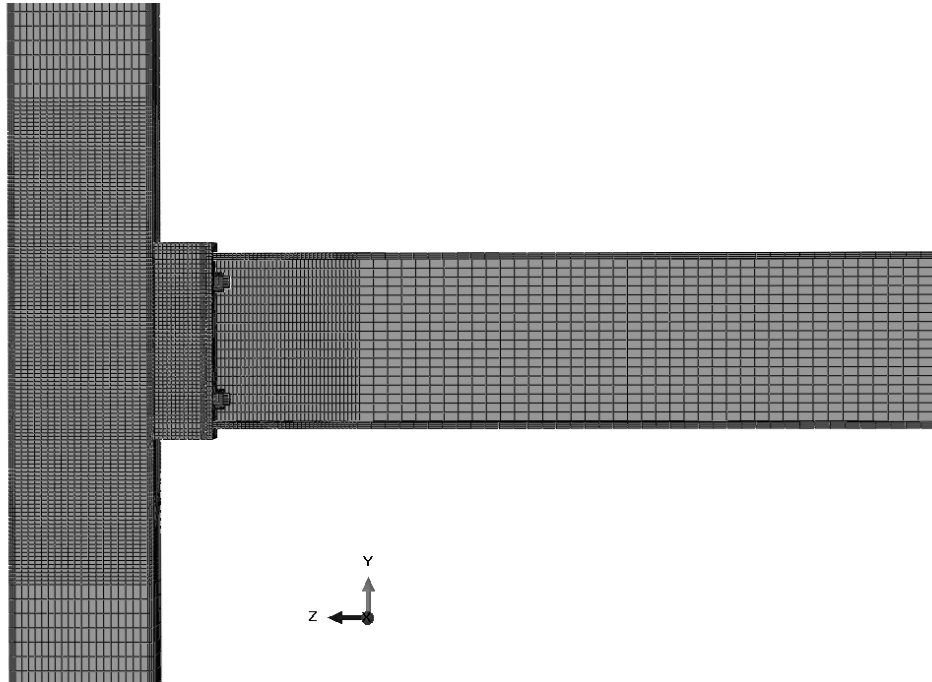


Figure 22: The typical FE mesh for the cantilever arrangement

According to Eurocode 3 Part 1-8 (CEN, 2005), the main sources of deformability for single-sided joint are the connection and the column web panel. The deformation

of the connection is related to its components while for the column web it is associated with the compressive and tensile forces acting on the column web. The shear force acting on column web panel is responsible for the shear deformation in that region. Therefore, the rotational deformation of this joint, ϕ , is equal to the sum of the connection rotational deformation, θ_c , and the shear deformation of the column web panel zone, γ , (Díaz, Victoria, Martí, & Querin, 2011). The bending moment is produced by multiplying the applied load, P , with the distance between the load application point and the face of the reverse channel, L_{load} (Figure 21), and it is given by Equation 1.

$$M = P \times L_{load} \quad (1)$$

The displacement values of the reference points B_1 to B_3 , C_1 and C_2 (Figure 21) are used to determine the rotational deformation of the joint as proposed by Díaz et al. (2011) and Girao Coelho and Bijlaard (2007). The relevant equations are given in Equations (2 to 5):

$$\gamma = \text{atan}\left(\frac{H_{c_2} - H_{c_1}}{D}\right) - \frac{5}{64} \frac{M(H_{col} - D_{col})}{EI_c} \quad (2)$$

$$\begin{aligned} \theta_c &= \text{atan}\left(\frac{V_{B_2} - V_{B_1} - \delta_{b.el}(x_{B_2})}{x_{B_2}}\right) - \text{atan}\left(\frac{H_{c_2} - H_{c_1}}{D}\right) \\ &= \text{atan}\left(\frac{V_{B_3} - V_{B_1} - \delta_{b.el}(x_{B_3})}{x_{B_3}}\right) - \text{atan}\left(\frac{H_{c_2} - H_{c_1}}{D}\right) \end{aligned} \quad (3)$$

$$\begin{aligned} \phi &= \theta_c + \gamma = \text{atan}\left(\frac{V_{B_2} - V_{B_1} - \delta_{b.el}(x_{B_2})}{x_{B_2}}\right) - \frac{5}{64} \frac{M(H_{col} - D_{col})}{EI_c} \\ &= \text{atan}\left(\frac{V_{B_3} - V_{B_1} - \delta_{b.el}(x_{B_3})}{x_{B_3}}\right) - \frac{5}{64} \frac{M(H_{col} - D_{col})}{EI_c} \end{aligned} \quad (4)$$

V_{B_1}, V_{B_2} and V_{B_3} are the vertical displacements at reference points B_1, B_2 and B_3 , respectively. H_{c_1} and H_{c_2} are the horizontal displacements corresponding to reference points C_1 and C_2 . x_{B_2} and x_{B_3} are the distances measured from point B_1 to points B_2 and B_3 , respectively. D and D_{col} are the depths of beam and column, respectively. H_{col} and I_c correspond to the length and the second moment of area of the column. Girao Coelho and Bijlaard (2007) approach is used to evaluate the elastic deflection of beam, $\delta_{b.el(x_{B_i})}$ (Equation 5).

$$\delta_{b.el(x_{B_i})} = -\frac{P}{E_b I_b} \left(\frac{(x_{B_i})^3}{6} - \frac{L_{load}(x_{B_i})^2}{2} \right) \quad (5)$$

4.3 Finite Element Results and Observations

The main parameters and failure modes obtained from finite element models are summarized in Table 5. These parameters are given in terms of resistance, stiffness and rotation, as defined in section 3.3.3. The initial stiffness, $S_{j,in,FE}$, and the post yield stiffness, $S_{j,p,FE}$, values are computed by means of regression analysis of the elasto-plastic branches before and after the knee range (Figure 16). Moreover, the graphs in Figure 23 give the moment-rotation comparison for the same joint configuration from five different groups, as detailed in section 4.2. The general response of the joints before and after the failure can be seen in Figure 24.

Table 5: Main parameters of the moment-rotation curves and the observed failure modes

Group	Specimen	Resistance (kN.m)			Stiffness (kN.m/rad)			Rotation (rad)			Failure mode
		$M_{j,R,FE}$	$M_{j,RD,FE}$	$M_{j,ult,FE}$	$S_{j,in,FE}$	$S_{j,FE}$	$S_{j,P,FE}$	$\phi_{j,R,FE}$	$\phi_{j,x,FE}$	$\phi_{j,ult,FE}$	
G1	S1	38.8	56.6	86.2	10351.8	3450.6	1318.6	0.0037	0.0059	0.0649	BPO
	S2	39.1	57.6	88.3	12170.0	4056.7	1637.4	0.0032	0.0051	0.0548	BPO
	S3	39.8	58.1	92.1	13208.9	4403.0	1785.4	0.0030	0.0048	0.0548	BPO
	S4	40.8	60.7	93.5	13663.3	4554.4	1857.3	0.0030	0.0049	0.0511	BPO
	S5	39.4	60.2	94.9	14086.5	4695.5	2058.0	0.0028	0.0044	0.0511	BPO
	S6	39.4	59.7	96.6	14517.1	4839.0	2138.7	0.0027	0.0043	0.0472	BPO
G2	S7	20.8	33.6	60.4	4158.1	1386.0	644.8	0.0050	0.0075	0.1071	BPO
	S8	34.6	43.6	78.6	6010.5	2003.5	574.2	0.0058	0.0106	0.1304	BPO
	S9	53.3	55.7	98.3	8417.4	2805.8	462.8	0.0063	0.0159	0.1382	BPO
	S10	70.8	73.4	113.8	11180.1	3726.7	487.9	0.0063	0.0165	0.1175	EPO
	S11	74.6	73.4	120.9	14203.8	4734.6	914.5	0.0053	0.0112	0.0813	EPO
G3	S12	63.4	100.8	208.6	23313.4	7771.1	3605.0	0.0027	0.0038	0.0639	BPO
	S13	58.9	89.9	209.3	21357.5	7119.2	3097.8	0.0028	0.0037	0.0703	BPO
	S14	59.3	91.3	207.5	20505.6	6835.2	2973.2	0.0029	0.0040	0.0665	BPO
	S15	59.8	88.2	208.7	20176.3	6725.4	2891.9	0.0030	0.0064	0.0728	BPO
	S16	59.6	92.5	205.2	19152.1	6384.0	2798.4	0.0031	0.0043	0.0674	BPO
	S17	59.5	88.9	205.0	18915.9	6305.3	2747.7	0.0031	0.0043	0.0693	BPO
	S18	59.2	91.3	204.5	18421.8	6140.6	2725.3	0.0032	0.0044	0.0759	BPO
G4	S19	39.1	57.6	88.8	11958.3	3986.1	1658.8	0.0033	0.0052	0.0549	BPO
	S20	39.1	62.7	88.4	10499.1	3499.7	1630.3	0.0037	0.0056	0.0504	BPO
	S21	39.2	68.8	88.2	7408.2	2469.4	1376.9	0.0053	0.0074	0.0605	BPO
	S22	38.6	73.4	87.8	3700.9	1233.6	851.3	0.0104	0.0141	0.0827	EPO
	S23	54.6	59.5	100.0	7892.3	2630.8	449.2	0.0069	0.0169	0.1384	EPO
	S24	45.3	66.7	94.6	2875.9	958.6	405.2	0.0158	0.0244	0.1690	EPO
G5	S25	48.8	72.1	128.7	19408.1	6469.4	2791.7	0.0025	0.0038	0.0415	BPO
	S26	55.3	84.1	146.8	20614.4	6871.5	3095.9	0.0027	0.0044	0.0505	BPO
	S27	63.3	94.4	163.8	23496.1	7832.0	3285.2	0.0027	0.0042	0.0548	BPO
	S28	91.0	110.4	150.8	23580.6	7860.2	1873.3	0.0039	0.0072	0.0531	BF
	S29	94.8	122.8	152.0	26989.0	8996.3	2690.1	0.0035	0.0056	0.0332	BF
	S30	107.6	140.2	152.1	30261.5	10087.2	3167.9	0.0036	0.0056	0.0301	BF

Note: BPO denotes Bolt Pull-Out, EPO denotes End plate Pulled Outwards, BF denotes Bolt Failure

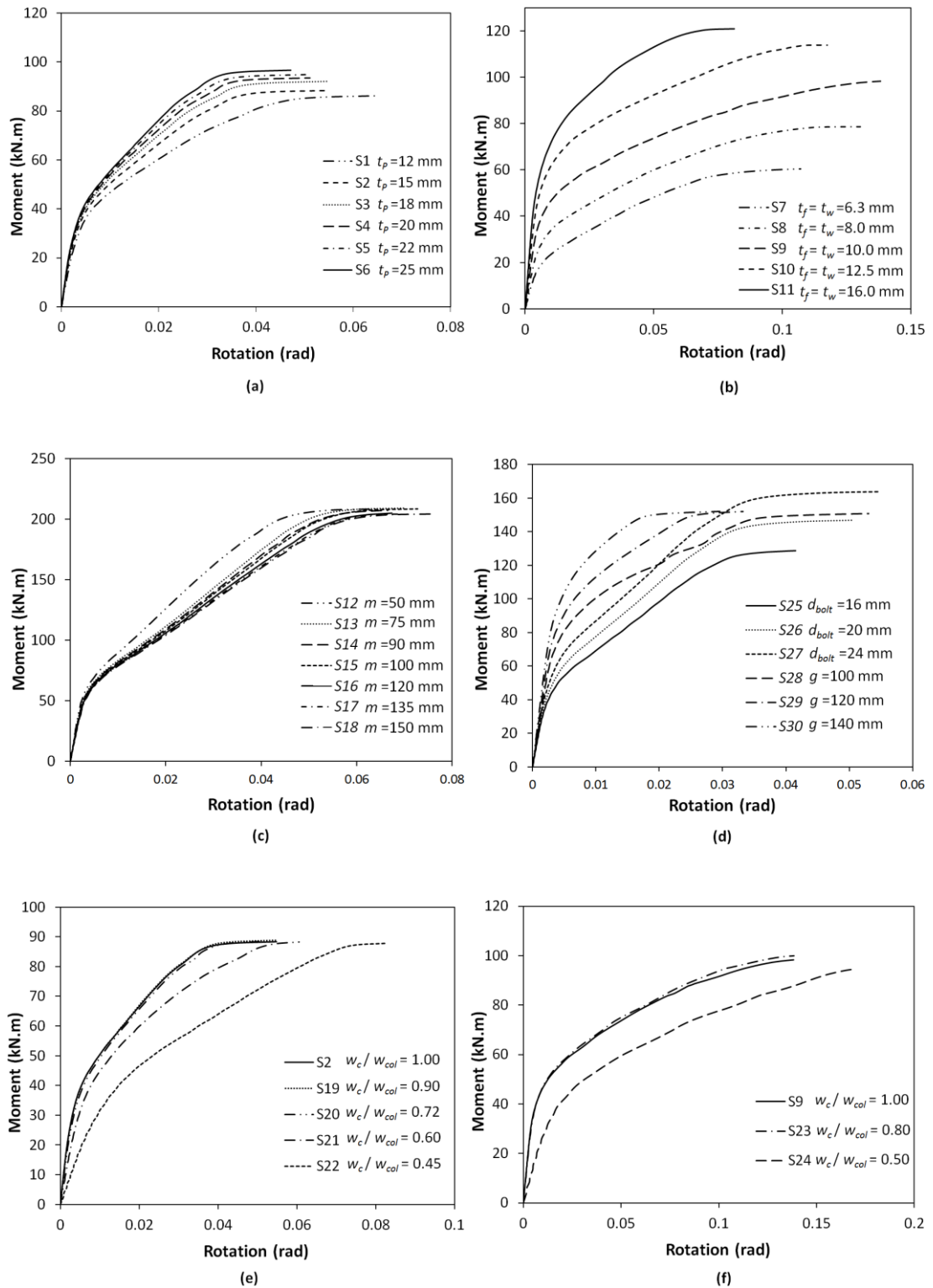
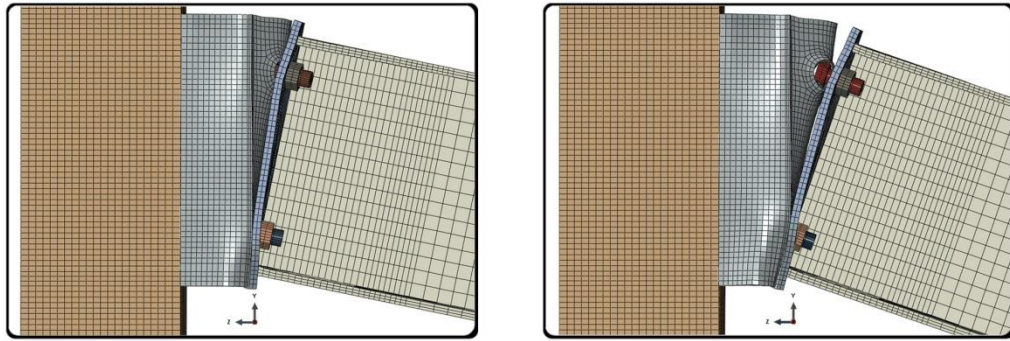


Figure 23: Moment-rotation curves for: (a) G1, (b) G2, (c) G3, (d) G5, (e) First series of G4 and (f) Second series of G4



(a)

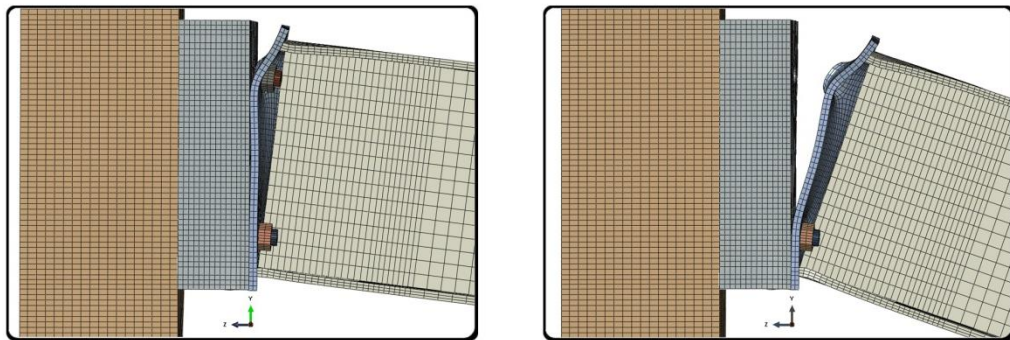
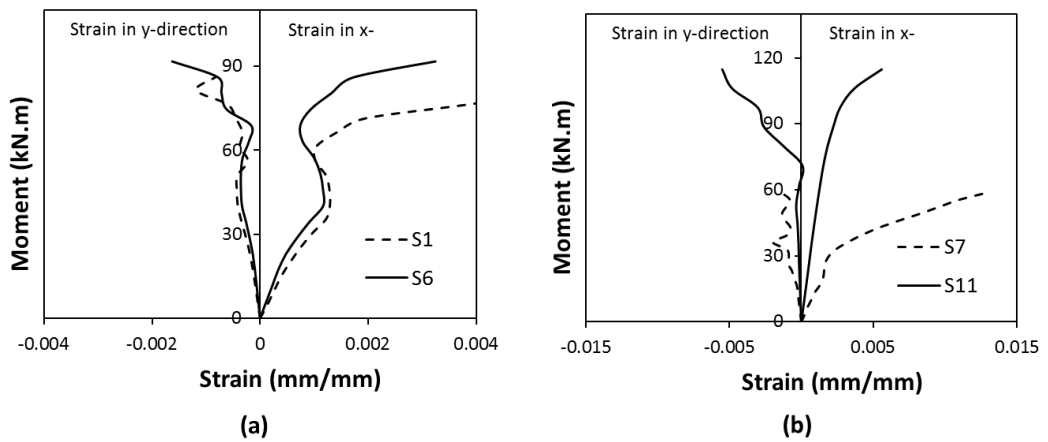


Figure 24: Joint general response before and after failure: (a) Bolt's head pull-out from reverse channel (BPO) of S7 and (b) End-plate pulled outwards (EPO) of S11

The deformability of the reverse channel is quantified in terms of the strain measurements, between tension bolts, in x and y-directions, as illustrated in Figure 25.



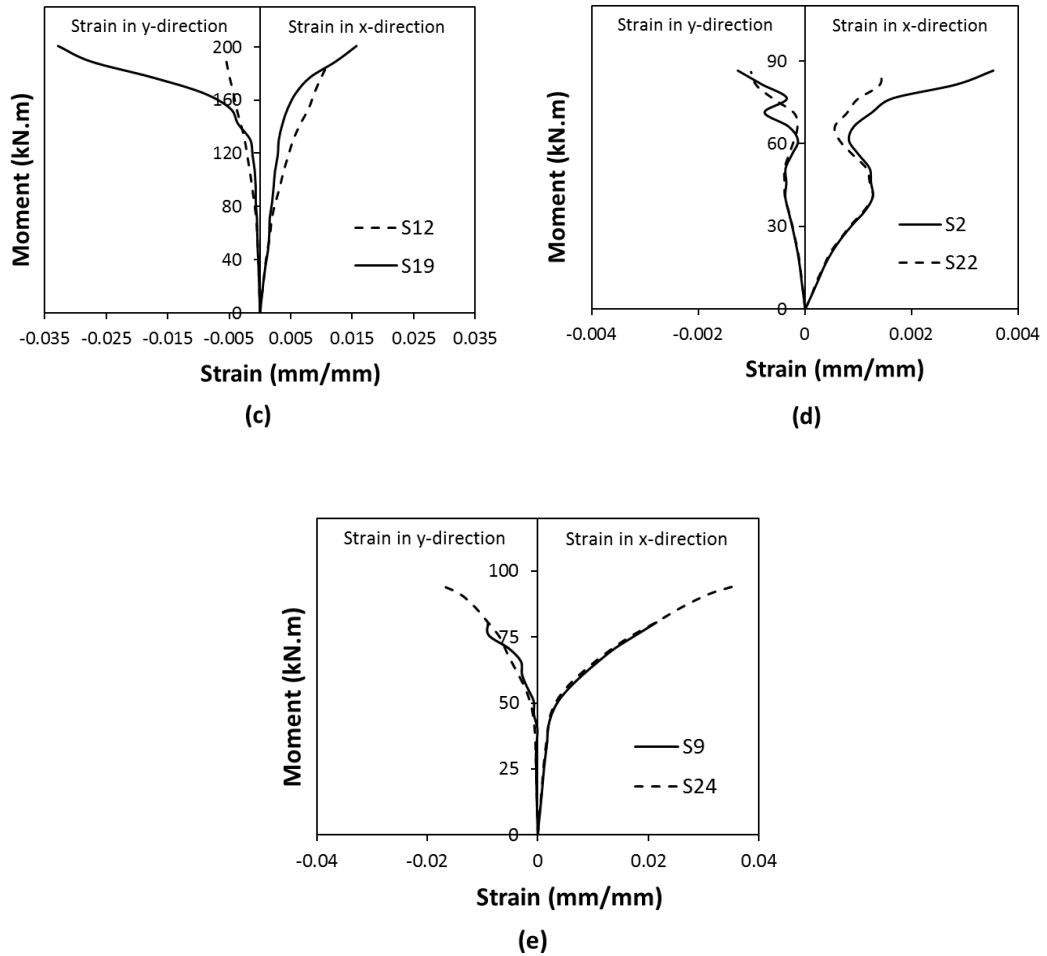


Figure 25: Strain measurements, between tension bolts, in x and y-directions; extreme specimens in each group

In this section, the parametric study results will be presented by considering the effect of the geometric parameters mentioned in section 4.2: the flush end-plate thickness, the wall thickness of channel, the width of channel, the ratio of channel depth to SHS width and the nominal bolt diameter and the gage distance.

4.3.1 Effect of Flush End-Plate Thickness (G1)

The moment-rotation ($M-\phi$) curves for the first group G1 are compared in Figure 23 (a). For the thick flush end-plate, generally the results indicate that, the higher the moment resistance, the higher the initial stiffness is and the lower the rotational capacity of the connection will be. When the flush end-plate's thickness increased from 12 mm (S1) to 25 mm (S6), more load needs to be applied to develop high

moment resistance, which results in notable increased in the ultimate flexural resistance and the initial stiffness values of the connection, up to 12% and 40%, respectively. Furthermore, the reverse channel became the weak part, with respect to the flush end-plate and the bolts, which caused a reduction in the rotational capacity of the connection by up to 27% (Table 5).

The failure modes of this group were identical, irrespective of the variation in flush end-plate thickness. One example from the failed connections is shown in Figure 24 (a), where the web of the reverse channel was pulled outwards by the bolts at the top. In all cases, the webs of the hot-rolled channel sections are significantly thinner than the flush end-plates, which resulted in the reverse channels controlling the failure and having experienced large deformations. On the other hand, there was no sign of deformation in the face of the SHS columns or in the steel beams.

4.3.2 Effect of the Wall Thickness of Reverse Channel (G2)

The effect of wall thickness of reverse channel on the moment-rotation ($M-\phi$) response for group G2 is illustrated in Figure 23(b). In the simulations of G2, the reverse channels were cut from hot-rolled SHS tubes in order to get varied wall thicknesses. According to the results in Table 5, increasing the wall thickness of reverse channel gave remarkable increase in both the initial stiffness and ultimate flexural resistance values of RCC. When the wall thickness of reverse channel increased from 6.3 mm (S7) to 16 mm (S11), there were 2.0 and 3.4 times increase in ultimate flexural resistance and the initial stiffness values of the RCC, respectively. On the other hand, the increase in the wall thickness of the reverse channel has led to discrepancies in the rotational capacity values. This may be explained by the change in the ratio of wall thickness of reverse channel to the thickness of flush end-plate

(Figure 23(b)). The maximum rotational capacity was achieved when the ratio was equal to one. When this ratio is less than or equal to one, this might have caused the bolt heads to punch through bolt holes of reverse channel (Figure 24(a)). On the contrary, the deformation of the flush end-plate became more severe once this ratio was more than one. This might have caused the failure mode shown in Figure 24 (b), where the flush end-plate was pulled out from the tension bolts (EPO).

4.3.3 Effect of the Width of Reverse Channel (G3)

The influence of the width of channel on RCC response is given in Figure 23(c). It compares the moment-rotation ($M-\phi$) response for reverse channel cut from hot-rolled SHS tube with seven different widths: 50, 75, 90, 100, 125, 130 and 150 mm. The ductility contributed by RCC lead to noticeable variations in the rotational capacity without compromise to ultimate flexural resistance. The web and flanges of the tube-cut channels exhibit more deformations with the increase in channel width. In addition, by increasing the width of reverse channel twice and thrice, exhibits 13.9% and 18.8% higher rotational capacity, respectively. This can be seen when the results of specimens S15 and S18 are compared with those of S12 in Table 5. In all cases, the failure modes of the tests were the bolt pull-out (BPO) from reverse channel (Figure 24(a)).

4.3.4 Effect of the Ratio of Reverse Channel Depth to SHS Width (G4)

Figure 23(e) and (f) elucidates the effect of the ratio of channel depth to SHS width on the moment-rotation ($M-\phi$) response of RCC. Two different RCC configurations with six different ratios were investigated: 0.90, 0.80, 0.72, 0.60, 0.50 and 0.45. The results indicate that the deformation of the face of SHS columns is proportional to the ratio of channel depth to SHS width. When the SHS width was wider than the reverse channel depth, the face of SHS column was pulled outwards at the top while

at the bottom it was pushed inwards due to the bending deformation of the web of reverse channel. As this ratio decreased to less than 0.72, the initial stiffness value reduced without sacrificing the ultimate strength and the deformations of the face of SHS columns became noticeable. On the other hand, there was an increase in the rotational capacity. As a result, the ratio of 0.72 can be considered as threshold ratio and it is suggested to keep this ratio more than or equal to 0.72 in order to prevent the column face deformation.

4.3.5 Effect of the Nominal Bolt Diameter and the Gage Distance (G5)

The effect of the nominal bolt diameter and gage distance on the moment-rotation ($M-\phi$) response for group G5 is illustrated in Figure 23(d). According to the results in Table 5, increasing the nominal bolt diameter gave remarkable increase in all characteristics of moment-rotation ($M-\phi$) values of RCC. When the nominal bolt diameter increased from 16 mm (S25) to 24 mm (S27), there was a notable increase in the ultimate flexural resistance, the initial stiffness and rotational capacity values of the connection, up to 27%, 21% and 32%, respectively. On the other hand, generally the results indicate that increase in the gage distance causes increase in the initial stiffness and decrease in the rotational capacity of the connection. Furthermore, it was noted that the failure modes of the tests (S28-S30) were bolt failure (BF) which shows that the bolts became the weak part with respect to the flush end-plate and the reverse channel.

4.3.6 Sensitivity Chart

To sum up the effect of the geometrical configurations of reverse channel flush end-plate connections on the moment-rotation ($M-\phi$) relationship, a sensitivity chart was developed as shown in Figure 26. In this figure, the correlation coefficients with the characteristics of $M-\phi$ are illustrated as horizontal bars with percentile values. The

positive value implies that there is proportional relationship while the negative means inverse relationship. It should be noted that the flush end-plate thickness and the nominal bolt diameter have the greatest effect on the ultimate flexural resistance. On the other hand, the rotational capacity is strongly sensitive against the gage distance, the nominal bolt diameter and the flush end-plate thickness.

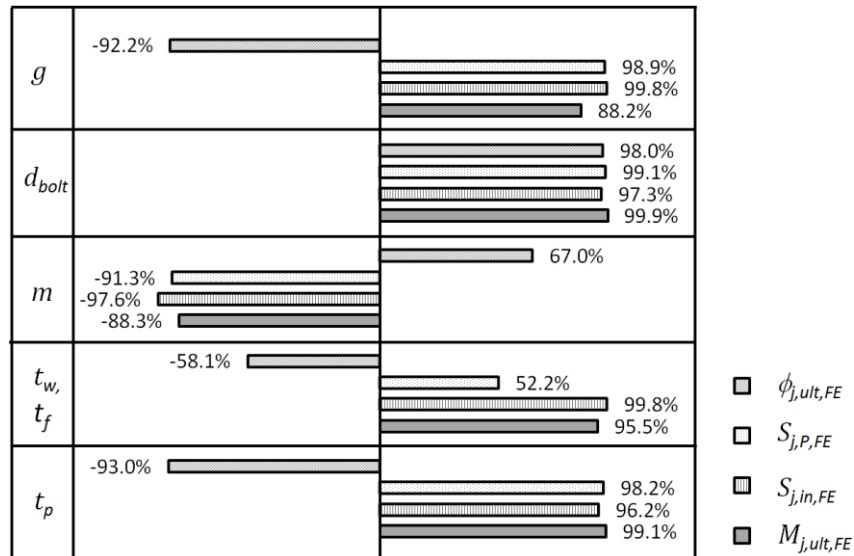


Figure 26: The sensitivity chart on the characteristics of moment-rotation of RCC

Chapter 5

EFFECT OF MATERIALS STRENGTH ON $M-\phi$ CHARACTERISTICS OF RCC

5.1 Introduction

During the last two decades there has been increase in the usage of High Strength Steels (HSS). This was partly due to the increase in the demand for constructing tall structures and also the problems encountered with the steel beam-to-column connections during Northridge and Kobe earthquakes (Wilkinson, Hurdman, & Crowther, 2006), (Scawthorn & Yanev, 1995). This increased demand for HSS encouraged researchers to embark on research into moment connections employing HSS columns (Gao, Sun, Jin, & Fan, 2009), (Coelho, Bijlaard, & Kolstein, 2009), (Ban, Shi, Shi, & Bradford, 2013), (Shi, Ban, & Bijlaard, 2012), (Ban, Shi, Shi, & Wang, 2012), (Wang, Li, Su-Wen, & Fei-Fei, 2014) beams (Ban & Bradford, 2013), end plates (Coelho, Bijlaard, & Silva, 2004), (Qiang, Bijlaard, Kolstein, & Jiang, 2014a), (Qiang, Bijlaard, Kolstein, & Jiang, 2014), (Coelho & Bijlaard, 2007) and bolts (Coelho & Bijlaard, 2007).

The parametric study mentioned in the previous chapter were illustrated the effect of the geometrical configurations of RCC on the moment-rotation ($M-\phi$) relationship and the results indicate that the main source of deformability of RCC is the reverse channel. Therefore, there is need to do more investigation with the objective of understanding the behaviour of RCC connections particularly with HSS reverse channels. On the other hand, reverse channel was introduced mainly to provide a

medium for connecting beams to hollow sections with traditional bolts. However, even this approach may provide limited access for tightening bolts, particularly when deep beams are connected to reverse channel. This brought up the idea of splitting the reverse channel into two pieces by leaving a gap in between which will allow for better access for bolt tightening. From now on this split reverse channel connection will be named as Double Reverse Channel Connection (DRCC) (Figure 27).

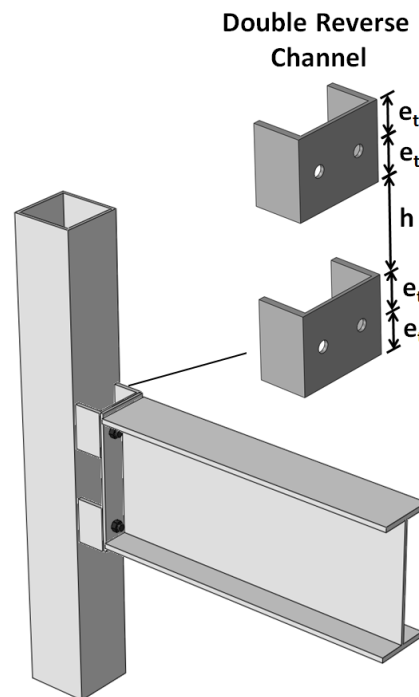


Figure 27: Double reverse channel connection (DRCC)

The effects of the material properties of reverse channel flush end-plate connections on the moment-rotation ($M-\phi$) relationship under monotonic loading are introduced in this chapter. Moreover, the behaviour of newly introduced DRCC will also investigate; the effects of material properties and the variation of clear distance between the split reverse channels; and then the results will compare with those of RCC. For this purpose, thirty five reverse channel joints with five different connection configurations; varying dimensions of column sizes, beam sections and channel types were investigated. Subsequent sections of this chapter describe the

specimens considered in parametric study. The main results of this parametric study are then presented and the observations related to the response are discussed.

5.2 Parametric Study

Based on the previous procedure of FEM mentioned in chapter 3, a new 3D finite element model was developed by using ABAQUS (v.6.12) to investigate the effects of reverse channel material property on the behaviour and strength of RCCs as well as to validate the behaviour of newly introduced DRCC, which give more access to inside of the reverse channel to tighten conventional bolts, particularly with deep beam connection. Table 6 summarizes the dimensions of seventeen reverse-channel joints and fourteen double-reverse-channel joints which were considered in this study. All tests are divided into four groups (2-G1 to 2-G4). The first group of connections (2-G1) is formed by selecting different specimens from previous parametric study carried out in chapter 4. Five beam sections UB 305×165×40, UB 356×127×33, UB 406×178×60, UB 457×191×106 and UB 533×210×92 , five column sections and reverse channels of two different sizes and four cut from different hot-rolled SHS tubes were used. The steel grade for beams, columns, flush end-plates and channel sections was S355 and Grade 8.8 standard M20 bolts were used. The group 2 (2-G2) is formed to investigate the influence of reverse-channel material property on the behaviour and strength of RCC; the steel grade used for beams, columns, and flush end-plates was S355 and for reverse-channel it was S690. The remaining groups (2-G3 and 2-G4) were allocated to compare the behaviour of DRCC with RCC; in group 3 (2-G3), the steel grade used for all joints components was S355 and the clear distance between double reverse channels, h , was calculated by $h = h_c - 4e_t$ (Figure 27). The steel grade of S355 was used for beams, columns and flush end-plates and S690 were used for reverse-channel to examine the influence of

material property of reverse channel on the behaviour and strength of DRCC in group 4 (2-G4).

5.3 FE results and Discussions

The main parameters and failure modes obtained from finite element models are summarized in Table 7. These parameters are given in terms of resistance, stiffness and rotation, as defined in section 3.3.3. The initial stiffness, $S_{j,in,FE}$, and the post yield stiffness, $S_{j,p,FE}$, values are computed by means of regression analysis of the elasto-plastic branches before and after the knee range (Figure 16). Moreover, the graphs in Figure 28 give the moment-rotation comparison between RCC and DRCC for the same joint configuration extracted from four different groups, as detailed in section 5.2 and Table 7. The deformability of the reverse channel is quantified in terms of the strain measurements, between tension bolts, in x and y-directions; an example is illustrated in Figure 29. The general response of the joints before the failure can be seen in Figures 30 and 31.

In this section, the parametric study results will be presented by considering: the effect of the material properties of reverse channel on the moment-rotation ($M-\phi$) relationship of RCC and DRCC under monotonic loading; comparison between the behaviour of RCC and DRCC for the same connection; and the effect of the variation of clear distance between the split reverse channels on the behaviour of DRCC.

Table 6: Schedule of test specimens in the parametric study

Group	Specimen	Column Section (S355)	Beam Section (S355)	Channel								Endplate (S355)				
				Section	Steel Grade	h*	h _c	w _c	m	t _{fc}	t _{wc}	h _p	w _p	t _p	e _t	g
2-G1	S1	SHS180 × 10	UKB356 × 127 × 33	UKPFC180 × 90 × 26	S355	-	400	180	90	12.5	6.5	400	180	12	72	90
	S2	SHS180 × 10	UKB356 × 127 × 33	UKPFC180 × 90 × 26	S355	-	400	180	90	12.5	6.5	400	180	15	72	90
	S6	SHS180 × 10	UKB356 × 127 × 33	UKPFC180 × 90 × 26	S355	-	400	180	90	12.5	6.5	400	180	25	72	90
	S11	SHS200 × 10	UKB305 × 165 × 40	cut from SHS200 × 16	S355	-	339.4	200	90	16	16	339	200	18	67	100
	S12	SHS260 × 10	UKB533 × 210 × 92	cut from SHS260 × 10	S355	-	583.1	260	50	10	10	583.1	259.3	25	75	100
	S15	SHS260 × 10	UKB533 × 210 × 92	cut from SHS260 × 10	S355	-	583.1	260	100	10	10	583.1	259.3	25	75	100
	S18	SHS260 × 10	UKB533 × 210 × 92	cut from SHS260 × 10	S355	-	583.1	260	150	10	10	583.1	259.3	25	75	100
	S21	SHS300 × 10	UKB356 × 127 × 33	UKPFC180 × 90 × 26	S355	-	400	180	90	12.5	6.5	400	180	15	72	90
	S31	SHS250 × 10	UKB457 × 191 × 106	cut from SHS250 × 10	S355	-	513.2	250	90	10	10	513.2	238	22	82	80
S32	SHS250 × 10	UKB406 × 178 × 60	UKPFC230 × 75 × 26	S355	-	446.2	230	75	12.5	6.5	446.2	217.9	20	65	100	
2-G2	HSS-S1	SHS180 × 10	UKB356 × 127 × 33	UKPFC180 × 90 × 26	S690	-	400	180	90	12.5	6.5	400	180	12	72	90
	HSS-S2	SHS180 × 10	UKB356 × 127 × 33	UKPFC180 × 90 × 26	S690	-	400	180	90	12.5	6.5	400	180	15	72	90
	HSS-S6	SHS180 × 10	UKB356 × 127 × 33	UKPFC180 × 90 × 26	S690	-	400	180	90	12.5	6.5	400	180	25	72	90
	HSS-S11	SHS200 × 10	UKB305 × 165 × 40	cut from SHS200 × 16	S690	-	339.4	200	90	16	16	339	200	18	67	100
	HSS-S12	SHS260 × 10	UKB533 × 210 × 92	cut from SHS260 × 10	S690	-	583.1	260	50	10	10	583.1	259.3	25	75	100
	HSS-S18	SHS260 × 10	UKB533 × 210 × 92	cut from SHS260 × 10	S690	-	583.1	260	150	10	10	583.1	259.3	25	75	100
	HSS-S21	SHS300 × 10	UKB356 × 127 × 33	UKPFC180 × 90 × 26	S690	-	400	180	90	12.5	6.5	400	180	15	72	90
2-G3	DR-S1	SHS180 × 10	UKB356 × 127 × 33	UKPFC180 × 90 × 26	S355	112	400	180	90	12.5	6.5	400	180	12	72	90
	DR-S2	SHS180 × 10	UKB356 × 127 × 33	UKPFC180 × 90 × 26	S355	112	400	180	90	12.5	6.5	400	180	15	72	90
	DR-S6	SHS180 × 10	UKB356 × 127 × 33	UKPFC180 × 90 × 26	S355	112	400	180	90	12.5	6.5	400	180	25	72	90
	DR-S11	SHS200 × 10	UKB305 × 165 × 40	cut from SHS200 × 16	S355	71.4	339.4	200	90	16	16	339	200	18	67	100
	DR-S12	SHS260 × 10	UKB533 × 210 × 92	cut from SHS260 × 10	S355	283.1	583.1	260	50	10	10	583.1	259.3	25	75	100
	DR-S18	SHS260 × 10	UKB533 × 210 × 92	cut from SHS260 × 10	S355	283.1	583.1	260	150	10	10	583.1	259.3	25	75	100
	DR-S21	SHS300 × 10	UKB356 × 127 × 33	UKPFC180 × 90 × 26	S355	112	400	180	90	12.5	6.5	400	180	15	72	90
2-G4	DRHSS-S1	SHS180 × 10	UKB356 × 127 × 33	UKPFC180 × 90 × 26	S690	112	400	180	90	12.5	6.5	400	180	12	72	90
	DRHSS-S2	SHS180 × 10	UKB356 × 127 × 33	UKPFC180 × 90 × 26	S690	112	400	180	90	12.5	6.5	400	180	15	72	90
	DRHSS-S6	SHS180 × 10	UKB356 × 127 × 33	UKPFC180 × 90 × 26	S690	112	400	180	90	12.5	6.5	400	180	25	72	90
	DRHSS-S11	SHS200 × 10	UKB305 × 165 × 40	cut from SHS200 × 16	S690	71.4	339.4	200	90	16	16	339	200	18	67	100
	DRHSS-S12	SHS260 × 10	UKB533 × 210 × 92	cut from SHS260 × 10	S690	283.1	583.1	260	50	10	10	583.1	259.3	25	75	100
	DRHSS-S18	SHS260 × 10	UKB533 × 210 × 92	cut from SHS260 × 10	S690	283.1	583.1	260	150	10	10	583.1	259.3	25	75	100
	DRHSS-S21	SHS300 × 10	UKB356 × 127 × 33	UKPFC180 × 90 × 26	S690	112	400	180	90	12.5	6.5	400	180	15	72	90

Note: All specimens in Group 2-G1, except S31 and S32, were selected from the previous parametric study carried out in chapter 4

* h is the clear distance between the split reverse channels in DRCC

Table 7: Main parameters of the moment-rotation curves and the observed failure modes

Group	Specimen	Resistance (kN.m)			Stiffness (kN.m/rad)			Rotation (rad)			Failure mod
		$M_{j,R,FE}$	$M_{j,Rd,FE}$	$M_{j,ult,FE}$	$S_{j,m,FE}$	$S_{j,FE}$	$S_{j,p,FE}$	$\phi_{j,R,FE}$	$\phi_{j,x,FE}$	$\phi_{j,ult,FE}$	
2-G1	S1	38.8	56.6	86.2	10351.8	3450.6	1318.6	0.0037	0.0059	0.0649	BPO
	S2	39.1	57.6	88.3	12170.0	4056.7	1637.4	0.0032	0.0051	0.0548	BPO
	S6	39.4	59.7	96.6	14517.1	4839.0	2138.7	0.0027	0.0043	0.0472	BPO
	S11	74.6	73.4	120.9	14203.8	4734.6	914.5	0.0053	0.0112	0.0813	EPO
	S12	63.4	100.8	208.6	23313.4	7771.1	3605.0	0.0027	0.0038	0.0639	BPO
	S15	59.8	88.2	208.7	20176.3	6725.4	2891.9	0.0030	0.0064	0.0728	BPO
	S18	59.2	91.3	204.5	18421.8	6140.6	2725.3	0.0032	0.0044	0.0759	BPO
	S21	39.2	68.8	88.2	7408.2	2469.4	1376.9	0.0053	0.0074	0.0605	BPO
	S31	52.8	80.4	173.9	14494.9	4831.6	2081.5	0.0036	0.0052	0.0838	BPO
S32	23.8	53.8	96.0	9266.3	3088.8	2058.7	0.0026	0.0030	0.0557	BPO	
2-G2	HSS-S1	67.9	91.7	133.9	9996.7	3332.2	1107.2	0.0068	0.0114	0.0914	BPO+DE
	HSS-S2	68.3	102.2	133.9	11211.8	3737.3	1548.3	0.0061	0.0095	0.0661	BPO+DE
	HSS-S6	71.9	122.1	145.3	12968.0	4322.7	2201.7	0.0055	0.0079	0.0632	BPO
	HSS-S11	73.5	89.1	123.6	13173.0	4391.0	1154.4	0.0056	0.0108	0.0686	EPO
	HSS-S12	121.3	253.2	263.8	23388.0	7796.0	4917.1	0.0052	0.0064	0.0432	BF+DC
	HSS-S18	116.0	230.6	257.5	18226.4	6075.5	3636.0	0.0064	0.0079	0.0545	BF+DC
	HSS-S21	69.2	95.1	131.4	7247.6	2415.9	853.7	0.0095	0.0155	0.1020	BPO
2-G3	DR-S1	38.8	54.2	77.1	8711.7	2903.9	1091.9	0.0045	0.0070	0.0647	BPO
	DR-S2	39.0	54.8	80.0	10387.5	3462.5	1347.1	0.0037	0.0061	0.0527	BPO
	DR-S6	39.1	59.1	84.9	11893.0	3964.3	1771.7	0.0033	0.0051	0.0496	BPO
	DR-S11	78.1	85.7	119.3	12460.4	4153.5	708.6	0.0063	0.0144	0.0783	EPO
	DR-S12	21.1	*	201.7	10224.3	3408.1	4225.5	0.0021	0.0021	0.0572	BPO
	DR-S18	23.0	*	185.1	9067.5	3022.5	3056.2	0.0025	0.0026	0.0815	BPO
	DR-S21	39.8	65.1	77.6	6858.3	2286.1	1061.2	0.0058	0.0089	0.0623	BPO
2-G4	DRHSS-S1	67.4	86.0	119.5	9050.6	3016.9	847.0	0.0074	0.0138	0.0898	BPO
	DRHSS-S2	63.2	96.3	120.5	10395.4	3465.1	1481.8	0.0061	0.0089	0.0663	BPO
	DRHSS-S6	68.0	111.1	130.0	12159.1	4053.0	1952.9	0.0056	0.0081	0.0582	BPO
	DRHSS-S11	69.9	88.6	121.9	12632.1	4210.7	1230.7	0.0055	0.0099	0.0673	EPO
	DRHSS-S12	33.3	*	259.0	10454.4	3484.8	5902.7	0.0032	0.0021	0.0477	BF+DC
	DRHSS-S18	46.2	*	239.4	9500.1	3166.7	3886.0	0.0049	0.0052	0.0608	BF+DC
	DRHSS-S21	65.2	89.9	117.5	6851.9	2284.0	800.4	0.0095	0.0153	0.0927	BPO

Note: BPO, EPO, BF, DC and DE denote Bolt Pull-Out, End plate Pulled Outwards, Bolt Failure, Deformation in Channel and Deformation in End plate, respectively.

* $M_{j,Rd}$ cannot be found; this moment is corresponding to the secant stiffness, S_j , which is equal to one-third of the initial stiffness

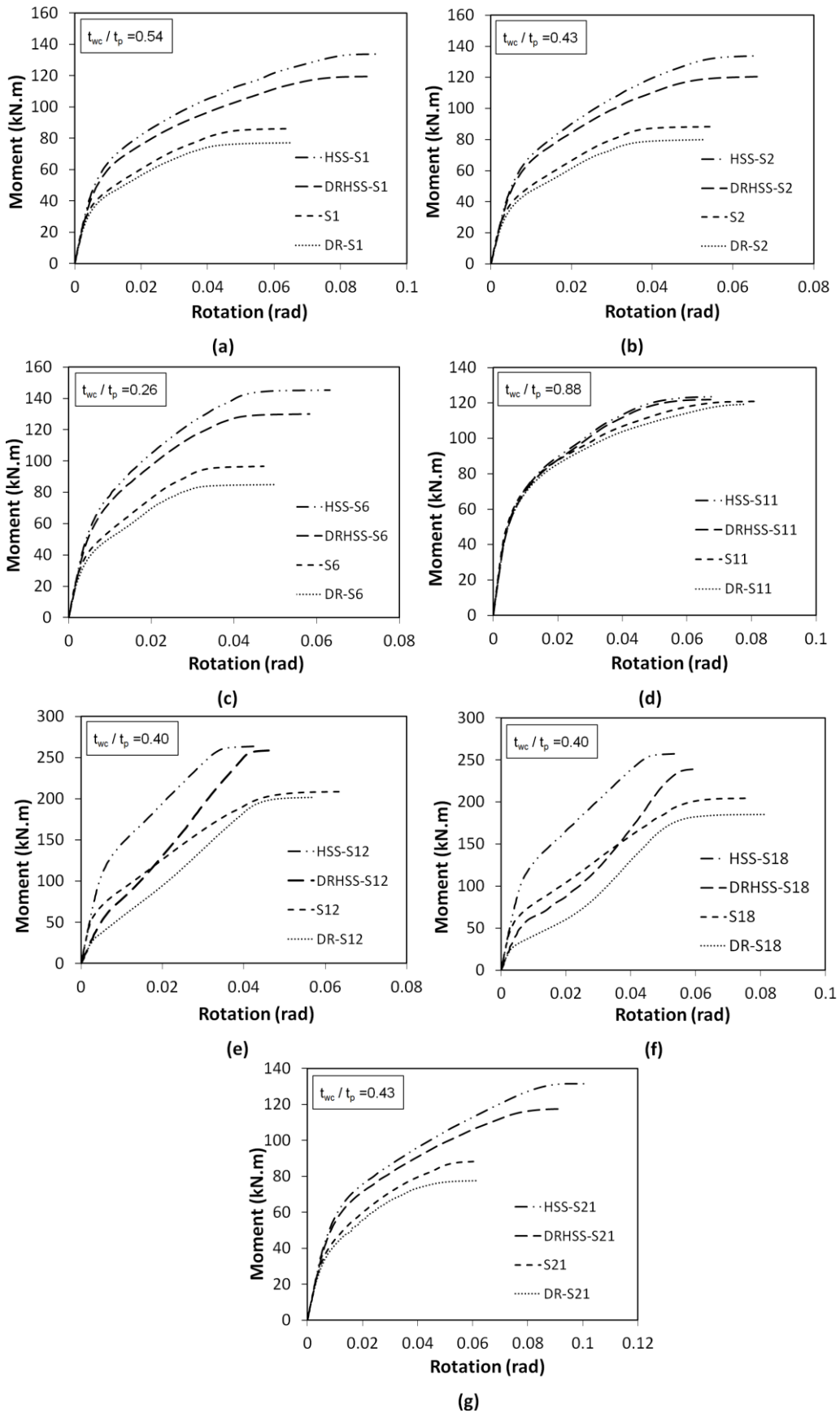


Figure 28: Comparison of moment-rotation curves from FE models between RCC and DRCC with and without HSS.

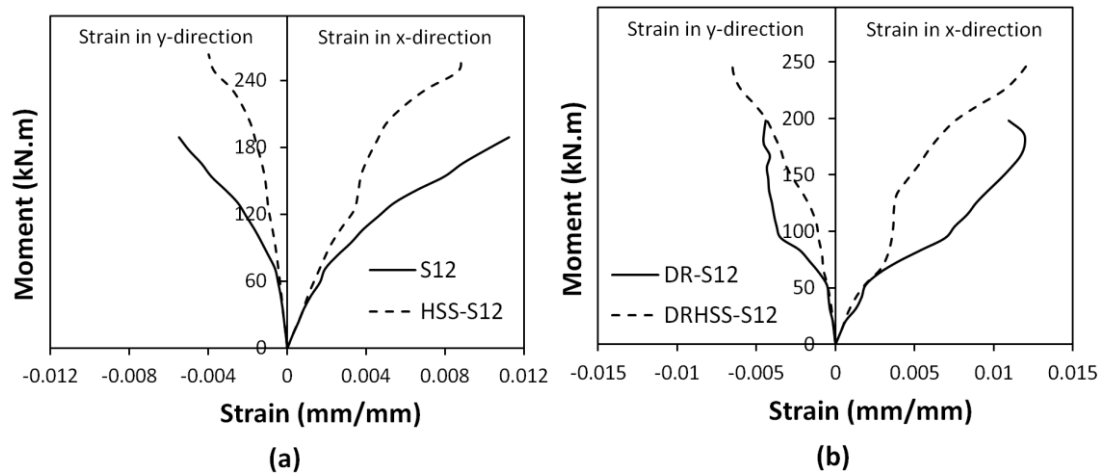


Figure 29: Strain measurements between tension bolts in x and y directions; (a) S12 and HSS-S12 and (b) DR-S12 and DRHSS-S12

5.3.1 Effect of Reverse-Channel Material Property on the Response of RCC and DRCC

The effect of the material property of reverse channel on RCC and DRCC response is given in Figure 28. This figure includes seven cases ((a) to (g)) and each case compares the moment-rotation ($M-\phi$) responses of the same connection from four different groups mentioned in section 5.2 (RCC and DRCC with mild steel and HSS channel). The steel grade of reverse channel was varied from S355 to S690. Based on comparison of Figure 28 (a) to (c) and (h), the results indicate that the use of HSS (S690) reverse channel as part of the joint; compared to mild steel (S355), produced remarkable increase in both ultimate flexural resistance and the rotational capacity without compromise to the initial stiffness. From Table 7, it was also noted that the increase in ultimate flexural resistance for RCC and DRCC was within the ranges of 48.9% to 55.3% and 50.7% to 54.9%, respectively. Nevertheless, the increase in the rotational capacity for RCC and DRCC was within the ranges of 20.6% to 68.4% and 17.4% to 48.8%, respectively. On the other hand, the failure modes of these joints were almost identical, irrespective of the variation in steel grade of reverse channel. One example from the failed connections is shown in Figure 30, where the web of

the reverse channel was pulled outwards by the bolts at the top (BPO). The webs of the hot-rolled channel sections are significantly thinner than the flush end-plates ($t_{wc}/t_p = 0.542$). In case of using mild steel reverse channel (S355), (Figure 30 (a) and (c)), the reverse channels experienced large deformations and controlled the failure of connections, due to t_{wc}/t_p ratio. On the other hand, the change of steel grade of reverse channel to HSS (S690) led channel require more load to deform, thereby making the connection stiffer and develop high moment resistance. Consequently, noticeable deformation of the flush end-plate was noted.

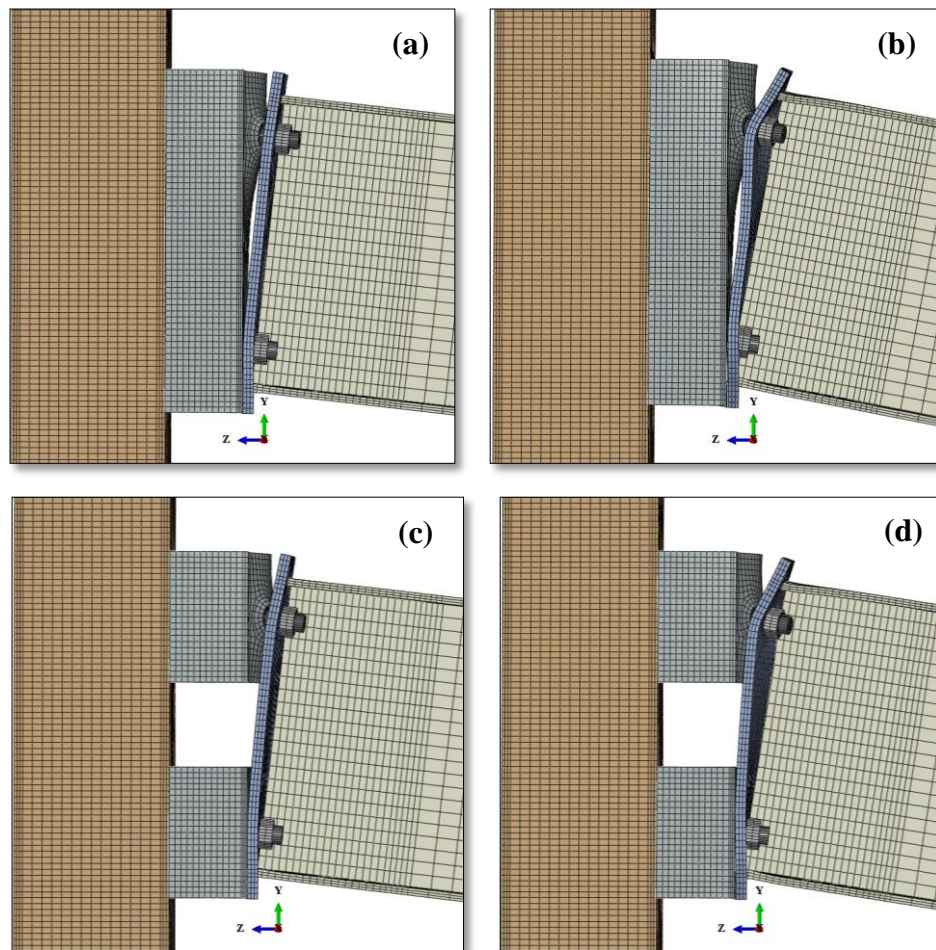


Figure 30: Joint general response prior to failure: Bolt's head pull-out from reverse channel (BPO) of (a) S1, (b) HSS-S1, (c) DR-S1 and (d) DRHSS-S1

In Figure 28 (d), the situation is quite different when HSS (S690) is used for reverse channel; the value of rotational capacity is reduced without sacrificing the initial stiffness and the ultimate strength values. By comparing the results of specimens S11 and DR-S11 with those of HSS-S11 and DRHSS-S11 in Table 7, the reductions in the rotational capacity values were up to 15.6% and 14%, respectively. Regarding the failure modes of these joints, Figure 31 shows that the deformation of the flush end-plate was more severe in all cases, which in turn caused the failure mode of EPO, where the flush end-plate was pulled out from the tension bolts. In all cases the ratio of t_{wc}/t_p was quite high (0.88) which resulted in the flush end-plates being the weak parts, with respect to the reverse channels and the bolts, and controlling the failure with large deformations. So the use of HSS reverse channel for these joints did not provide the structural behaviour envisaged.

Similarly, the introduction of S690 steel grade for reverse channel significantly increased the ultimate flexural resistance value and also reduced the rotational capacity value (Figure 28 (e) and (f)). The increase in ultimate flexural resistance for RCC and DRCC was about 26% and 29%, respectively; while the reductions in the rotational capacity values for RCC and DRCC were within ranges of 28.2% to 32.4% and 16.6% to 25.4%, respectively. It should be noted that the thickness of flush end-plate was quite high when compared to the wall thickness of reverse channel ($t_{wc}/t_p = 0.40$). The failure modes of the tests with mild reverse channels were the bolt pull-out (BPO) from reverse channel while the tests with HSS reverse channels were bolt failure with significant deformation in reverse channel. Herein the beam depth may have a direct influence on the rotational capacity values for RCC and DRCC. Past research carried out on Northridge steel beam to column connections indicated that shallow beam connections often show a high plastic rotational capacity than deep

beam connections. For example, the tested specimens of SAC3, SAC5 and SAC7 in Phase 1 of SAC Steel Projects (SAC, 1996) and the parametric study carried out on modified post-Northridge connections (Hedayat & Celikag, 2009) also shown that the beam depth may have significant effect on connection rotational capacity.

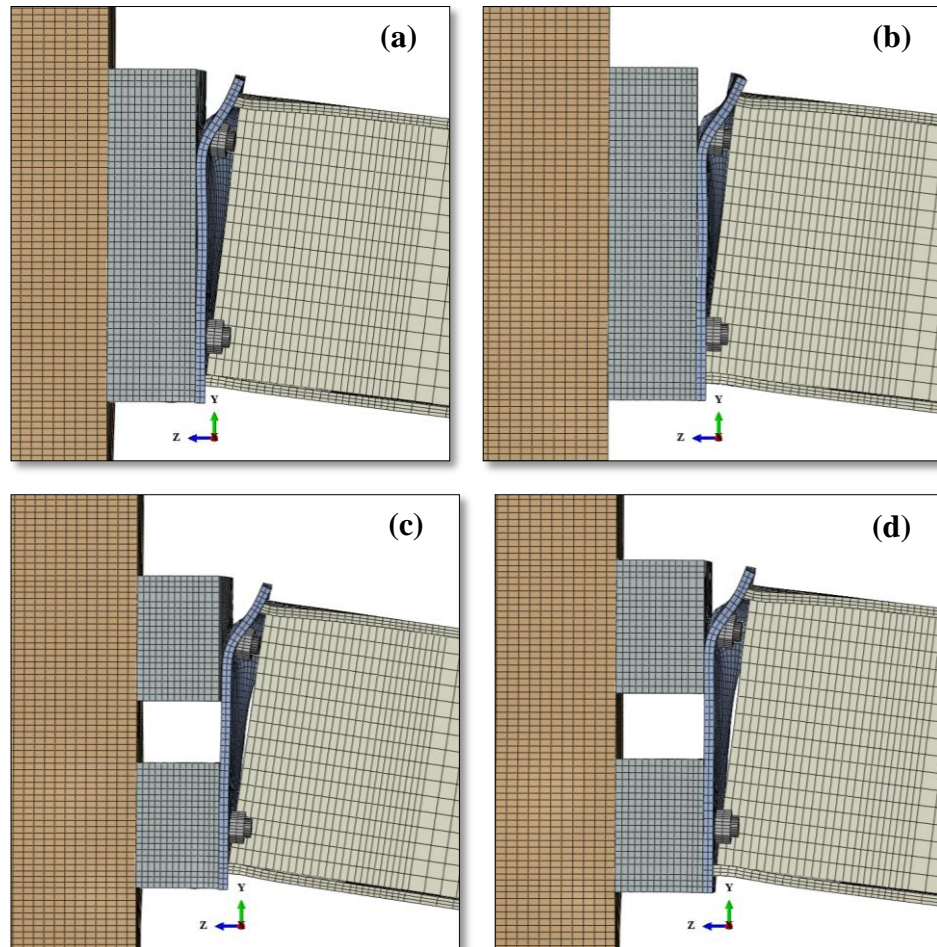


Figure 31: Joint general response prior to failure: End-plate pulled outwards (EPO) of (a) S11, (b) HSS-S11, (c) DR-S11 and (d) DRHSS-S11

5.3.2 Comparison between the Behaviour of RCC and DRCC

When the moment-rotation ($M-\phi$) curves of RCC and DRCC are compared, it can be seen in Figure 28 that in all cases, except (e) and (f), using DRCC produced less ultimate flexural resistance than the RCC. Moreover, the initial stiffness and the deformation capacity for DRCC were very similar to those of RCC. In contrast,

Figure 28 (e) and (f) show a sudden reduction in the initial stiffness for DRCC. This reduction may be owing to either the effect of depth of beam and/or the clear distance between the split reverse channels (h). The beam sections used for these connections were UKB 533×210×92 and the clear distance (h) was 283 mm. This is the deepest beam considered for this parametric study and the highest clear distance for DRCC. Therefore, there is need for further investigation of these parameters which may affect the behaviour of DRCC.

When moment-rotation ($M-\phi$) curves for all the cases are compared in Figure 28 it becomes clear that the main improvements in moment capacity and rotation capacity are due to the use of DRCC with HSS channel as opposed to RCC. For example, the results in Figure 28 (a) to (c) and (h) indicate that the use of DRCC with HSS (S690) reverse channel produced 33.2% to 38.7% increase in ultimate flexural resistance and 20.9% to 53.1% increase in rotational capacity, without compromise to the initial stiffness (Table 7).

5.3.3 Effect of the Variation of Clear Distance between the Split Reverse Channels on the Behaviour of DRCC

In addition to beam depth, the clear distance between the split reverse channels (h) is another parameter which may have noticeable effect on the DRCC behaviour under monotonic loading. A number of simulations were performed to investigate the effects of this parameter on DRCC with varied beam sizes. Three RCC specimens; S15, S31 and S32, were used for this investigation. The beam sections used were UKB 533×210×92, UKB 457×191×106 and UKB 406×178×60 for S15, S31 and S32, respectively. The values of h were taken as 20, 30, 40 and 50 percentage of the beam depth. The specimens were labeled as DR20-S15 where DR is double reverse

channel connection; numbers are the percentage of the beam depth taken for h .

Figure 32 compares the results of changing clear distance (h) on the moment-rotation ($M-\phi$) curves of DRCC for different beam sizes. Comparing the moment-rotation ($M-\phi$) relationship for the original RCC with DRCC it is clear that the deformation of DRCC is more than the corresponding RCC, particularly, for the knee and post yield zone (Figure 32). But as far as the initial stiffness is concerned the DRCC with UKB 533×210×92 and UKB 457×191×106 beams is not capable of achieving similar initial stiffness as those of RCC. It was noted that there were sudden reduction in the initial stiffness values, up to 51% (Table 8). For the same beam size the changes in initial stiffness of DRCC is inversely proportional to the clear distance h (Table 8). For DRCC with UKB 457×191×106 beam there is 13.3% drop in initial stiffness as the clear distance h increased from 20 to 50 % of the beam depth. On the other hand, with the increase in distance h there is reduction in moment capacity values and fluctuations in values of rotational capacity. Few of the $M-\phi$ curves from Figure 32 are presented in Figure 32 to clearly highlight the possible effect of change in beam depth on the DRCC $M-\phi$ response for two constant percentage values of h , 20% and 50%. For these percentages, the $M-\phi$ behaviour appears to be similar, whilst the general behaviour of $M-\phi$ curves may indicate that there is a contribution of beam depth to the variation in rotation capacity and moment capacity. Therefore, there is need for further investigation of these types of connections with even deeper beams to clarify the possible effects of increase in beam depth to $M-\phi$ behaviour of such connections.

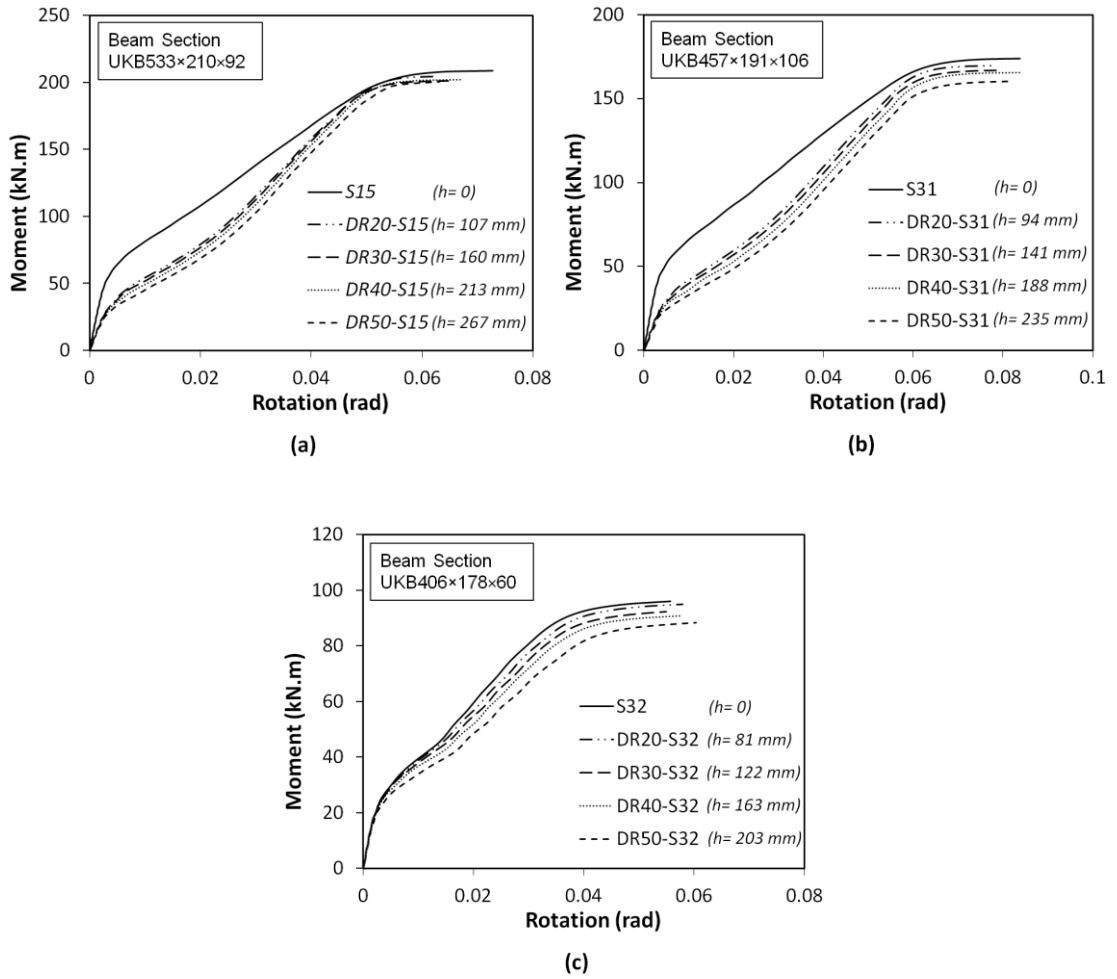


Figure 32: Effects of the variation of clear distance (h) between the split reverse channels for (a) S15, (b) S31 and (c) S32

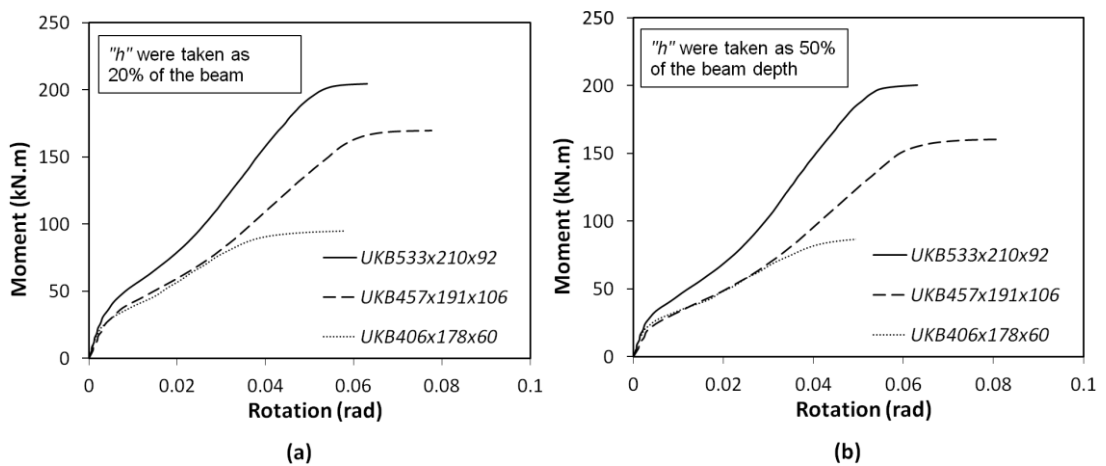


Figure 33: The effect of change in beam depth on the DRCC $M-\phi$ response for two constant percentage values of h for (a) 20% and (b) 50%

Table 8: Comparison of RCC and DRCC with varied clear distance (h) between the split reverse channels in terms of $M_{j,ult,FE}$, $S_{j,in,FE}$, $\phi_{j,ult,FE}$ and the observed failure modes

Specimen	$M_{j,ult,FE}$	$S_{j,in,FE}$	$\phi_{j,ult,FE}$	Failure mode
S15	208.7	20176.3	0.0728	BPO
DR20-S15	204.5	10331.9	0.0631	BPO
DR30-S15	201.1	9905.5	0.0647	BPO
DR40-S15	202.0	9373.6	0.0671	BPO
DR50-S15	200.3	8498.9	0.0631	BPO
S31	173.9	14494.9	0.0838	BPO
DR20-S31	169.7	7181.0	0.0776	BPO
DR30-S31	166.9	6964.4	0.0788	BPO
DR40-S31	165.6	6420.7	0.0838	BPO
DR50-S31	160.3	6226.3	0.0811	BPO
S32	96.0	9266.3	0.0557	BPO
DR20-S32	94.9	9203.1	0.0579	BPO
DR30-S32	92.3	9069.2	0.0549	BPO
DR40-S32	90.7	9124.0	0.0573	BPO
DR50-S32	88.3	8674.7	0.0603	BPO

Note: BPO denotes Bolt Pull-Out.

Chapter 6

MATHEMATICAL MODELING OF $M-\phi$ RELATIONSHIP OF RCC

6.1 General

Connections need to be strong enough with adequate rotation capacity in order to be cable of successfully transferring the forces and undergoing any required deformation without distress. Hence, there are rules already established for connection adequacy under statics or dynamic loading and further rules are needed for newly proposed connections. Since early 1930, the beam-column connections research had been focused on the moment-rotation characteristics, which correspond to its actual behavior. The experiments done have clearly demonstrated that all joints exhibit a certain degree of flexibility to an applied loading and they behave in nonlinearly manner. This proves that most of the beam-column connections in practice are semi-rigid. In recent years, much effort has been focused on determining the moment-rotation ($M-\phi$) relationships of various semi-rigid connections. For the purposes of either predicting the connection behavior or incorporate the behavior into a frame analysis computer program, the results of moment-rotation ($M-\phi$) curves were then modeled by using mathematical representation. In this chapter, the methods of modeling moment-rotation curves and several commonly used connection models are described.

6.2 Mathematical Modeling of Moment-Rotation Curve

Since the early studies, the mathematical modeling of moment-rotation curves for semi-rigid connections have been developed by using different relationships, which was dependent on the degree of accuracy required in the semi-rigid frame analysis. Table 9 shows numerous past attempts to represent the moment-rotation curve in mathematical form. Through this table, a comparison of these forms along with their advantages and drawbacks are demonstrated. It should be noted that the non-linear model efficiently agree with the dotted line which implies that it adequately represents the moment-rotation collected from test data.

6.2.1 The Non-linear Moment-Rotation Models

The non-linear representation of the connection $M-\phi$ relationship shows sufficient reliable representation of the key parts of the connection behaviour. As reflected in the available literature, a number of models were proposed on this basis to model $M-\phi$ curves. Namely, they are the polynomial model, the cube B-spline model, the bounding line model, the power model and the exponential model. In addition, for design purpose, the Eurocode 3-(revised) Annex J (CEN, 1997) suggested a non-linear $M-\phi$ curve, which is very close to tri-linear behaviour, with plastic rotational stiffness equal to zero. Table 10 briefly elucidates on some of these models along with the relevant equations. Only a few of these models are close to demonstrating the characteristics of moment-rotation behaviour through the full range of loading/rotation (Chisala, 1999). For example; the polynomial model may yield negative tangent stiffness at some value of connection moment. In addition, the parameters implemented in this model have very little physical meaning (Mohamadi-shooreh & Mofid, 2008). Despite the high level of accuracy of the multi-parameters

exponential function in curve-fitting process, they need a large domain data which makes them difficult to use. As a rule of thumb, a good mathematical function should be simple with few parameters, easy in determination of these parameters, capable of representing a wide range of connection types, physically meaningful, numerically stable and containing no negative first-derivative (Chan & Chui, 2000).

6.2.2 Modelling Functions

Based on literature survey (Table 10), it is clear that some models are better than others in terms of accuracy and convenience. Therefore, there is necessity to select adequate and accurate function to represent RCC behavior in order to be used in computerized structural analysis. The selection of the adequate model has to be based on the comparison of the curve fitting results with the available experimental ones. Hence, six models; Ang-Morris (1984), Kishi-Chen (1987), Yee-Melchers (1985), Chisala (1999), Richard-Abbott (1975) and Wu-Chen (1990); were fitted to the dimensionless forms of experimental results by Wang and Xue (2013). The optimization toolbox (solver add-in) implemented in Excel was adapted to fit the experimental data. The method used in this tool is the GRG (Generalized Reduced Gradient) algorithm which considered as one of the most robust nonlinear programming. The objective function was to minimize the square of residuals of the data points relative to the fitted function. In order to measure the goodness and accuracy of the fit, the coefficient of determination (R^2) and standard error of estimate ($S_{\phi,M}$ or $S_{M,\phi}$) were measured. On the basis of these values, the best fitted formulation is the one having bigger R^2 with less $S_{M,\phi}$.

Table 9: Comparison of different mathematical representations for the ($M-\phi$) curve (Chan & Chui, 2000, Faella, Piluso, & Rizzano, 2000)

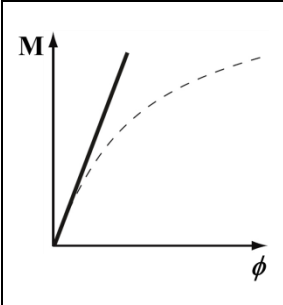
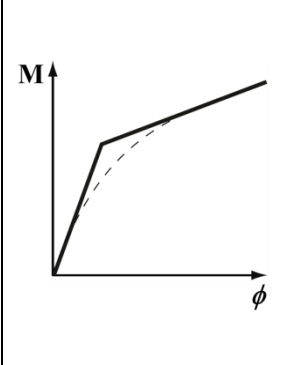
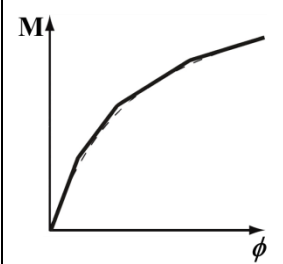
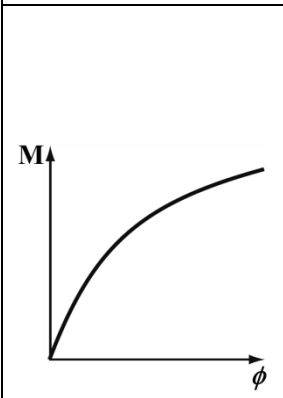
Type of Model	Name	References	Advantages	Drawbacks
	Linear	<ul style="list-style-type: none"> - Batho and co-workers (1931,1934,1936) - Baker (1934) - Rathbun (1936) - Monforton and Wu (1963) - Arbabi (1982) - Chan (1994) 	<ul style="list-style-type: none"> - The simplest model. - One parameter is required; the initial stiffness. 	<ul style="list-style-type: none"> - Inaccurate in the large deflection range.
	Bi-linear	<ul style="list-style-type: none"> - Lionberger and Weaver (1967) - Romstad and Subramanian (1970) - Maxwell et al. (1981) - Melchers and Kaur (1982) - Sugimoto and Chen (1982) - Lui and Chen (1983) 	<ul style="list-style-type: none"> - Simple to use. - Shows significant improvement than linear model. - Three parameter are required; the initial stiffness, post-yield stiffness and plastic flexural resistance. 	<ul style="list-style-type: none"> - The change of stiffness in the knee region of ($M-\phi$) curve not being able to account.
	Multi-linear	<ul style="list-style-type: none"> - Moncarz and Gerstle (1981) - Vinnakota (1983) - Razzaq (1983) - Stelmack et al. (1986) - Gerstle (1988) 	<ul style="list-style-type: none"> - Shows significant improvement than bi-linear model. - Have a very clear physical meaning. 	<ul style="list-style-type: none"> - Required many parameters.
	Non-linear	<ul style="list-style-type: none"> - Frye and Morris (1975) - Krishnamurthy et.al (1979) - Jones et al. (1980) - Colson and Louveau (1983) - Ang and Morris (1984) - Lui and chen (1986) - Yee and Melchers (1986) - Kishi and Chen (1987) - King and Chen (1993) - etc.... 	<ul style="list-style-type: none"> - Very high degree of accuracy. - Some proposed models have a very clear physical meaning. - The change in stiffness is clearly accounted. 	<ul style="list-style-type: none"> - Some proposed models contain negative first-derivative and they are numerically unstable.

Table 10: Different non-linear M - ϕ models (Chan & Chui, 2000, Faella, Piluso, & Rizzano, 2000, Mohamadi-Shoore & Mofid, 2011)

Type of Model	Model Name	Year	Function	No. of Parameters	Remarks
Polynomial Model	Frye-Morries	1975	$\phi = C_1(KM) + C_2(KM)^3 + C_3(KM)^5$	4	<ul style="list-style-type: none"> - C_1, C_2 and C_3 can be determined from curve –fitting. - K is a standardization parameter depending on the geometrical and mechanical properties of the connection. - The tangent connection stiffness may become negative at some value of connection moment M.
	Picard-Giroux	1976	$\phi = C_1(KM) - C_2(KM)^2 + C_3(KM)^5$	4	
Power Model	Two-parameter	1936 1979	$\phi = C M^\alpha$	2	<ul style="list-style-type: none"> - C and α are two curve-fitting parameters ($C > 0$ and $\alpha > 0$)
	Colson-Louveau	1983	$\phi = \frac{ M }{K_i} \frac{1}{1 - M/M_u ^n}$	3	<ul style="list-style-type: none"> - K_i is the initial connection stiffness. - M_u is the ultimate moment capacity. - n is the shape factor.
	Kishi and Chen	1987	$\phi = \frac{M}{K_i} \frac{1}{[1 - (M/M_u)^n]^{1/n}}$	3	
	Ramberg-Osgood	1943	$\phi = \frac{M}{K_i} (1 + K(M/K_i)^{n-1})$	3	<ul style="list-style-type: none"> - K is expressed by means of the bending moment giving rise, after unloading, to a permanent rotation.
	Ang-Morris	1984	$\frac{\phi}{\phi_o} = \frac{ KM }{(KM)_o} \left[1 + \left(\frac{ KM }{(KM)_o} \right)^{n-1} \right]$	3	<ul style="list-style-type: none"> - ϕ_o and $(KM)_o$ are constants defining the position of intersection point on the curve. - K is a dimensionless factor dependent on the connection type and geometry.
	Richard-Abbott	1975	$M = \frac{(K_i - K_p) \phi }{\left[1 + \left \frac{(K_i - K_p) \phi }{M_o} \right ^n \right]^{1/n}} + K_p \phi $	4	<ul style="list-style-type: none"> - K_p is the strain-hardening stiffness. - M_o is a reference moment.

Table 10: (Continued)

Type of Model	Model Name	Year	Function	No. of Parameters	Remarks
Exponential Model	Lui and Chen	1986 1988	$M = M_o + \sum_{j=1}^n C_j \left[1 - \exp\left(\frac{- \phi }{2j\alpha}\right) \right] + K_p \phi $	4	- M_o is the initial moment. - α is the scaling factor. - C_j is the curve-fitting coefficient. - n is the number of terms considered.
	Yee and Melchers	1986	$M = M_u (1 - \exp(-\frac{\phi}{M_u} (K_i - K_p + C\phi))) + K_p \phi$	4	- C is constant controlling the slope of the curve.
	Wu and Chen	1990	$\frac{M}{M_u} = n \left(\ln\left(1 - \frac{K_i \phi}{M_u}\right) \right)$	3	- n is determined empirically from test data
	Chisala	1999	$M = (M_o + K_p \phi) \left(1 - \exp\left(\frac{-K_i \phi}{M_o}\right) \right)$	3	- M_o is the intercept-constant.

Table 11: Coefficient of determination and standard error of estimate: comparison between fitted models of RCC

Test	Ang-Morris Model		Kishi-Chen Model		Yee-Melcher Model		Chisala Model		Richard-Abbott Model		Wu-Chen Model	
	R^2	$S_{\phi.M}$	R^2	$S_{M.\phi}$	R^2	$S_{M.\phi}$	R^2	$S_{M.\phi}$	R^2	$S_{M.\phi}$	R^2	$S_{M.\phi}$
1	0.848	1.429	0.978	0.052	0.732	0.184	0.732	0.184	0.957	0.074	0.584	0.229
2	0.930	0.709	0.965	0.097	0.919	0.147	0.918	0.148	0.971	0.088	0.909	0.156
3	0.914	1.800	0.927	0.130	0.910	0.144	0.910	0.144	0.972	0.080	0.872	0.171
4	0.803	1.829	0.968	0.060	0.701	0.184	0.701	0.184	0.941	0.082	0.538	0.229
5	0.781	1.240	0.959	0.065	0.493	0.229	0.492	0.229	0.926	0.087	0.596	0.205

Note: $S_{\phi.M}$ denotes standard error of estimate of $\phi/\phi_{j,R}$ on $M/M_{j,R}$, $S_{M.\phi}$ denotes standard error of estimate of $M/M_{j,R}$ on $\phi/\phi_{j,R}$.

The comparison between fitted models is summarized in Table 11. In addition, the normalized moment-rotation ($M-\phi$) curves for Test 1-5 with fitted models are also given in Appendix C, Figures C1 to C5. It can be seen from Table 11 that the Kishi-Chen function has the best agreement with the data when compared to other functions, since it has bigger R^2 with less $S_{M,\phi}$. While, the Richard-Abbott model has the second rank with its satisfactory fit. Therefore, Kishi-Chen and Richard-Abbott models are adopted in this study to represent the $M-\phi$ characteristics of RCC.

6.2.3 The Kishi and Chen Model (Three-Parameter Power Model)

The model developed by Kishi and Chen (1987) depends on three main parameters: the initial stiffness ($S_{j,in}$), the ultimate moment capacity ($M_{j,ult}$) and the shape parameter (n). This model is found suitable and adjustable for representing the realistic behaviour of semi-rigid connections, especially for single and double web-angle connections and top- and seat angle connections with or without double web angle (Chen & Kishi, 1989). Later, Abolmaali et al. (2005) found out that Kishi and Chen model is also adequate to use for flush end-plate connections with one row of bolts.

The three-power model can be expressed as:

$$M = \frac{S_{j,in} \phi}{\left[1 - (S_{j,in} \phi / M_{j,ult})^n\right]^{1/n}} \quad (6)$$

Bahaari and Sherbourne (1997) suggested that, for design purposes, in order to eliminate the dimensional effect, it is desirable to represent the function in normalized manner. Therefore, the plastic flexural resistance of the joint, $M_{j,R}$, and the corresponding rotation, $\phi_{j,R}$, (Figure 16) are selected to normalize the moment and rotation axes, respectively. Equation (6) can be rewritten in normalized form as:

$$M_n = \frac{\phi_n}{\left[1 - (\phi_n / M_{j,ult,n})^n\right]^{1/n}} \quad (7)$$

where, $M_n = M/M_{j,R}$ and $\phi_n = \phi/\phi_{j,R}$: are normalized moment and normalized rotation, respectively. $M_{j,ult,n} = M_{j,ult}/M_{j,R}$ is normalized ultimate moment capacity.

6.2.4 The Richard-Abbott Model

The model proposed by Richard-Abbott (1975) requires four parameters: the initial stiffness ($S_{j,in}$), the post-yield stiffness ($S_{j,P}$), the intercept-constant or the plastic flexural resistance of the joint ($M_{j,R}$) and the shape parameter (n). Despite the fact that this model needs four parameters, it always provides a positive stiffness and gives good fit to the knee region due to the fitted curve being forced to pass through the points before and after the knee region (Bahaari & Sherbourne, 1997). Furthermore, it was found adequate and applicable to predict the key parameters of semi-rigid connections bi-linear behaviour, especially those with a strain-softening behavior (Chan & Chui, 2000). The model can be represented as:

$$M = \frac{(S_{j,in} - S_{j,P})\phi}{\left[1 + \left|\frac{(S_{j,in} - S_{j,P})\phi}{M_{j,R}}\right|^n\right]^{1/n}} + S_{j,P}\phi \quad (8)$$

Similar to Equation (7), the normalized form of equation (8) can be expressed as:

$$M_n = \frac{(1 - S_{j,P,n})\phi_n}{\left[1 + \left|(1 - S_{j,P,n})\phi_n\right|^n\right]^{1/n}} + S_{j,P,n}\phi_n \quad (9)$$

where $S_{j,P,n} = S_{j,P} \cdot \phi_{j,R} / M_{j,R}$ is the strain-hardening stiffness of dimensionless curve.

6.2.5 Model Suggested by Eurocode-3

The moment-rotation curve offered in *Eurocode 3-(revised) Annex J* (CEN, 1997) is characterized by three behavioural ranges: the linear elastic region, the transition (non-linear) region and perfectly plastic region. As illustrated in Figure 34, the suggested curve is very close to tri-linear behaviour with plastic rotational stiffness equal to zero. The first region is valid when the bending moment experienced by the connection is less than the maximum elastic joint moment resistance defined as $2/3 M_{j,Rd}$. The slope in this case is taken equal to the initial stiffness $S_{j,ini}$. In the second region, non-linear part, the behaviour can be described as:

$$M = \frac{S_{j,ini}}{\left(1.5 \frac{M}{M_{j,Rd}}\right)^\psi} \phi \quad \text{for } \frac{2}{3} M_{j,Rd} < M \leq M_{j,Rd} \quad (10)$$

Where, the parameter ψ is the shape factor which is mainly dependent on the connection geometry. It is suggested to be equal to 2.7 for the welded connections and end-plate connections, while for top and seat angle connections the value of 3.1 is recommended (Faella, Piluso, & Rizzano, 2000). Finally, the third region defined by the secant rotation, S_j , which is equal to $1/3$ of $S_{j,ini}$ for $\psi = 2.7$ and $1/3.5$ of $S_{j,ini}$ for $\psi = 3.1$. In this case, the bending moment is equal to the design resistance $M_{j,Rd}$. It should be noted that the change of stiffness in the knee region of $M-\phi$ curve is characterized by post-yield rotational stiffness, $S_{j,P}$, as follows:

$$S_{j,P} = \frac{S_{j,ini}}{3\left(1.5^\psi - \frac{2}{3}\right)} \quad (11)$$

producing $S_{j,P}$ equal to $1/7$ of $S_{j,ini}$ for $\psi = 2.7$ and $1/8.5$ of $S_{j,ini}$ for $\psi = 3.1$.

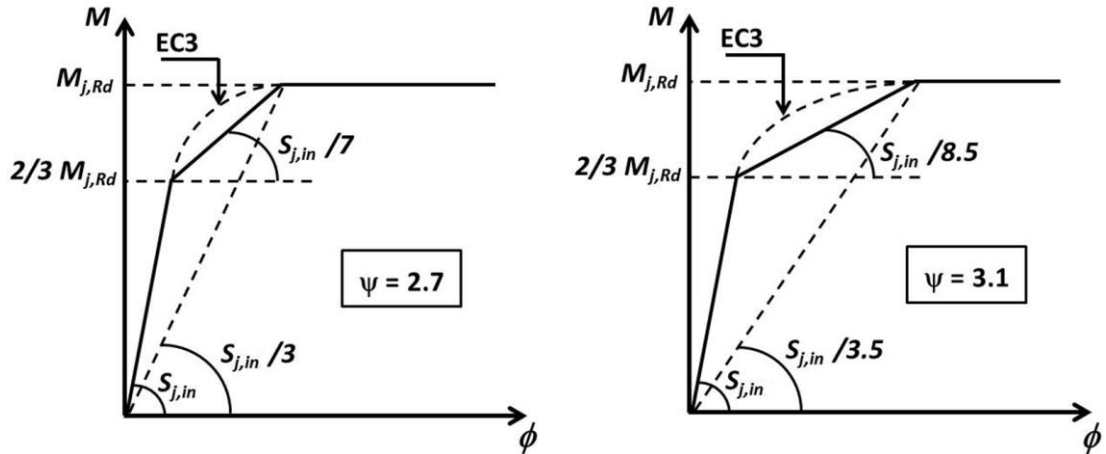


Figure 34: The Eurocode 3 representation of the moment-rotation curve (Faella, Piluso, & Rizzano, 2000)

In order to examine the EC3 Annex J model for RCC, a comparison between the EC3 Annex J model and experimental results by Wang and Xue (2013) was carried out to evaluate this model in terms of accuracy and convenience. The results of this comparison are depicted in Figure 35, where the design moment resistance of the joint, $M_{j,Rd}$, is evaluated by means of the secant rotation, S_j , which is equal to one-third of the initial stiffness. This implies that the shape factor (ψ) is equal to 2.7, which is recommended for end-plate connections. According to Figure 35 (a), (c) and (d), which are for Tests 1, 3 and 4, respectively, it should be noted that the suggested formulation of Eurocode 3-(revised) Annex J leads to satisfactory agreement with experimental $M-\phi$ curves. While, the Eurocode 3 formulations of Test 2 and 5 (Figure 35 (b) and (e)) resulted in a significant overestimation of the knee region behaviour. This raises the necessity for more investigation on the suitability of shape factor value of 2.7 and the equation for finding the secant rotation, S_j , which correspond to $M_{j,Rd}$ for RCC.

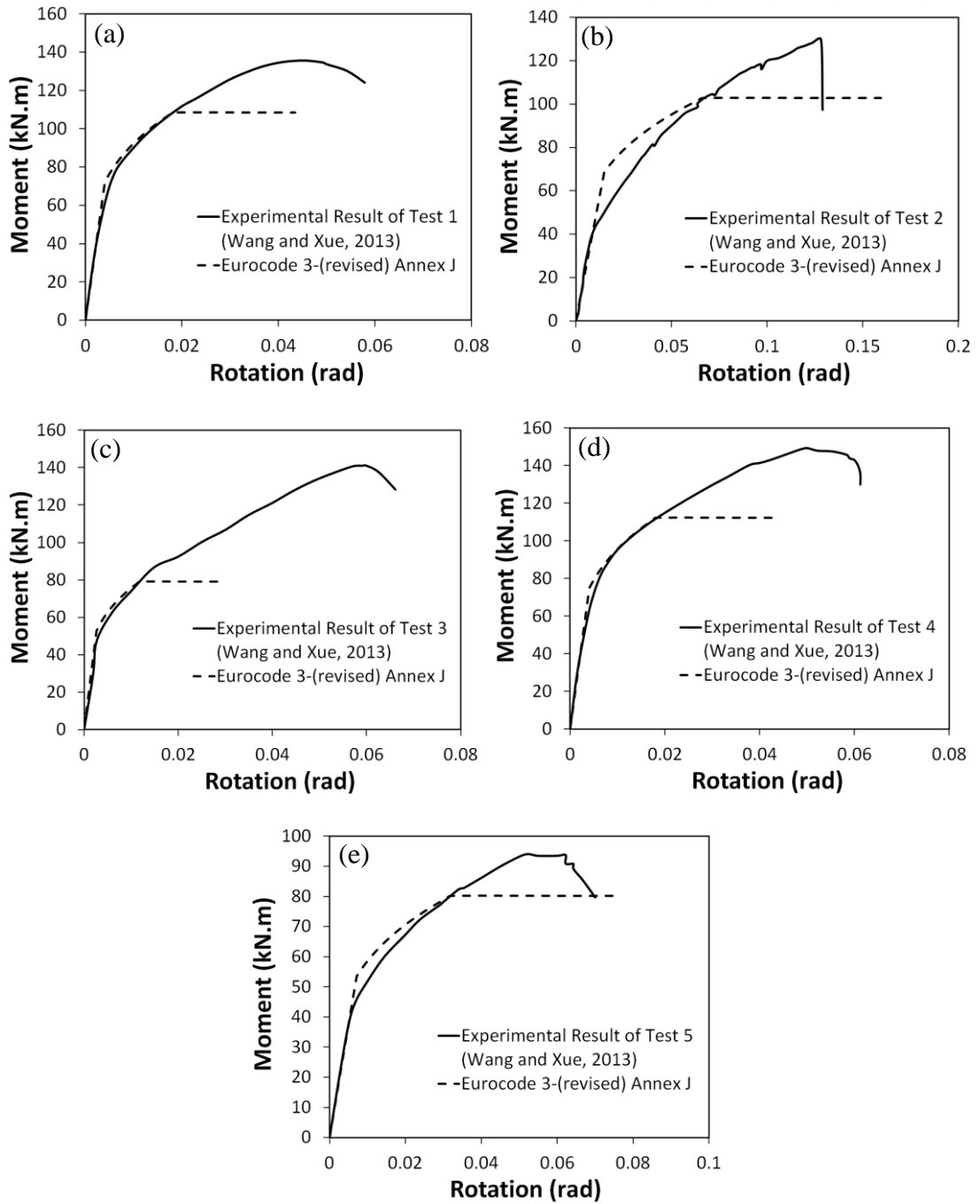


Figure 35: Comparison between EC3 Annex J model and Moment-rotation curves from experimental: (a) Test 1, (b) Test 2, (c) Test 3, (d) Test 4 and (e) Test 5

6.3 Mathematical Function of RCC

6.3.1 Selection of Parametric Study Cases

In order to develop the standardized moment–rotation function for RCC, different ranges of geometric parameters were selected based on recommendations of handbooks and practical details of flush end-plate connections. According to the work done by Bahaari and Sherbourne (1997), the geometrical parameters could be selected in non-dimensional form with respect to particular parameters; such as beam depth (Krishnamurthy, Huang, Jeffrey, & Avery, 1979) or end-plate width (Kukreti, Ghassemieh, & Murray, 1990) so that the standardized equations do not depend on unit. It is also possible to choose ranges of geometrical parameters and then the standardized equations could be presented in non-dimensional form. The following ranges of geometrical parameters for RCC components were selected (Figure 36):

1. Six standard column sections: SHS 260×10, SHS 250×10, SHS 200×10, SHS 180×10, SHS 160×10 and SHS 140×10.
2. Five standard beam sections: UKB 457×191×106, UKB 406×178×60, UKB 356×127×33, UKB 305×165×40 and UKB 254×102×28.
3. Six flush end-plate thicknesses (t_p): 12, 15, 18, 20, 22 and 25 mm.
4. Six gage distances (g): 70, 80, 90, 100, 120 and 140 mm.
5. Six bolt pitches (p_f): 40, 45, 50, 60, 80 and 100 mm.
6. Six channel flange thicknesses (t_{fc}): 8, 10, 10.5, 12, 12.5 and 14 mm.
7. Seven channel web thicknesses (t_{wc}): 6, 6.5, 7, 7.5, 8, 10 and 12 mm.
8. Four values of channel width (m): 75, 90, 100 and 120 mm.
9. Three bolt diameters (d_{bolt}): 16, 20 and 24 mm

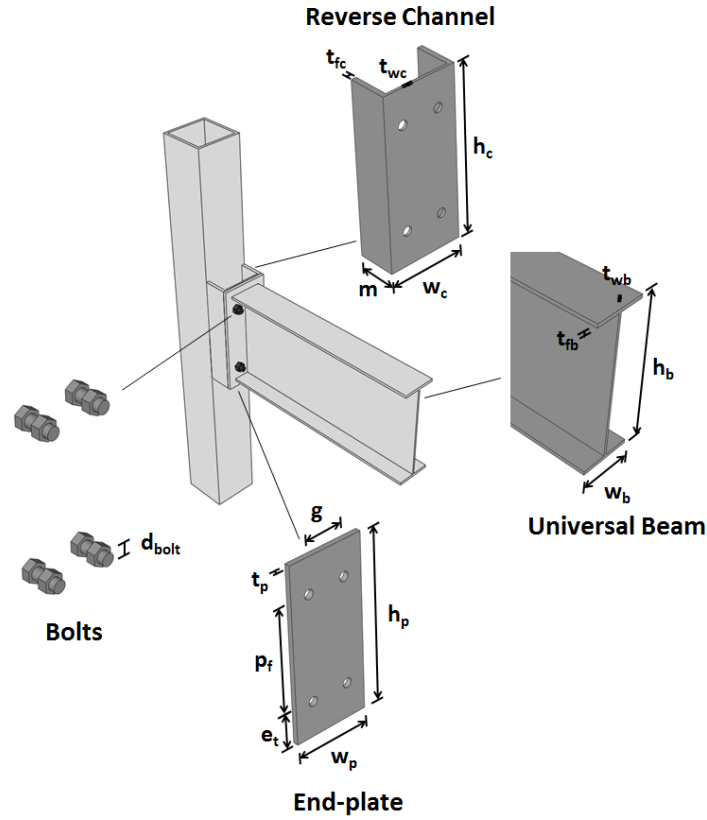


Figure 36: General description of the geometrical parameters used in parametric study

The width and the height of flush end-plate were taken according to the assumptions given by Mohamadi-shooreh and Mofid (2008); these assumptions were based on the results of an industrial survey and the steel structures design handbooks.

$$w_p = w_b + \max\{30mm, 2t_p\} \quad (12)$$

$$h_p = h_b + \max\left\{30mm, 2t_p, \frac{w_p t_p^2}{4w_b t_{fb}}\right\} \quad (13)$$

For the sake of simplicity, it was assumed that the heights of channel and flush end-plate were equal, the ratio of flush end-plate width to channel width was kept to a minimum value of 0.89 and the minimum value of the ratio of reverse channel depth to SHS width was kept equal to 0.72 (AlHendi & Celikag, 2015).

Since the steel grade of the beam and end-plate has no effect on the initial stiffness (Mohamadi-Shoore & Mofid, 2011), S355 steel grade was used for beams, columns, flush end-plates and channel sections and Grade 8.8 was used for standard M20 bolts.

It was found that 18,144 separate RCC combinations would correspond to the selected ranges of aforementioned parameters. A part of this huge number of combinations could be eliminated due to not being practical. For this reason, practical instructions and limitations suggested by Mohamadi-shooreh and Mofid (2008) were applied as follows:

1. For gage distance (g): $t_{wb} + 2d_{bolt} + 30mm \leq g$ and $1.5d_{bolt} \leq \frac{w_p - g}{2}$
2. For bolt pitch (p_f): $d_{bolt} + 20mm \leq p_f$ and $1.5d_{bolt} \leq \frac{h_b - 2t_{fb}}{2} - p_f$
3. For flush end-plate thickness (t_p): $0.71 \leq 2.5t_p \sqrt{z/Z_b} \leq 2$ and $1.17 \leq d_{bolt}/t_p \leq 1.96$

where, z is the vertical distance between the tension bolt center and centerline of compression flange, Z_b is the beam plastic modulus.

Consequently, 140 specimens of RCC were considered in the parametric study, since they were the most practical specimens. Tables A.1-A.5 (Appendix A) summarizes the dimensions of these joints. Based on the beam sections, all joints were divided into sets (Set1 to Set5). The finite element models for all sets were prepared according to section 3.3. The main parameters, as defined in section 3.3.3, and failure modes obtained from finite element models are given in Tables A.6-A.10 (Appendix

A). Moreover, Von Mises stress contour of selected joints prior to failure are illustrated in Figures B1-B8 (Appendix B).

6.3.2 Normalized Moment-Rotation Function

The graphs in Figure 37 illustrate the moment-rotation curves for Set1 to Set5. As already stated in section 6.2.3, it is desirable to represent the moment-rotation curves in normalized manner in order to eliminate the dimensional effect. Therefore, the moment and rotation axes of Figure 37 are normalized by the plastic flexural resistance of the joint, $M_{j,R}$, and the corresponding rotation, $\phi_{j,R}$, for each curve, respectively. As an example, the normalized form of the moment-rotation curves for Set4 (Figure 37 (d)) is shown in Figure 38.

6.3.3 Standardized Function of RCC

On the basis of the derivation of a standardized moment-rotation function for RCC, the Kishi-Chen (1987) and Richard-Abbott (1975) functions were fitted to the dimensionless forms of numerically measured moment-rotation curves of Figure 37. With the objective function of minimizing the square of residuals, the goodness and accuracy of the fit were computed by measuring the coefficient of determination (R^2) and standard error of estimate ($S_{M,\phi}$). The results indicated that the coefficient of determination (R^2) of the Kishi-Chen and Richard-Abbott functions fits were within the ranges of 0.897 to 0.999 and 0.980 to 0.999, respectively, while the standard error of estimate ($S_{M,\phi}$) were within the ranges of 0.010 to 0.495 and 0.009 to 0.176, respectively. By considering these ranges, it is asserted that the Richard-Abbott function is capable of achieving accuracy when compared to that of the Kishi-Chen function. Further comparison of the Kishi-Chen and Richard-Abbott functions is also illustrated in Figure 39; where three RCC, with low, medium and high initial

stiffness, were selected from each set. It can be seen that the Richard-Abbott fits were better than those of Kishi-Chen in all cases.

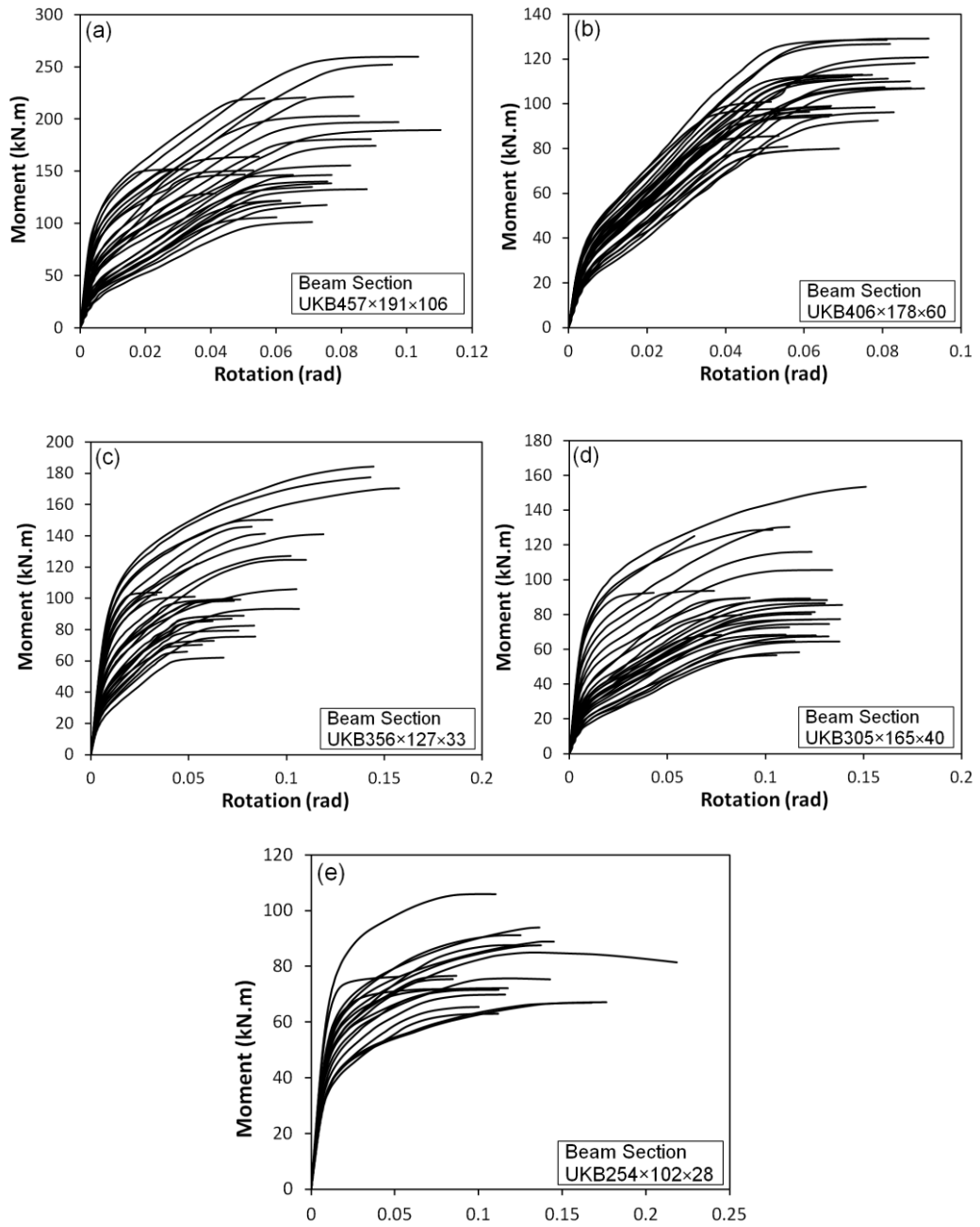


Figure 37: Moment-rotation curves from FE models for RCC: (a) Set1, (b) Set2, (c) Set3, (d) Set4 and (e) Set5

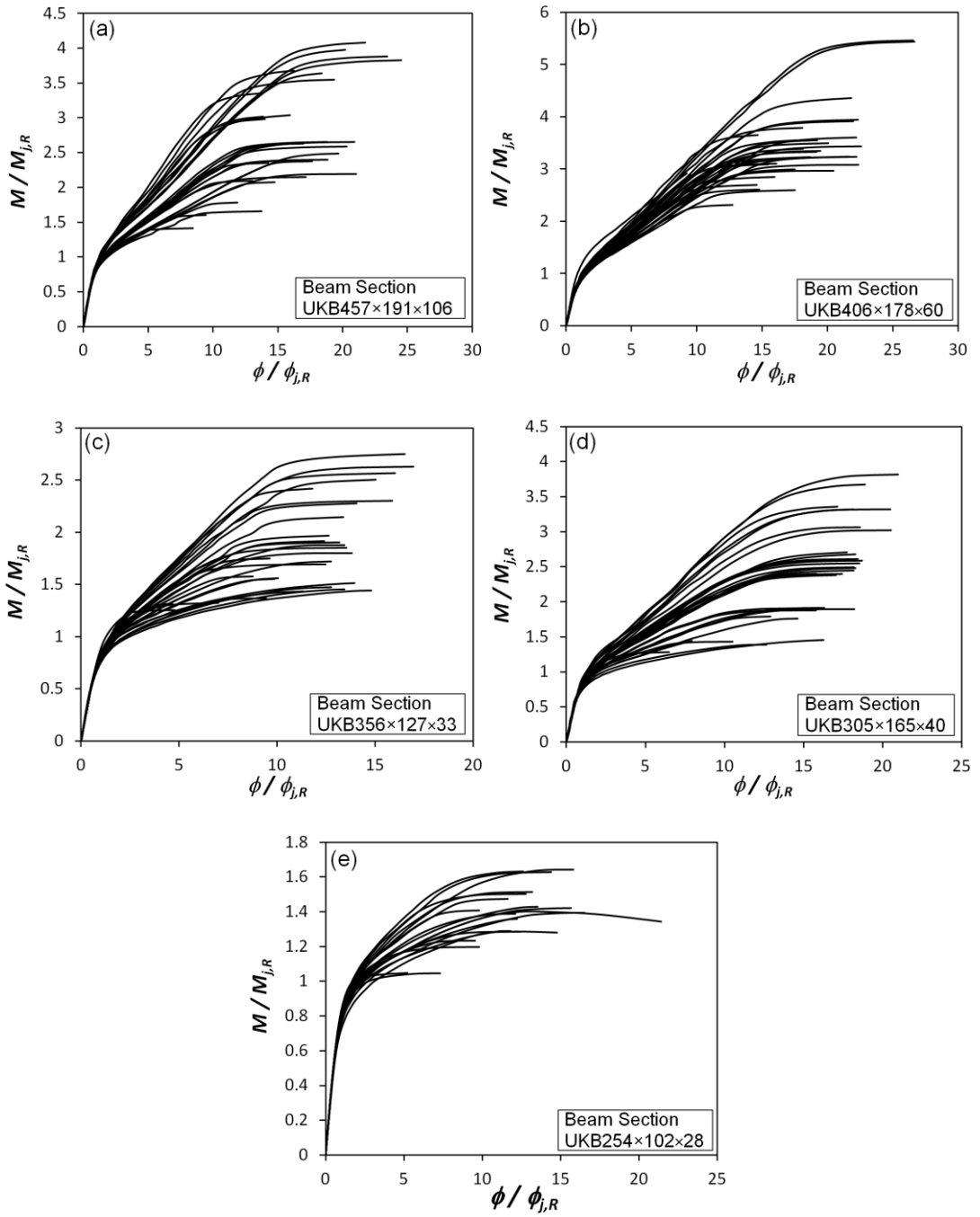
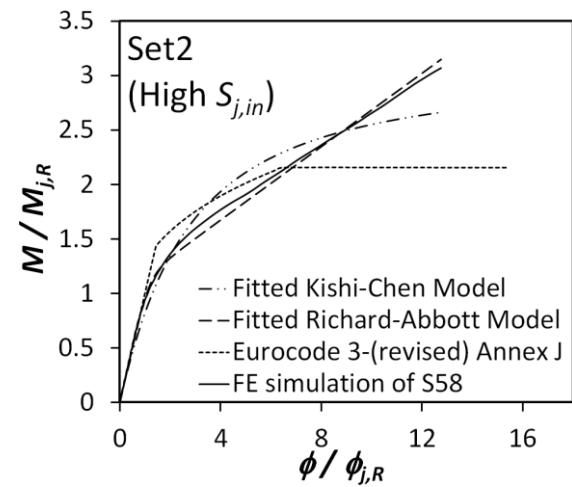
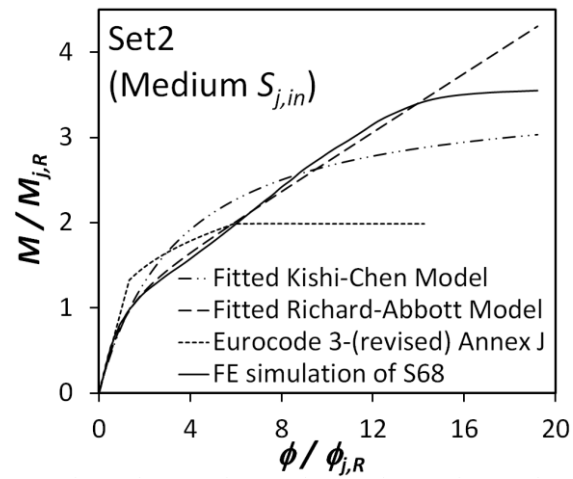
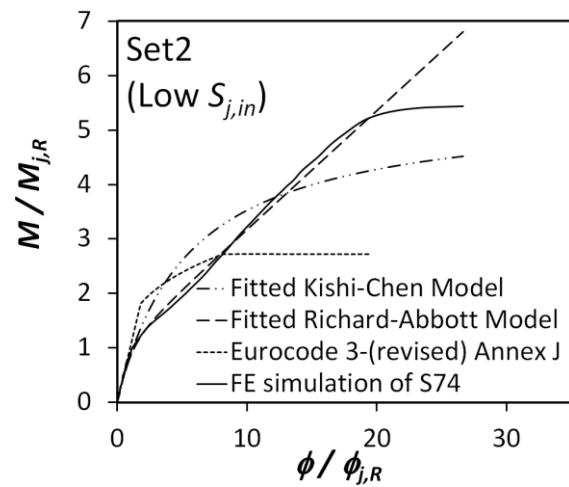
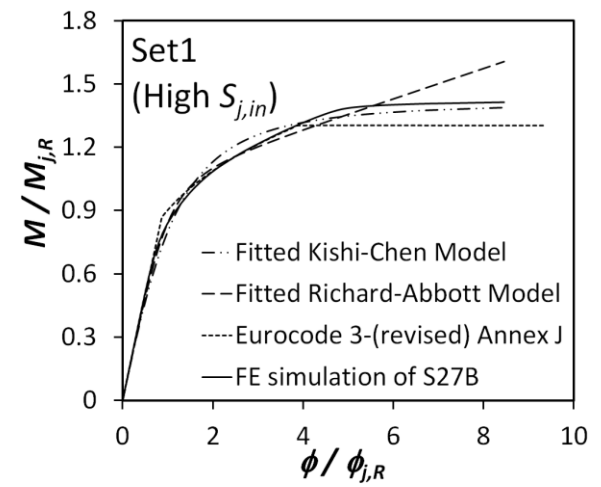
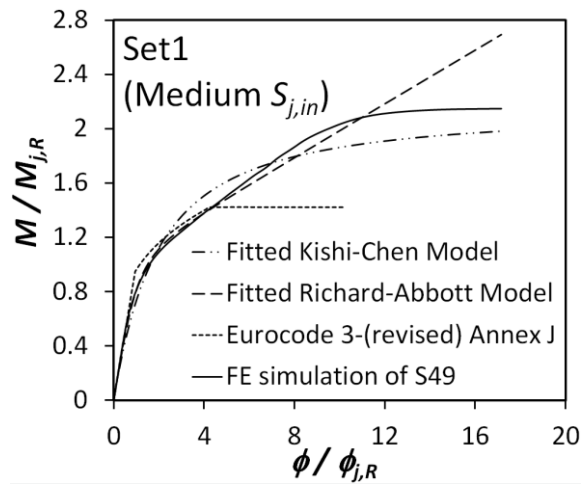
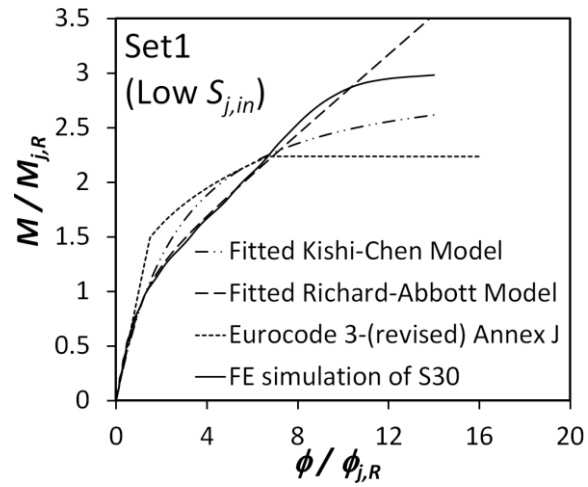
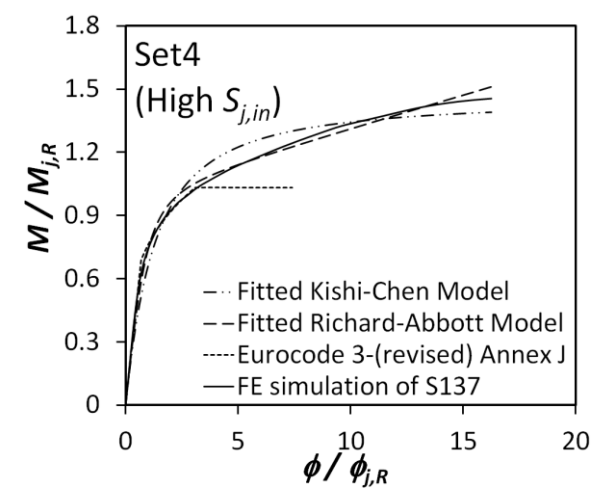
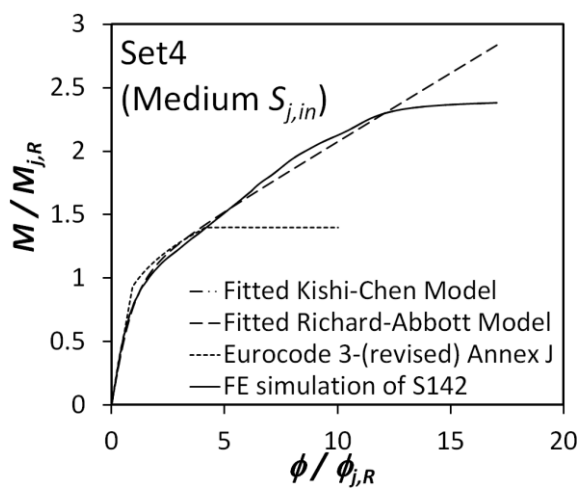
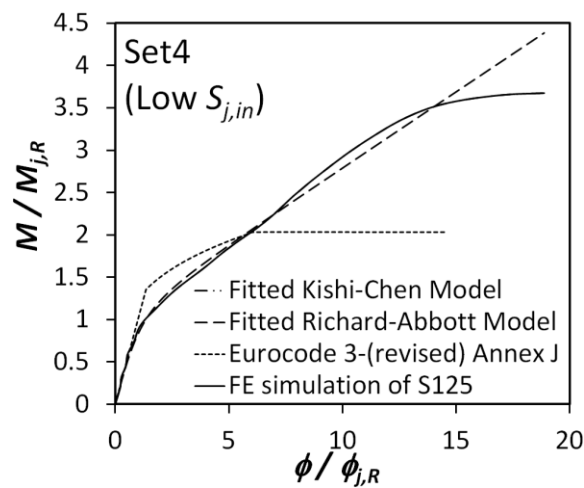
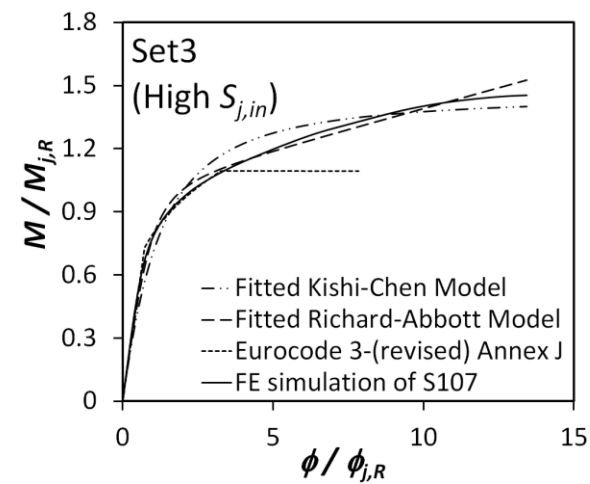
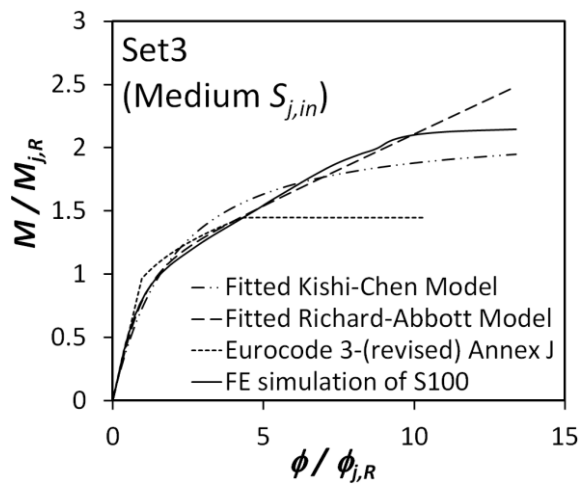
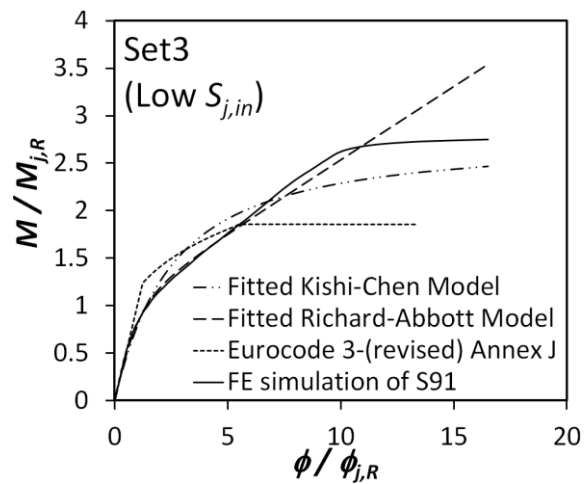


Figure 38: Normalized form of moment-rotation curves: (a) Set1, (b) Set2, (c) Set3, (d) Set4 and (e) Set5





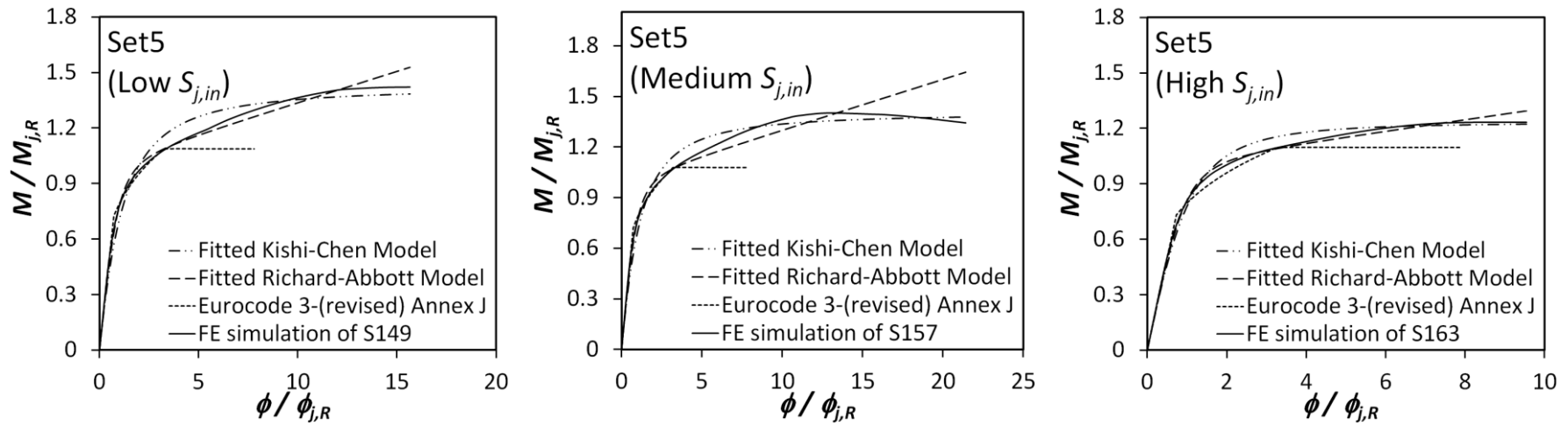


Figure 39: Comparison of analytical $M-\phi$, Kishi-Chen and Richard-Abbott curve fit and Eurocode 3-(revised) Annex J for RCC with low, medium and high initial stiffness

In order to derive the standardized moment-rotation function for RCC, it was required to express the normalized form of Kishi-Chen parameters ($M_{j,ult,n}$, $M_{j,R}$, $\phi_{j,R}$, and n) and the Richard-Abbott parameters ($S_{j,P,n}$, $M_{j,R}$, $\phi_{j,R}$, and n) in terms of geometrical properties of a connection as follows:

$$M_{j,R} = \prod_{j=1}^m q_j^{a_j}; \quad \phi_{j,R} = \prod_{j=1}^m q_j^{b_j} \quad (14)$$

$$M_{j,ult,n} = \prod_{j=1}^m q_j^{c_j}; \quad n = \prod_{j=1}^m q_j^{d_j} \quad (15)$$

$$S_{j,P,n} = \prod_{j=1}^m q_j^{e_j}; \quad n = \prod_{j=1}^m q_j^{f_j} \quad (16)$$

In Eqs. (14-16), q_j is j^{th} size parameter; a_j , b_j , c_j , d_j , e_j and f_j are exponents that indicate the effect of the j^{th} geometric parameter and m is the number of connection geometric parameters considered. The coefficients (a_j - f_j) can be obtained by multiple linear regression analysis after taking logarithms of both sides of Eqs. (14-16).

Regarding the independent variables involved in the empirical formulations of RCC, these variables (Figure 36) were identified as follows: h_b = overall depth of beam; t_{fb} , t_{fc} = flange thickness of beam and channel, respectively; t_{wb} , t_{wc} = web thickness of beam and channel, respectively; m = width of channel; t_p = flush end-plate thickness; g = gage distance; p_f = bolt pitch and d_{bolt} = nominal bolt diameter.

The following expressions were derived for the Kishi-Chen and Richard-Abbott functions parameters:

$$M_{j,R} = \frac{5.495 \times 10^{-2} (d_{bolt})^{1.354} (t_{fb}/h_b)^{-2.324} (t_{fc}/t_{wc})^{-0.309} (t_p/t_{wc})^{0.123} (g/d_{bolt})^{0.834}}{(t_{wb}/h_b)^{-2.399} (t_{wc})^{-1.400} (p_f/d_{bolt})^{0.182}} \quad (17)$$

$$\phi_{j,R} = \frac{4.048 (d_{bolt}/h_b)^{0.981} (t_{fb}/h_b)^{-1.525} (t_{fc}/t_{wc})^{-0.167} (m)^{-0.151}}{(t_{wb}/h_b)^{-1.747} (t_{wc}/h_b)^{-0.532} (t_p/t_{wc})^{-0.281} (g/d_{bolt})^{-0.242}} \quad (18)$$

$$M_{j,ult,n} = \frac{0.224 (h_b)^{1.215} (t_{fb})^{3.054} (t_{wb})^{-3.167} (t_{wc})^{-0.801} (g/d_{bolt})^{-0.743}}{(d_{bolt})^{0.996} (t_p/t_{wc})^{-0.170} (p_f/d_{bolt})^{0.267}} \quad (19)$$

$$n_{\text{Kishi-Chen}} = \frac{77.353 (d_{bolt})^{-0.217} (h_b)^{-0.447} (t_{fb}/h_b)^{-1.611} (t_{fc}/t_{wc})^{0.130} (m)^{-0.160} (t_p/t_{wc})^{0.061}}{(t_{wb}/h_b)^{-1.858} (t_{wc})^{-0.627} (p_f/d_{bolt})^{-0.071}} \quad (20)$$

$$S_{j,p,n} = \frac{1.678 \times 10^{-3} (d_{bolt})^{-0.929} (h_b)^{1.285} (t_{fb}/h_b)^{2.360} (m)^{-0.101} (t_p/t_{wc})^{0.486} (g/d_{bolt})^{-0.567}}{(t_{wb}/h_b)^{2.634} (t_{wc})^{0.836} (p_f/d_{bolt})^{0.116}} \quad (21)$$

$$n_{\text{Richard-Abbott}} = \frac{18.822 (d_{bolt})^{-0.187} (h_b)^{-0.296} (t_{fb}/h_b)^{-0.422} (t_p/t_{wc})^{0.132}}{(t_{wb}/h_b)^{-0.540} (t_{wc})^{-0.439}} \quad (22)$$

The ability of the proposed equations (Eqs. 17-22) to represent the normalized form of Kishi-Chen and Richard-Abbott parameters are demonstrated in Figure 40, where the results obtained from these predicted functions compared to the actual results obtained from the finite element analyses. The bold line drawn with a slope of 1:1 and the values on this line is defined as a perfect fit. In this figure, two lines showing the $\pm 20\%$ error limits are also indicated. Moreover, the coefficient of determination (R^2) and standard error of estimate of predicted values on those of actual ($S_{P,A}$) were measured.

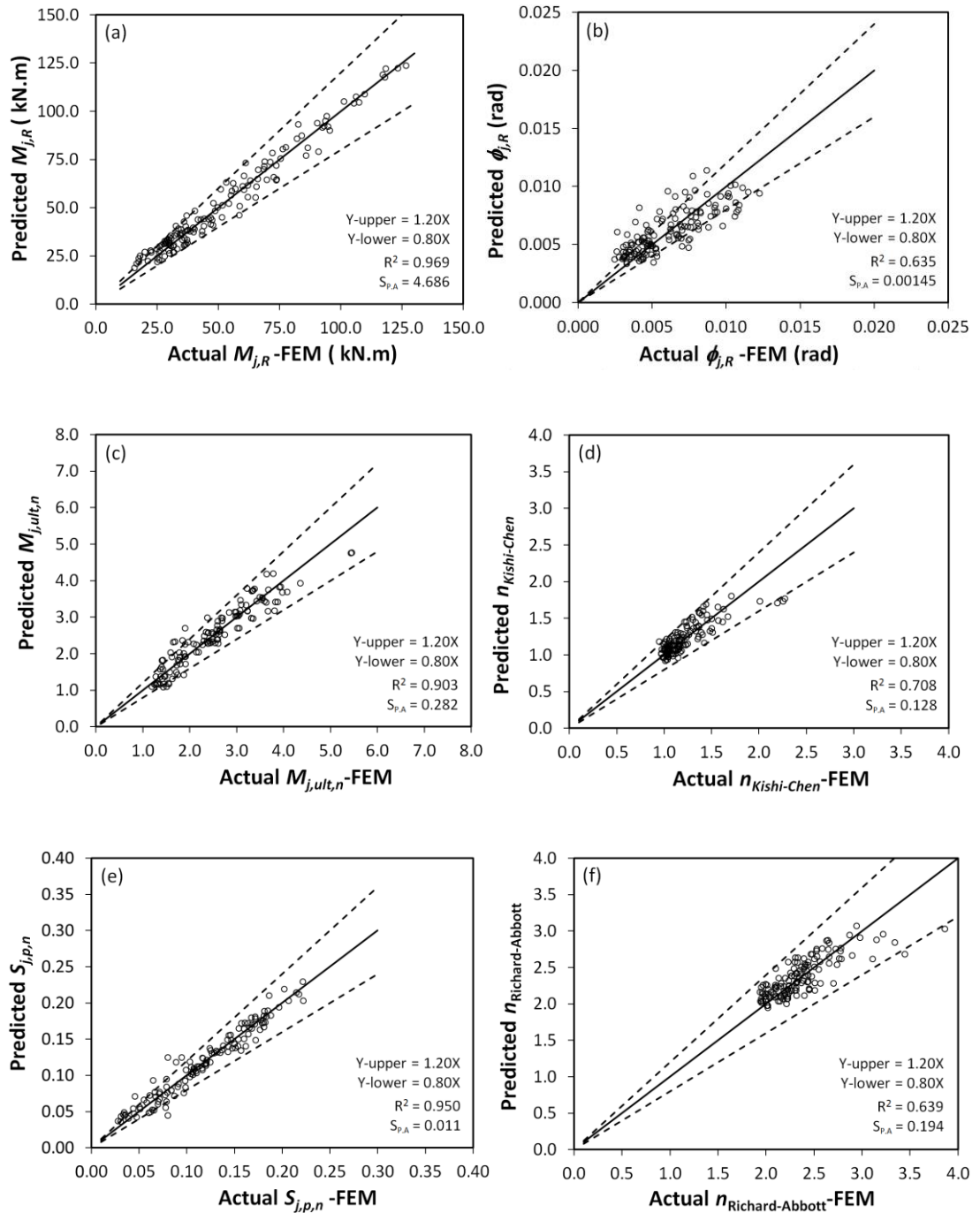


Figure 40: Comparison of analytical and predictive functions: (a) $M_{j,R}$, (b) $\phi_{j,R}$, (c) $M_{j,ult,n}$, (d) n for Kishi-Chen model, (e) $S_{j,p,n}$ and (f) n for Richard-Abbott model

Equations 17, 19 and 21 show very good predications as the R^2 values were close to unity (Figure 40 (a), (c) and (e)). On the other hand, the coefficient of determination of Eq. (18) was $R^2 = 0.635$ (Figure 40 (b)) since the rotation corresponding to plastic flexural resistance of the joint, $\phi_{j,R}$, is a very sensitive parameter. Even for, presumably, identical connections, experimental results of $\phi_{j,R}$ may vary considerably depending on the loading technique and material differences. Therefore, this correlation factor was deemed acceptable. The poor distribution of $\phi_{j,R}$ affects the normalized shape parameters, $n_{Kishi-Chen}$ and $n_{Richard-Abbott}$, for which the coefficient of determination was also relatively low.

6.3.4 Comparison between Numerical $M-\phi$ Curves and the Model Suggested by Eurocode-3

The suitability of model suggested by *Eurocode 3-(revised) Annex J* (CEN, 1997) and mentioned in section 6.2.5, with shape factor value of 2.7, was examined with the dimensionless forms of numerically measured moment-rotation curves of Figure 37. The design moment resistance of the joint, $M_{j,Rd}$, is evaluated by means of the secant rotation, S_j , which is equal to one-third of the initial stiffness. The results of this comparison shows that the suggested formulation of Eurocode 3-(revised) Annex J leads to satisfactory agreement with the numerical $M-\phi$ curves in 53 out of the 140 cases and significant overestimation of the knee region behaviour in 87 out of the 140 cases. Figure 39 illustrates part of this comparison for three RCC with, low, medium and high initial stiffness selected from each set. It should be noted that the variation in the knee region occurs for RCC with low initial stiffness which in turn resulted in higher design moment resistance of the joint, $M_{j,Rd}$. Therefore, there is need for further investigation to describe the behaviour of RCC, particularly for the

knee region, in order to codify the equation for the secant rotation, S_j , which correspond to $M_{j,Rd}$.

Chapter 7

CONCLUSION AND RECOMMENDATIONS FOR FUTURE WORK

7.1 Summary

The significance of this parametric study initiates from the need for further understanding of the behaviour of semi-rigid/partial-strength I-beam to tubular column connections. This research attempted to gain a qualitative understanding of the influence of the geometrical configurations of reverse channel connections (RCC) on the moment-rotation ($M-\phi$) response. These geometric parameters include; the thickness of flush end-plate, the wall thickness of reverse channel cut from hot-rolled square hollow sections (SHS), the ratio of flush end-plate thickness to the wall thickness of reverse channel, the width of hot-rolled reverse channels, the ratio of reverse channel depth to SHS width for different types of channel, the nominal bolt diameter and the gage distance. Furthermore, this study reported the possible achievements on moment-rotation ($M-\phi$) characteristics of reverse channel flush end-plate connections (RCC) by using HSS reverse channel under monotonic loading. It also introduced a double reverse channel connection (DRCC), where the reverse channel is split into two pieces, by leaving a gap in between, for better access to bolts. On the other hand, a standardized moment-rotation functions for reverse channel flush end-plate connection (RCC) were developed for the purposes of either predicting the RCC behavior or incorporating the behavior into a frame analysis computer program.

ABAQUS (v.6.12) software was used to develop three-dimensional (3-D) FE models for 200 specimens. The FE models developed were validated against the experimental results available from literature where 268 FE models were used for sensitivity analysis. The main emphasis of this research was on the stiffness, strength, sources of deformability, rotational capacity and failure mechanisms of the RCC.

7.2 Conclusion

Based on the results of this study, the following are the conclusions:

1. RCC joint is subjected to large rotation and deformation and the contacts between components are complicated which generate numerical convergence difficulties. Therefore, the use of explicit dynamic solver, implemented by ABAQUS, to analyze the behaviour of RCC joints can be considered as an efficient tool. For verification of finite element simulations, attention should be paid to loading duration in order to ensure a quasi-static response, the mesh size and the friction coefficient. In addition, the failure mode and the main characteristics, which define the moment-rotation ($M-\phi$) relationship, such as, the initial stiffness, the ultimate flexural resistance and the rotational capacity have to be in good agreement with the experiments.
2. The ultimate flexural resistance and the initial stiffness of RCC joint increase with the flush end-plate thickness while the rotational capacity dramatically decrease.
3. The ratio of wall thickness of channel to the thickness of flush end-plate is the

key for the rotational capacity of RCC connection. It is recommended to keep this ratio equal to 1.0 in order to achieve sufficient ductility.

4. For the same configuration of RCC, as the width of reverse channel increase the rotational capacity will also notably increase.
5. The ratio of channel depth to SHS width controls the deformability of the column face and also the rotational capacity of RCC connection. The deformations of the face of SHS columns became more severe with decrease in the ratio of channel depth to SHS width to less than 0.72. Therefore, the minimum value of this ratio is recommended to be kept equal to 0.72 in order to prevent the excessive deformation of the column face.
6. Having achieved high stiffness, strength, rotational capacity and ductility, the RCC had proven itself as a robust connection, particularly in terms of rotational capacity and ductility. All tests were able to achieve a rotational capacity beyond the minimum 0.03 rad, which is considered sufficient for full plastic design. In most cases it achieved a rotation of more than 0.06 rad and in one case 0.16 rad.
7. The failure of RCC can occur at the reverse channel, bolt or flush end plate. The key for the failure of RCC was the ratio of wall thickness of channel to the thickness of flush end-plate (t_{wc}/t_p). For RCC with beam serial size of up to UKB406x176 the t_{wc}/t_p ratio was up to 0.542 and the failure observed at reverse channel. When HSS (S690) reverse channel was used as part of the joint, this lead to remarkable increase in both ultimate flexural resistance and

the rotational capacity, without compromise to the initial stiffness. Consequently, the reverse channel and flush end plate experienced large deformations and they controlled the failure of the connection.

8. DRCC was introduced instead of RCC with the intention of providing better access for tightening bolts, particularly when deep beams are connected to reverse channel. Two tension bolts flush end plate connection was used throughout this study hence the beam depth was limited to serial size UKB533x210. The results indicate that for the DRCC using beams of up to UKB406x176 size had produced less ultimate flexural resistance and very similar initial stiffness and deformation capacity when compared to those of RCC.
9. The use of DRCC with HSS (S690) reverse channel, as opposed to RCC, resulted in increase in ultimate flexural resistance and rotational capacity of up to 38.7% and 53.1% respectively, without compromise to the initial stiffness.
10. As the clear distance between the split reverse channels (h) increased the deformation of DRCC also increased. This can be observed from the change in the knee and post yield zone in moment-rotation ($M-\phi$) response. Therefore, it is recommended that h should be kept at a minimum 20% of the beam depth, as considered in this study, and at the same time h should be practically adequate for bolt accessibility.
11. Among the currently available functions, the Kishi-Chen and Richard-Abbott

models are proved appropriate for fitting experimental moment-rotation data for RCC. The two functions were successfully used in this parametric study to express the $M-\phi$ relationships for 140 specimens, where the analytical and predicted data are in very good agreement. Comparisons were presented between the fitted functions and the results indicated that the Richard-Abbott function, in dimensionless form, provides more accuracy than Kishi-Chen function.

12. With the aim of examining the suitability of the representation of moment-rotation curve suggested by Eurocode 3 in its Annex J for RCC, the comparison of this model with numerical $M-\phi$ curves illustrated a significant overestimation of the knee region behaviour for most of the cases, particularly for RCC with low initial stiffness.

7.2 Recommendations for Future Work

This thesis was step towards establishing the requirements for the design of semi-rigid/partial-strength I-beam to tubular column connections and it was also trying to contribute to the development of a simple and accurate moment-rotation ($M-\phi$) relationship for the purpose of structural design and elastic-plastic analysis. Following the above concluding remarks the author would like to highlight the fact that more research is needed towards for:

- Investigating the behaviour of RCC and DRCC under cyclic loading, since the outcomes indicate that these types of connections have good potential to achieve sufficient strength and ductility.

- Examining the behaviour of RCC and DRCC with beams deeper than the ones considered in this study. So that a more general approach for the design guidelines of RCC and DRCC can be established.
- Developing moment-rotation ($M-\phi$) model for RCC by considering the effects of different steel grades for the purpose of structural design and elastic-plastic analysis.
- Examining the suitability of the representation of moment-rotation curve suggested by Eurocode 3 in its Annex J for RCC in order to codify the equation for the secant rotation, S_j , corresponding to $M_{j,Rd}$.

REFERENCES

- ABAQUS. (2012). *standard user's manual: Vol. 1, 2 and 3; version 6.12*. USA: Hibbitt, Karlsson and Sorensen, Inc.
- Abolmaali, A., Matthys, J. H., Farooqi, M., & Choi, Y. (2005). Development of moment–rotation model equations for flush end-plate connections. *Journal of Constructional Steel Research*, 61, 1595–1612.
- AIJ. (1997). *Full-scale test on plastic rotation capacity of steel wide-flange beams connected with square tube steel columns*. Tokyo: Kinki Branch, Architectural Institute of Japan.
- AISC. (1997). *Hollow structural sections connections manual*. Chicago, Ill., USA: American Institute of Steel.
- AlHendi, H., & Celikag, M. (2015). Parametric study on moment-rotation characteristics of reverse channel connections to tubular columns. *Journal of Constructional Steel Research*, 104, 261–273.
- Altman, W. G., Azizinamini, A., Bradburn, J. H., & Radziminski, J. B. (1982). *Moment–rotation characteristics of semi-rigid steel beam–column connections*. Civil Engineering Department, University of South Carolina.
- Anderson, J. C., & Linderman, R. R. (1991). *Steel beam to box column connections*. Department of Civil Engineering. University of Southern California.

- Ang, K. M., & Morris, G. A. (1984). Analysis of three-dimensional frames with flexible beam–column connections. *Canadian Journal of Civil Engineering*, 2, 245-254.
- ASCE. (2000). *State of the art report on connection performance (FEMA 355D)*. Reston, Va.; Washington, D.C.: American Society of Civil Engineers.
- Attigbe, G., & Morris, G. (1991). Moment–rotation functions for steel connections. *Journal of Structural Engineering*, 117, 1703–1718.
- Bahaari, M. R., & Sherbourne, A. N. (1997). Finite element prediction of end plate bolted connection behavior. II: analytic formulation. *Journal of Structural Engineering*, 123(2).
- Ban, H., & Bradford, M. A. (2013). Flexural behaviour of composite beams with high strength steel. *Engineering Structures*, 56, 1130–1141.
- Ban, H., Shi, G., Shi, Y., & Bradford, M. A. (2013). Experimental investigation of the overall buckling behaviour of 960 MPa high strength steel columns. *Journal of Constructional Steel Research*, 88, 256–266.
- Ban, H., Shi, G., Shi, Y., & Wang, Y. (2012). Overall buckling behavior of 460 MPa high strength steel columns: Experimental investigation and design method. *Journal of Constructional Steel Research*, 74, 140–150.

- Bose, S. K., McNeice, G. M., & Sherbourne, A. N. (1972). Column webs in steel beam to column connexions. Part I: formulation and verification. *Computers & Structures*, 2, 253–72.
- British Steel. (1997). *SHS jointing - flowdrill & hollo-bolt*. British Steel Tubes and Pipes.
- CEN. (1993). *Eurocode 3: Design of steel structures - Part 1-8: Design of joints; BS EN 1993-1-8;2005*. Londen: UK: British Standered Institution.
- CEN. (1997). *Eurocode 3 - Part 1-1 Revised Annex J: Joint in Building Frame*. Londen: European Committee for Standardization.
- CEN. (2005). *Eurocode 3: Design of steel structures - Part 1-1: General rules and rules for buldings; BS EN 1993-1-1*. Londen: UK: British Standered Institution.
- CEN. (2005). *Eurocode 3: Design of steel structures - Part 1-8: Design of joints; BS EN 1993-1-8*. Londen: UK: British Standered Institution.
- Chan, S., & Chui, P. (2000). *Non-Linear Static and Cyclic Analysis of Steel Frames with Semi-Rigid Connections*. Oxford: Elsevier.
- Chasten, C. P., Lu, L. W., & Driscoll, G. C. (1992). Prying and shear in end-plate connection design. *Journal of Structural Engineering*, 5(118), 1295–1311.

- Chen, W. F., & Kishi, N. (1989). Semi-rigid steel beam-to-column connections: data base and modeling. *Journal of Structural Engineering*, 115(1), 23104.
- Chen, W. F., Kishi, N., & Komuro, M. (2011). *Semi-rigid connections handbook*. J. Ross Publishing, Incorporated.
- Chisala, M. L. (1999). Modelling M–f curves for standard beam-to-column connections. *Engineering Structures*, 1066–1075.
- Chmielowiec, M., & Richard, R. M. (1987). *Moment–rotation curves for partially restrained steel connections*. Report to AISC. University of Arizona.
- Citipitioglu, A. M., Haj-Ali, R. M., & White, D. W. (2002). Refined 3D finite element modeling of partially-restrained connections including slip. *Journal of Constructional Steel Research*, 58, 995–1013.
- Coelho, A. M., & Bijlaard, F. S. (2007). Experimental behaviour of high strength steel end-plate connections. *Journal of Constructional Steel Research*, 63, 1228–1240.
- Coelho, A. M., Bijlaard, F. S., & Kolstein, H. (2009). Experimental behaviour of high-strength steel web shear panels. *Engineering Structures*, 31, 1543-1555.
- Coelho, A. M., Bijlaard, F. S., & Silva, L. S. (2004). Experimental assessment of the ductility of extended end plate connections. *Engineering Structures*, 26, 1185–1206.

- De Stefano, M., & Astaneh, A. (1991). Axial force–displacement behavior of steel double angles. *Journal of Constructional Steel Research*, 20(3), 161–181.
- Díaz, C., Martí, P., Victoria, M., & Querin, O. M. (2011). Review on the modelling of joint behaviour in steel frames. *Journal of Constructional Steel Research*, 67, 741–758.
- Díaz, C., Victoria, M., Martí, P., & Querin, O. M. (2011). FE model of beam-to-column extended end-plate joints. *Journal of Constructional Steel Research*, 67, 1578–1590.
- Ding, J., & Wang, Y. C. (2007). Experimental study of structural fire behaviour of steel beam to concrete filled tubular column assemblies with different types of joints. *Engineering Structures*, 29, 3485–3502.
- Elghazouli, A. Y., Málaga-Chuquitaype, C., Castro, J. M., & Orton, A. H. (2009). Experimental monotonic and cyclic behaviour of blind-bolted angle connections. *Engineering Structures*, 31, 2540–2553.
- Elsawaf, S., & Wang, Y. C. (2012). Methods of improving the survival temperature in fire of steel beam connected to CFT column using reverse channel connection. *Engineering Structures*, 34, 132–146.
- Elsawaf, S., & Wang, Y. C. (2013). Behaviour of restrained structural subassemblies of steel beam to CFT column in fire during cooling stage. *Engineering Structures*, 46, 471–492.

- Elsawaf, S., Wang, Y. C., & Mandal, P. (2011). Numerical modelling of restrained structural subassemblies of steel beam and CFT columns connected using reverse channels in fire. *Engineering Structures*, 33, 1217–1231.
- Faella, C., Piluso, V., & Rizzano, G. (1997). A new method to design extended end plate connections and semirigid braced frames. *Journal of Constructional Steel Research*, 1(41), 61–91.
- Faella, C., Piluso, V., & Rizzano, G. (2000). *Structural Steel Semirigid Connections*. Florida: CRC Press LLC.
- France, J. E., Davison, B., & Kirby, P. A. (1999). Strength and rotational stiffness of simple connections to tubular columns using flowdrill connectors. *Journal of Constructional Steel Research*, 50, 15–34.
- France, J. E., Davison, J. B., & Kirby, P. A. (1999a). Strength and rotational response of moment connections to tubular columns using flowdrill connectors. *Journal of Constructional Steel Research*, 50, 1–14.
- Frye, M. J., & Morris, G. A. (1975). Analysis of flexibly connected steel frames. *Canadian Journal of Civil Engineering* 1975, 2(3), 280–91.
- Gao, L., Sun, H., Jin, F., & Fan, H. (2009). Load-carrying capacity of high-strength steel box-sections I: Stub columns. *Journal of Constructional Steel Research*, 65, 918-924.

- Gebbeken, N., Rothert, H., & Binder, B. (1994). On the numerical analysis of endplate connections. *Journal of Constructional Steel Research*, 2(30), 177–196.
- Gerardy, J. C., & Schleich, J. B. (1991). *Semi-rigid action in steel frame structures*. Luxembourg: Arbed Recherches; Report no.7210-SAI507.
- Girao Coelho, A. M., & Bijlaard, F. S. (2007). Experimental behaviour of high strength steel end-plate connections. *Journal of Constructional Steel Research*, 63, 1228–1240.
- Gong, Y. (2008). Double-angle shear connections with small hollow structural. *Journal of Constructional Steel Research*, 64, 539–549.
- Gong, Y., & Gillies, A. (2008). Double-angle shear connections with short outstanding legs. . *Canadian Journal of Civil Engineering*, 35(8), 786-795.
- Gorenc, B., Tinyou , R., & Syam, A. (2005). *Steel Designers' Handbook*. Sydney NSW: University of New South Wales Press Ltd.
- Goverdhan, A. V. (1984). *A collection of experimental moment–rotation curves and valuation of prediction equations for semi-rigid connections*. Master thesis.Nashville (TN): Vanderbilt University.

- Guravich , S., & Dawe, J. (1998). Bolted double angle connections in combined shear and tension. *AISC National Steel Construction Congress* (pp. 8/1–8/15). Chicago: American Institute of Steel Construction.
- Hadianfard, M. A. (2003). Effects of semi-rigid behaviour of connections in the reliability of steel frames. *Structural Safety*, 2(25), 123–38.
- Hayalioglu MS, M. S. (2005). Minimum cost design of steel frames with semi-rigid connections and column bases via genetic optimization. *Computers & Structures*, 83(21-22), 1849–1863.
- Hedayat, A. A., & Celikag, M. (2009). Post-Northridge connection with modified beam end configuration to enhance strength and ductility. *Journal of Constructional Steel Research*, 65, 1413-1430.
- Hong, K., Yang, J. G., & Lee, S. K. (2001). Parametric study of double angle framing connections subjected to shear and tension. *Journal of Constructional Steel Research*, 57, 997–1013.
- Hong, K., Yang, J. G., & Lee, S. K. (2002). Moment–rotation behavior of double angle connections subjected to shear load. *Engineering Structures* 24 (2002), 24, 125–132.
- Huang , S., Davison, B., & Burgess, I. W. (2013). High-temperature tests on joints to steel and partially-encased H-section columns. *Journal of Constructional Steel Research* , 80, 243–251.

- Huang, S., Davison, B., & Burgess, I. W. (2013a). Experiments on reverse-channel connections at elevated temperatures. *Engineering Structures*, 49, 973–982.
- Jarmai, K., & Farkas, J. (1998). *Mechanics and design of tubular structures*. New York: Springer Science & Business Media.
- Kameshki, E. S., & Saka, M. P. (2001). Optimum design of nonlinear steel frames with semirigid connections using a genetic algorithm. *Computers & Structures* 2001(79), 1593–604.
- Kennedy, D. R., & Hafez, M. (1984). A study of end-plate connections for steel beams. *Canadian Journal of Civil Engineering*, 2(11), 139–49.
- Keshavarzi, F., Mirghaderi, R., Imanpour, A., & Khafaf, B. (2008). Numerical evaluation of through plate beam to box column connection. *Structures Congress 2008* (pp. 1-10). Vancouver, British Columbia, Canada: American Society of Civil Engineers.
- Kishi, N., & Chen, W. F. (1986). *Steel connection data bank program*. West Lafayette: School of Civil Engineering, Purdue University, Report no. CE-STR86-18.
- Kishi, N., & Chen, W. F. (1987). Moment-rotation relations of semirigid connections with angles. *Journal of Structural Engineering*, 116(7), 24833.

- Korol, R. M., Ghobarah, A., & Mourad, S. (1993). Blind bolting W-shape beams to HSS columns. *Journal of Structural Engineering*, *119*, 3463-3481.
- Kosteski, N., & Packer, J. A. (2003). Longitudinal plate and through plate-to-hollow structural section welded connections. *Journal of Structural Engineering*, *129*(4), 478–486.
- Krishnamurthy, N. (1978). Fresh look at bolted end-plate behaviour and design. *Engineering Journal 1978.*, *2*(15), 39–49.
- Krishnamurthy, N. (1978a). *Analytical investigation of bolted stiffened tee-stubs*. Nashville (TN): Department of Civil Engineering, Vanderbilt University.
- Krishnamurthy, N., & Graddy, D. E. (1976). Correlation between 2- and 3-dimensional finite element analysis of steel bolted end-plate connections. *Computers & Structures*, *4-5*(6), 381–389.
- Krishnamurthy, N., Huang, H., Jeffrey, P. K., & Avery, L. K. (1979). Analytical M- ϕ curves for end-plate connections. *Journal of the Structural Division*, *105*, 133–145.
- Kukreti, A. R., Ghassemieh, M., & Murray, T. M. (1990). Behavior and design of large-capacity moment end plates. *Journal of Structural Engineering*, *116*, 809-828.

- Kukreti, A. R., Murray, T. M., & Abolmaali, A. (1987). End-plate connection moment–rotation relationship. *Journal of Constructional Steel Research*, 8, 137–157.
- Kurobane, Y., Packer, J., Wardenier, J., & Yeomans, N. (2004). *Design guide for structural hollow section column connections*. In: Serie CIDECT construction with hollow sections: Germany: TUV-Verlag.
- Liu, Y., Málaga-Chuquitaype, C., & Elghazouli, A. Y. (2012). Response and component characterisation of semi-rigid connections to tubular columns under axial loads. *Engineering Structures*, 41, 510–532.
- Liu, Y., Málaga-Chuquitaype, C., & Elghazouli, A. Y. (2012a). Behaviour of beam-to-tubular column angle connections under shear loads. *Engineering Structures*, 42, 434–456.
- Málaga-Chuquitaype, C., & Elghazouli, A. Y. (2010). Component-based mechanical models for blind-bolted angle connections. *Engineering Structures*, 32, 3048–3067.
- Málaga-Chuquitaype, C., & Elghazouli, A. Y. (2010a). Behaviour of combined channel/angle connections to tubular columns under monotonic and cyclic loading. *Engineering Structures*, 32, 1600–1616.

- McMullin , K. M., & Astaneh , A. (1988). *Analytical and experimental studies of double-angle framing connections*. Report no. UCB/SEMM-88/14. Berkeley: Dept. of Civ. Eng., University of California.
- Mirghaderi, S. R., Torabian, S., & Keshavarzi, F. (2010). I-beam to box-column connection by a vertical plate passing through the column. *Engineering Structures*, 32, 2034-2048.
- Mohamadi-Shoore, M. R., & Mofid, M. (2011). New modeling for moment–rotation behavior of bolted endplate connections. *Scientia Iranica*, 827–834.
- Mohamadi-shooreh, M. R., & Mofid, M. (2008). Parametric analyses on the initial stiffness of flush end-plate splice connections using FEM. *Journal of Constructional Steel Research* , 64, 1129–1141.
- Nakashima, M., Roeder, C. W., & Maruoka, Y. (2000). Steel moment frames for earthquakes in United States and Japan. *Journal of Constructional Steel Research*, 126(8), 861-868.
- Nethercot, D. A. (1985). *Steel beam-to-column connections: a review of test data and its applicability to the evaluation of joint behaviour in the performance of steel frames*. CIRIA report, RP338.
- Picard, A., Giroux, Y. M., & Brun, P. (1976). Discussion of analysis of flexibly connected steel frame. *Canadian Journal of Civil Engineering*, 3(2), 350–352.

- Prabha , P., Marimuthu, V., Saravanan, M., & Jayachandran, S. (2010). Evaluation of connection flexibility in cold formed steel racks. *Journal of Constructional Steel Research*, 7(66), 863–872.
- Pucinotti, R. (2001). Top-and-seat and web angle connections: prediction via mechanical model. *Journal of Constructional Steel Research*, 57, 661–94.
- Qiang, X., Bijlaard, F. S., Kolstein, H., & Jiang, X. (2014). Behaviour of beam-to-column high strength steel endplate connections under fire conditions – Part 2: Numerical study. *Engineering Structures*, 64, 39–51.
- Qiang, X., Bijlaard, F. S., Kolstein, H., & Jiang, X. (2014a). Behaviour of beam-to-column high strength steel endplate connections under fire conditions – Part 1: Experimental study. *Engineering Structures*, 64, 23–38.
- Richard, R. M., & Abbott, B. J. (1975). Versatile elastic–plastic stress–strain formula. *Journal of the Engineering Mechanics Division, ASCE*, 4(101), 511–515.
- SAC. (1996). *Experimental investigations of beam-column sub assemblages*. Sacramento, CA.: Report SAC-96-01, Parts 1 and 2, SAC Joint Venture.
- Scawthorn, C., & Yanev, P. I. (1995). Preliminary report 17 January 1995, Hyogo-ken Nambu, Japanese earthquake. *Engineering Structures*, 17(3), 146-157.

- Sherbourne, A. N., & Bahaari, M. R. (1996). 3D simulation of end-plate bolted connections. *Journal of Structural Engineering*, *11*(120), 3122–3136.
- Sherman, D. R. (1995). Simple framing connections to HSS columns. *Proc. National Steel Construction Conference* (pp. 30.1 – 30.16). San Antonio, Tex., USA: American Institute of Steel Construction.
- Shi, G., Ban, H., & Bijlaard, F. S. (2012). Tests and numerical study of ultra-high strength steel columns with end restraints. *Journal of Constructional Steel Research*, *70*, 236–247.
- Simões da Silva, L., & Girão Coelho, A. M. (2001). An analytical evaluation of the response of steel joints under bending and axial force. *Computers & Structures*, *79*, 873–881.
- Sommer, W. H. (1969). *Behaviour of welded header plate connections*. Toronto, Canada: Master thesis presented to the University of Toronto.
- Troup, S., Xiao, R. Y., & Moy, S. J. (1998). Numerical modeling of bolted steel connections. *Journal of Constructional Steel Research*, *1*(46), 269.
- Urbonas, K., & Daniunas, A. (2006). Behaviour of semi-rigid steel beam-to-beam joints under bending and axial forces. *Journal of Constructional Steel Research*, *62*, 1244–1249.

- Wales, M. W., & Rossow, E. C. (1983). Coupled moment-axial force behaviour in bolted joint. *Journal of Structural Engineering* 1983;109, 5(109), 1250–1266.
- Wang, Y. C., & Xue, L. (2013). Experimental study of moment–rotation characteristics of reverse channel connections to tubular columns. *Journal of Constructional Steel Research* , 85, 92-104.
- Wang, Y.-B., Li, G.-Q., Su-Wen, C., & Fei-Fei, S. (2014). Experimental and numerical study on the behavior of axially compressed high strength steel box-columns. *Engineering Structures*, 58, 79–91.
- Weynand, K. (1992). SERICON I — databank on joints building frames. *COST C1 first state of the art workshop on semi-rigid behaviour of civil engineering structures*, (pp. 463–474).
- White, R. N., & Fang, P. J. (1966). Framing connections for square structural tubing. *Journal of the Structural Division*, 92(2), 175-194.
- Wilkinson, S., Hurdman, G., & Crowther, A. (2006). A moment resisting connection for earthquake resistant structures. *Journal of Constructional Steel Research*, 62, 295–302.
- Wu, F. S., & Chen, W. F. (1990). A design model for semi-rigid connections. *Engineering Structures*, 2(12), 88–97.

- Xue, L. (2012). *Moment-rotation behaviour of universal beam to tubular column connections using reverse channel*. Manchester: PhD thesis, School of Mechanical, Aerospace and Civil Engineering, University of Manchester.
- Yang, J. -G., Murray, T. M., & Plaut, R. H. (2000). Three-dimensional finite element analysis of double angle connections under tension and shear. *Journal of Constructional Steel Research*, 54, 227–244.
- Yang, W. H., Bowman, M. D., & Chen, W. F. (1999). Experimental study on bolted unstiffened seat angle connections. *Journal of Structural Engineering*, 125, 1224-1231.
- Yee, Y. L., & Melchers, R. E. (1985). Moment-rotation curves for bolted connections. *Journal of Structural Engineering*, 112(3), 20449.
- Yu, H., Burgess, I. W., Davison, J. B., & Plank, R. J. (2008). Numerical simulation of bolted steel connections in fire using explicit dynamic analysis. *Journal of Constructional Steel Research*, 64, 515–525.

APPENDICES

Appendix A: Schedule of RCC Dimensions, main parameters of the $M-\phi$ curves and the observed failure modes

Table A.1: Schedule of RCC dimensions of Set1 in the parametric study

Set No.	d_{bolt}	Specimen	Column Section (S355)	Beam Section (S355)	Channel						Endplate				
					Section	h_c	w_c	m	t_{fc}	t_{wc}	h_p	w_p	t_p	p_f	g
Set1	20	S27B	SHS250 × 10	UKB457 × 191 × 106	cut from SHS250 × 12.5	513.2	250.0	100.0	12.5	12.5	513.2	238.0	22.0	50.0	140.0
		S28B	SHS260 × 10	UKB457 × 191 × 106	UKPFC260 × 90 × 35	513.2	260.0	90.0	14.0	8.0	513.2	238.0	22.0	60.0	140.0
		S29B	SHS250 × 10	UKB457 × 191 × 106	cut from SHS250 × 10	519.2	250.0	120.0	10.0	10.0	519.2	244.0	25.0	80.0	120.0
		S30B	SHS260 × 10	UKB457 × 191 × 106	UKPFC260 × 75 × 28	519.2	260.0	75.0	12.0	7.0	519.2	244.0	25.0	100.0	120.0
		S31	SHS250 × 10	UKB457 × 191 × 106	cut from SHS250 × 12.5	513.2	250.0	100.0	12.5	12.5	513.2	238.0	22.0	50.0	120.0
		S32	SHS260 × 10	UKB457 × 191 × 106	UKPFC260 × 90 × 35	513.2	260.0	90.0	14.0	8.0	513.2	238.0	22.0	60.0	100.0
		S33	SHS250 × 10	UKB457 × 191 × 106	cut from SHS250 × 10	519.2	250.0	120.0	10.0	10.0	519.2	244.0	25.0	80.0	100.0
		S34	SHS250 × 10	UKB457 × 191 × 106	cut from SHS250 × 12.5	513.2	250.0	100.0	12.5	12.5	513.2	238.0	22.0	50.0	100.0
	S35	SHS260 × 10	UKB457 × 191 × 106	UKPFC260 × 75 × 28	519.2	260.0	75.0	12.0	7.0	519.2	244.0	25.0	100.0	90.0	
	S36	SHS260 × 10	UKB457 × 191 × 106	UKPFC260 × 90 × 35	513.2	260.0	90.0	14.0	8.0	513.2	238.0	22.0	60.0	90.0	
	S37	SHS250 × 10	UKB457 × 191 × 106	cut from SHS250 × 12.5	513.2	250.0	100.0	12.5	12.5	513.2	238.0	22.0	50.0	140.0	
	S38	SHS260 × 10	UKB457 × 191 × 106	UKPFC260 × 90 × 35	513.2	260.0	90.0	14.0	8.0	513.2	238.0	22.0	60.0	140.0	
	S39	SHS250 × 10	UKB457 × 191 × 106	cut from SHS250 × 10	519.2	250.0	120.0	10.0	10.0	519.2	244.0	25.0	80.0	120.0	
	S40	SHS260 × 10	UKB457 × 191 × 106	UKPFC260 × 75 × 28	519.2	260.0	75.0	12.0	7.0	519.2	244.0	25.0	100.0	120.0	
	S41	SHS250 × 10	UKB457 × 191 × 106	cut from SHS250 × 12.5	513.2	250.0	100.0	12.5	12.5	513.2	238.0	22.0	50.0	120.0	
	S42	SHS260 × 10	UKB457 × 191 × 106	UKPFC260 × 90 × 35	513.2	260.0	90.0	14.0	8.0	513.2	238.0	22.0	60.0	100.0	
S43	SHS250 × 10	UKB457 × 191 × 106	cut from SHS250 × 10	519.2	250.0	120.0	10.0	10.0	519.2	244.0	25.0	80.0	100.0		
S44	SHS250 × 10	UKB457 × 191 × 106	cut from SHS250 × 12.5	513.2	250.0	100.0	12.5	12.5	513.2	238.0	22.0	50.0	100.0		
S45	SHS260 × 10	UKB457 × 191 × 106	UKPFC260 × 75 × 28	519.2	260.0	75.0	12.0	7.0	519.2	244.0	25.0	100.0	90.0		
S46	SHS260 × 10	UKB457 × 191 × 106	UKPFC260 × 90 × 35	513.2	260.0	90.0	14.0	8.0	513.2	238.0	22.0	60.0	90.0		
24	S47	SHS250 × 10	UKB457 × 191 × 106	cut from SHS250 × 12.5	513.2	250.0	100.0	12.5	12.5	513.2	238.0	22.0	50.0	140.0	
	S48	SHS260 × 10	UKB457 × 191 × 106	UKPFC260 × 90 × 35	513.2	260.0	90.0	14.0	8.0	513.2	238.0	22.0	60.0	140.0	
	S49	SHS250 × 10	UKB457 × 191 × 106	cut from SHS250 × 10	519.2	250.0	120.0	10.0	10.0	519.2	244.0	25.0	80.0	140.0	
	S50	SHS250 × 10	UKB457 × 191 × 106	cut from SHS250 × 10	519.2	250.0	120.0	10.0	10.0	519.2	244.0	25.0	80.0	120.0	
	S51	SHS260 × 10	UKB457 × 191 × 106	UKPFC260 × 75 × 28	519.2	260.0	75.0	12.0	7.0	519.2	244.0	25.0	100.0	120.0	
	S52	SHS250 × 10	UKB457 × 191 × 106	cut from SHS250 × 12.5	513.2	250.0	100.0	12.5	12.5	513.2	238.0	22.0	50.0	120.0	
	S53	SHS260 × 10	UKB457 × 191 × 106	UKPFC260 × 90 × 35	513.2	260.0	90.0	14.0	8.0	513.2	238.0	22.0	60.0	100.0	
	S54	SHS250 × 10	UKB457 × 191 × 106	cut from SHS250 × 10	519.2	250.0	120.0	10.0	10.0	519.2	244.0	25.0	80.0	100.0	
	S55	SHS250 × 10	UKB457 × 191 × 106	cut from SHS250 × 12.5	513.2	250.0	100.0	12.5	12.5	513.2	238.0	22.0	50.0	100.0	
	S56	SHS260 × 10	UKB457 × 191 × 106	UKPFC260 × 75 × 28	519.2	260.0	75.0	12.0	7.0	519.2	244.0	25.0	100.0	100.0	

Table A.2: Schedule of RCC dimensions of Set2 in the parametric study

Set No.	d _{bolt}	Specimen	Column Section (S355)	Beam Section (S355)	Channel						Endplate				
					Section	h _c	w _c	m	t _{fc}	t _{wc}	h _p	w _p	t _p	p _f	g
Set2	20	S57	SHS250 × 10	UKB406 x 178 x 60	UKPFC230 x 90 x 32	442.4	230.0	90.0	14.0	7.5	442.4	213.9	18.0	50.0	120.0
		S58	SHS250 × 10	UKB406 x 178 x 60	UKPFC230 x 75 x 26	446.4	230.0	75.0	12.5	6.5	446.4	217.9	20.0	60.0	120.0
		S59	SHS250 × 10	UKB406 x 178 x 60	UKPFC230 x 75 x 26	450.4	230.0	75.0	12.5	6.5	450.4	221.9	22.0	80.0	120.0
		S60	SHS250 × 10	UKB406 x 178 x 60	UKPFC230 x 90 x 32	450.4	230.0	90.0	14.0	7.5	450.4	221.9	22.0	80.0	100.0
		S61	SHS250 × 10	UKB406 x 178 x 60	UKPFC230 x 75 x 26	446.4	230.0	75.0	12.5	6.5	446.4	217.9	20.0	60.0	100.0
		S62	SHS250 × 10	UKB406 x 178 x 60	UKPFC230 x 90 x 32	442.4	230.0	90.0	14.0	7.5	442.4	213.9	18.0	50.0	100.0
		S63	SHS250 × 10	UKB406 x 178 x 60	UKPFC230 x 75 x 26	456.4	230.0	75.0	12.5	6.5	456.4	227.9	25.0	100.0	90.0
		S64	SHS250 × 10	UKB406 x 178 x 60	UKPFC230 x 75 x 26	442.4	230.0	75.0	12.5	6.5	442.4	213.9	18.0	50.0	90.0
		S65	SHS250 × 10	UKB406 x 178 x 60	UKPFC230 x 90 x 32	450.4	230.0	90.0	14.0	7.5	450.4	221.9	22.0	80.0	90.0
		S66	SHS250 × 10	UKB406 x 178 x 60	UKPFC230 x 90 x 32	450.4	230.0	90.0	14.0	7.5	450.4	221.9	20.0	80.0	120.0
		S67	SHS250 × 10	UKB406 x 178 x 60	UKPFC230 x 90 x 32	442.4	230.0	90.0	14.0	7.5	442.4	213.9	18.0	50.0	100.0
		S68	SHS250 × 10	UKB406 x 178 x 60	UKPFC230 x 75 x 26	446.4	230.0	75.0	12.5	6.5	446.4	217.9	20.0	60.0	100.0
		S69	SHS250 × 10	UKB406 x 178 x 60	UKPFC230 x 75 x 26	450.4	230.0	75.0	12.5	6.5	450.4	221.9	22.0	80.0	100.0
		S70	SHS250 × 10	UKB406 x 178 x 60	UKPFC230 x 90 x 32	450.4	230.0	90.0	14.0	7.5	450.4	221.9	22.0	80.0	90.0
		S71	SHS250 × 10	UKB406 x 178 x 60	UKPFC230 x 75 x 26	446.4	230.0	75.0	12.5	6.5	446.4	217.9	20.0	60.0	90.0
		S72	SHS250 × 10	UKB406 x 178 x 60	UKPFC230 x 90 x 32	442.4	230.0	90.0	14.0	7.5	442.4	213.9	18.0	50.0	90.0
S73	SHS250 × 10	UKB406 x 178 x 60	UKPFC230 x 75 x 26	456.4	230.0	75.0	12.5	6.5	456.4	227.9	25.0	100.0	70.0		
S74	SHS250 × 10	UKB406 x 178 x 60	UKPFC230 x 75 x 26	442.4	230.0	75.0	12.5	6.5	442.4	213.9	18.0	50.0	70.0		
S75	SHS250 × 10	UKB406 x 178 x 60	UKPFC230 x 90 x 32	450.4	230.0	90.0	14.0	7.5	450.4	221.9	22.0	80.0	70.0		
S76	SHS250 × 10	UKB406 x 178 x 60	UKPFC230 x 90 x 32	450.4	230.0	90.0	14.0	7.5	450.4	221.9	20.0	80.0	70.0		
S77	SHS250 × 10	UKB406 x 178 x 60	UKPFC230 x 90 x 32	442.4	230.0	90.0	14.0	7.5	442.4	213.9	18.0	50.0	100.0		
S78	SHS250 × 10	UKB406 x 178 x 60	UKPFC230 x 75 x 26	446.4	230.0	75.0	12.5	6.5	446.4	217.9	20.0	60.0	100.0		
S79	SHS250 × 10	UKB406 x 178 x 60	UKPFC230 x 75 x 26	450.4	230.0	75.0	12.5	6.5	450.4	221.9	22.0	80.0	100.0		
S80	SHS250 × 10	UKB406 x 178 x 60	UKPFC230 x 90 x 32	450.4	230.0	90.0	14.0	7.5	450.4	221.9	22.0	80.0	90.0		
S81	SHS250 × 10	UKB406 x 178 x 60	UKPFC230 x 75 x 26	446.4	230.0	75.0	12.5	6.5	446.4	217.9	20.0	60.0	90.0		
S82	SHS250 × 10	UKB406 x 178 x 60	UKPFC230 x 90 x 32	442.4	230.0	90.0	14.0	7.5	442.4	213.9	18.0	50.0	90.0		
S83	SHS250 × 10	UKB406 x 178 x 60	UKPFC230 x 75 x 26	456.4	230.0	75.0	12.5	6.5	456.4	227.9	25.0	100.0	70.0		
S84	SHS250 × 10	UKB406 x 178 x 60	UKPFC230 x 75 x 26	442.4	230.0	75.0	12.5	6.5	442.4	213.9	18.0	50.0	70.0		
S85	SHS250 × 10	UKB406 x 178 x 60	UKPFC230 x 90 x 32	450.4	230.0	90.0	14.0	7.5	450.4	221.9	22.0	80.0	70.0		
S86	SHS250 × 10	UKB406 x 178 x 60	UKPFC230 x 90 x 32	450.4	230.0	90.0	14.0	7.5	450.4	221.9	20.0	80.0	70.0		

Table A.3: Schedule of RCC dimensions of Set3 in the parametric study

Set No.	d _{bolt}	Specimen	Column Section (S355)	Beam Section (S355)	Channel						Endplate				
					Section	h _c	w _c	m	t _{fc}	t _{wc}	h _p	w _p	t _p	p _f	g
Set3	20	S87	SHS160 × 10	UKB356 x 127 x 33	cut from SHS160 × 12.5	379.0	160.0	120.0	12.5	12.5	379.0	155.4	15.0	50.0	90.0
		S88	SHS160 × 10	UKB356 x 127 x 33	cut from SHS160 × 10	379.0	160.0	100.0	10.0	10.0	379.0	155.4	15.0	60.0	80.0
		S89	SHS160 × 10	UKB356 x 127 x 33	cut from SHS160 × 8	379.0	160.0	90.0	8.0	8.0	379.0	155.4	15.0	80.0	80.0
		S90	SHS180 × 10	UKB356 x 127 x 33	UKPFC180 x 90 x 26	385.0	180.0	90.0	12.5	6.5	385.0	161.4	18.0	50.0	90.0
		S91	SHS180 × 10	UKB356 x 127 x 33	UKPFC180 x 75 x 20	385.0	180.0	75.0	10.5	6.0	385.0	161.4	18.0	60.0	80.0
		S92	SHS180 × 10	UKB356 x 127 x 33	UKPFC180 x 75 x 20	389.0	180.0	75.0	10.5	6.0	389.0	165.4	20.0	60.0	90.0
		S93	SHS180 × 10	UKB356 x 127 x 33	cut from SHS180 × 12.5	389.0	180.0	120.0	12.5	12.5	389.0	165.4	20.0	80.0	80.0
		S94	SHS180 × 10	UKB356 x 127 x 33	cut from SHS180 × 12.5	393.0	180.0	100.0	12.5	12.5	393.0	169.4	22.0	80.0	80.0
		S95	SHS180 × 10	UKB356 x 127 x 33	UKPFC180 x 90 x 26	393.0	180.0	90.0	12.5	6.5	393.0	169.4	22.0	50.0	80.0
		S96	SHS180 × 10	UKB356 x 127 x 33	cut from SHS180 × 10	399.0	180.0	120.0	10.0	10.0	399.0	175.4	25.0	100.0	80.0
		S97	SHS160 × 10	UKB356 x 127 x 33	cut from SHS160 × 12.5	379.0	160.0	120.0	12.5	12.5	379.0	155.4	15.0	50.0	90.0
		S98	SHS160 × 10	UKB356 x 127 x 33	cut from SHS160 × 10	379.0	160.0	100.0	10.0	10.0	379.0	155.4	15.0	60.0	80.0
		S99	SHS160 × 10	UKB356 x 127 x 33	cut from SHS160 × 8	379.0	160.0	90.0	8.0	8.0	379.0	155.4	15.0	80.0	80.0
		S100	SHS180 × 10	UKB356 x 127 x 33	UKPFC180 x 90 x 26	385.0	180.0	90.0	12.5	6.5	385.0	161.4	18.0	50.0	90.0
		S101	SHS180 × 10	UKB356 x 127 x 33	UKPFC180 x 75 x 20	385.0	180.0	75.0	10.5	6.0	385.0	161.4	18.0	60.0	80.0
		S102	SHS180 × 10	UKB356 x 127 x 33	UKPFC180 x 75 x 20	389.0	180.0	75.0	10.5	6.0	389.0	165.4	20.0	60.0	90.0
S103	SHS180 × 10	UKB356 x 127 x 33	cut from SHS180 × 12.5	389.0	180.0	120.0	12.5	12.5	389.0	165.4	20.0	80.0	80.0		
S104	SHS180 × 10	UKB356 x 127 x 33	cut from SHS180 × 12.5	393.0	180.0	100.0	12.5	12.5	393.0	169.4	22.0	80.0	80.0		
S105	SHS180 × 10	UKB356 x 127 x 33	UKPFC180 x 90 x 26	393.0	180.0	90.0	12.5	6.5	393.0	169.4	22.0	50.0	80.0		
S106	SHS180 × 10	UKB356 x 127 x 33	cut from SHS180 × 10	399.0	180.0	120.0	10.0	10.0	399.0	175.4	25.0	100.0	80.0		
Set3	24	S107	SHS180 × 10	UKB356 x 127 x 33	cut from SHS180 × 12.5	379.0	180.0	120.0	12.5	12.5	379.0	180.0	15.0	50.0	90.0
		S108	SHS180 × 10	UKB356 x 127 x 33	cut from SHS180 × 10	379.0	180.0	100.0	10.0	10.0	379.0	180.0	15.0	60.0	90.0
		S109	SHS180 × 10	UKB356 x 127 x 33	cut from SHS180 × 8	379.0	180.0	90.0	8.0	8.0	379.0	180.0	15.0	80.0	90.0
		S110	SHS180 × 10	UKB356 x 127 x 33	UKPFC180 x 90 x 26	385.0	180.0	90.0	12.5	6.5	385.0	180.0	18.0	50.0	90.0
		S111	SHS180 × 10	UKB356 x 127 x 33	UKPFC180 x 75 x 20	385.0	180.0	75.0	10.5	6.0	385.0	180.0	18.0	60.0	90.0
		S112	SHS180 × 10	UKB356 x 127 x 33	UKPFC180 x 75 x 20	389.0	180.0	75.0	10.5	6.0	389.0	180.0	20.0	60.0	90.0
		S113	SHS180 × 10	UKB356 x 127 x 33	cut from SHS180 × 12.5	389.0	180.0	120.0	12.5	12.5	389.0	180.0	20.0	80.0	90.0
		S114	SHS180 × 10	UKB356 x 127 x 33	cut from SHS180 × 12.5	393.0	180.0	100.0	12.5	12.5	393.0	180.0	22.0	80.0	90.0
		S115	SHS180 × 10	UKB356 x 127 x 33	UKPFC180 x 90 x 26	393.0	180.0	90.0	12.5	6.5	393.0	180.0	22.0	50.0	90.0
		S116	SHS180 × 10	UKB356 x 127 x 33	cut from SHS180 × 10	399.0	180.0	120.0	10.0	10.0	399.0	180.0	25.0	100.0	90.0

Table A.4: Schedule of RCC dimensions of Set4 in the parametric study

Set No.	d _{bolt}	Specimen	Column Section (S355)	Beam Section (S355)	Channel						Endplate				
					Section	h _c	w _c	m	t _{fc}	t _{wc}	h _p	w _p	t _p	p _f	g
Set4	16	S117	SHS200 × 10	UKB305 x 165 x 40	cut from SHS200 × 12.5	333.4	200.0	90.0	12.5	12.5	333.4	195.0	15.0	50.0	120.0
		S118	SHS200 × 10	UKB305 x 165 x 40	cut from SHS200 × 10	339.4	200.0	120.0	10.0	10.0	339.4	200.0	18.0	60.0	100.0
		S119	SHS250 × 10	UKB305 x 165 x 40	UKPFC230 x 90 x32	343.4	230.0	90.0	14.0	7.5	343.4	205.0	20.0	80.0	100.0
		S120	SHS250 × 10	UKB305 x 165 x 40	UKPFC230 x 90 x32	347.4	230.0	90.0	14.0	7.5	347.4	209.0	22.0	100.0	100.0
		S121	SHS250 × 10	UKB305 x 165 x 40	UKPFC230 x 75 x 26	343.4	230.0	75.0	12.5	6.5	343.4	205.0	20.0	80.0	90.0
		S122	SHS200 × 10	UKB305 x 165 x 40	UKPFC200 x 90 x30	333.4	200.0	90.0	14.0	7.0	333.4	195.0	15.0	50.0	90.0
		S123	SHS200 × 10	UKB305 x 165 x 40	cut from SHS200 × 8	339.4	200.0	100.0	8.0	8.0	339.4	200.0	18.0	60.0	90.0
		S124	SHS250 × 10	UKB305 x 165 x 40	UKPFC230 x 90 x 32	347.4	230.0	90.0	14.0	7.5	347.4	209.0	22.0	100.0	80.0
	S125	SHS250 × 10	UKB305 x 165 x 40	UKPFC230 x 75 x 26	353.4	230.0	75.0	12.5	6.5	353.4	215.0	25.0	100.0	80.0	
	S126	SHS200 × 10	UKB305 x 165 x 40	cut from SHS200 × 12.5	339.4	200.0	75.0	12.5	12.5	339.4	200.0	18.0	60.0	80.0	
	S127	SHS200 × 10	UKB305 x 165 x 40	cut from SHS200 × 12.5	333.4	200.0	90.0	12.5	12.5	333.4	195.0	15.0	50.0	120.0	
	S128	SHS200 × 10	UKB305 x 165 x 40	cut from SHS200 × 10	339.4	200.0	120.0	10.0	10.0	339.4	200.0	18.0	60.0	100.0	
	S129	SHS250 × 10	UKB305 x 165 x 40	UKPFC230 x 90 x32	343.4	230.0	90.0	14.0	7.5	343.4	205.0	20.0	80.0	100.0	
	S130	SHS250 × 10	UKB305 x 165 x 40	UKPFC230 x 90 x32	347.4	230.0	90.0	14.0	7.5	347.4	209.0	22.0	100.0	100.0	
	S131	SHS250 × 10	UKB305 x 165 x 40	UKPFC230 x 75 x 26	343.4	230.0	75.0	12.5	6.5	343.4	205.0	20.0	80.0	90.0	
	S132	SHS200 × 10	UKB305 x 165 x 40	UKPFC200 x 90 x30	333.4	200.0	90.0	14.0	7.0	333.4	195.0	15.0	50.0	90.0	
S133	SHS200 × 10	UKB305 x 165 x 40	cut from SHS200 × 8	339.4	200.0	100.0	8.0	8.0	339.4	200.0	18.0	60.0	90.0		
S134	SHS250 × 10	UKB305 x 165 x 40	UKPFC230 x 90 x 32	347.4	230.0	90.0	14.0	7.5	347.4	209.0	22.0	100.0	80.0		
S135	SHS250 × 10	UKB305 x 165 x 40	UKPFC230 x 75 x 26	353.4	230.0	75.0	12.5	6.5	353.4	215.0	25.0	100.0	80.0		
S136	SHS200 × 10	UKB305 x 165 x 40	cut from SHS200 × 12.5	339.4	200.0	75.0	12.5	12.5	339.4	200.0	18.0	60.0	80.0		
S137	SHS200 × 10	UKB305 x 165 x 40	cut from SHS200 × 12.5	333.4	200.0	90.0	12.5	12.5	333.4	195.0	15.0	50.0	120.0		
S138	SHS200 × 10	UKB305 x 165 x 40	cut from SHS200 × 10	339.4	200.0	120.0	10.0	10.0	339.4	200.0	18.0	60.0	100.0		
S139	SHS250 × 10	UKB305 x 165 x 40	UKPFC230 x 90 x32	343.4	230.0	90.0	14.0	7.5	343.4	205.0	20.0	80.0	100.0		
S140	SHS250 × 10	UKB305 x 165 x 40	UKPFC230 x 90 x32	347.4	230.0	90.0	14.0	7.5	347.4	209.0	22.0	100.0	100.0		
S141	SHS250 × 10	UKB305 x 165 x 40	UKPFC230 x 75 x 26	343.4	230.0	75.0	12.5	6.5	343.4	205.0	20.0	80.0	90.0		
S142	SHS200 × 10	UKB305 x 165 x 40	UKPFC200 x 90 x30	333.4	200.0	90.0	14.0	7.0	333.4	195.0	15.0	50.0	90.0		
S143	SHS200 × 10	UKB305 x 165 x 40	cut from SHS200 × 8	339.4	200.0	100.0	8.0	8.0	339.4	200.0	18.0	60.0	90.0		
S144	SHS250 × 10	UKB305 x 165 x 40	UKPFC230 x 90 x 32	347.4	230.0	90.0	14.0	7.5	347.4	209.0	22.0	100.0	120.0		
S145	SHS250 × 10	UKB305 x 165 x 40	UKPFC230 x 75 x 26	353.4	230.0	75.0	12.5	6.5	353.4	215.0	25.0	100.0	100.0		
S146	SHS200 × 10	UKB305 x 165 x 40	cut from SHS200 × 12.5	339.4	200.0	75.0	12.5	12.5	339.4	200.0	18.0	60.0	90.0		

Table A.5: Schedule of RCC dimensions of Set5 in the parametric study

Set No.	d _{bolt}	Specimen	Column Section (S355)	Beam Section (S355)	Channel					Endplate						
					Section	h _c	w _c	m	t _{fc}	t _{wc}	h _p	w _p	t _p	p _f	g	
16		S147	SHS140 × 10	UKB254 x 102 x 28	cut from SHS140 × 10	290.4	140.0	100.0	10.0	10.0	290.4	132.2	12.0	40.0	80.0	
		S148	SHS140 × 10	UKB254 x 102 x 28	cut from SHS140 × 12.5	290.4	140.0	75.0	12.5	12.5	290.4	132.2	12.0	60.0	80.0	
		S149	SHS140 × 10	UKB254 x 102 x 28	cut from SHS140 × 10	290.4	140.0	90.0	10.0	10.0	290.4	132.2	12.0	80.0	80.0	
		S150	SHS140 × 10	UKB254 x 102 x 28	cut from SHS140 × 8	290.4	140.0	90.0	8.0	8.0	290.4	132.2	15.0	50.0	80.0	
		S151	SHS140 × 10	UKB254 x 102 x 28	cut from SHS140 × 12.5	290.4	140.0	120.0	12.5	12.5	290.4	132.2	15.0	80.0	80.0	
		S152	SHS140 × 10	UKB254 x 102 x 28	cut from SHS140 × 10	290.4	140.0	120.0	10.0	10.0	290.4	132.2	15.0	40.0	80.0	
		S153	SHS140 × 10	UKB254 x 102 x 28	cut from SHS140 × 12.5	296.4	140.0	75.0	12.5	12.5	296.4	138.2	18.0	60.0	80.0	
		S154	SHS140 × 10	UKB254 x 102 x 28	cut from SHS140 × 8	296.4	140.0	90.0	8.0	8.0	296.4	138.2	18.0	60.0	80.0	
		S155	SHS160 × 10	UKB254 x 102 x 28	cut from SHS160 × 12.5	300.4	160.0	120.0	12.5	12.5	300.4	142.2	20.0	80.0	90.0	
		S156	SHS160 × 10	UKB254 x 102 x 28	cut from SHS160 × 10	300.4	160.0	90.0	10.0	10.0	300.4	142.2	20.0	40.0	90.0	
Set5		S157	SHS140 × 10	UKB254 x 102 x 28	cut from SHS140 × 10	290.4	140.0	100.0	10.0	10.0	290.4	132.2	12.0	40.0	80.0	
		S158	SHS140 × 10	UKB254 x 102 x 28	cut from SHS140 × 12.5	290.4	140.0	75.0	12.5	12.5	290.4	132.2	12.0	60.0	80.0	
		S159	SHS140 × 10	UKB254 x 102 x 28	cut from SHS140 × 10	290.4	140.0	90.0	10.0	10.0	290.4	132.2	12.0	80.0	80.0	
		S160	SHS140 × 10	UKB254 x 102 x 28	cut from SHS140 × 8	290.4	140.0	90.0	8.0	8.0	290.4	132.2	15.0	50.0	80.0	
	20		S161	SHS140 × 10	UKB254 x 102 x 28	cut from SHS140 × 12.5	290.4	140.0	120.0	12.5	12.5	290.4	132.2	15.0	80.0	80.0
			S162	SHS140 × 10	UKB254 x 102 x 28	cut from SHS140 × 10	290.4	140.0	120.0	10.0	10.0	290.4	132.2	15.0	40.0	80.0
			S163	SHS140 × 10	UKB254 x 102 x 28	cut from SHS140 × 12.5	296.4	140.0	75.0	12.5	12.5	296.4	138.2	18.0	60.0	80.0
			S164	SHS140 × 10	UKB254 x 102 x 28	cut from SHS140 × 8	296.4	140.0	90.0	8.0	8.0	296.4	138.2	18.0	60.0	80.0
			S165	SHS160 × 10	UKB254 x 102 x 28	cut from SHS160 × 12.5	300.4	160.0	120.0	12.5	12.5	300.4	142.2	20.0	80.0	80.0
			S166	SHS160 × 10	UKB254 x 102 x 28	cut from SHS160 × 10	300.4	160.0	90.0	10.0	10.0	300.4	142.2	20.0	40.0	80.0

Table A.6: Main parameters of the moment-rotation curves and the observed failure modes of Set1

Set	Specimen	Resistance (kN.m)			Stiffness (kN.m/rad)			Rotation (rad)			Failure mode
No.		$M_{j,R,FE}$	$M_{j,Rd,FE}$	$M_{j,ult,FE}$	$S_{j,in,FE}$	$S_{j,FE}$	$S_{j,P,FE}$	$\phi_{j,R,FE}$	$\phi_{j,x,FE}$	$\phi_{j,ult,FE}$	
	S27	107.6	140.2	152.1	30261.5	10087.2	3167.9	0.0036	0.0056	0.0301	BF
	S28	48.8	72.1	128.7	19408.1	6469.4	2791.7	0.0025	0.0038	0.0415	BPO
	S29	69.9	98.0	146.4	13964.0	4654.7	1732.4	0.0050	0.0080	0.0652	BF
	S30	35.5	79.4	105.9	8264.8	2754.9	1801.0	0.0043	0.0057	0.0601	BPO
	S31	94.8	122.8	152.0	26989.0	8996.3	2690.1	0.0035	0.0056	0.0332	BF
	S32	33.4	61.4	121.6	9991.0	3330.3	1871.5	0.0033	0.0043	0.0615	BPO
	S33	62.2	91.9	146.4	11526.0	3842.0	1577.7	0.0054	0.0082	0.0770	BF
	S34	91.0	110.4	150.8	23580.6	7860.2	1873.3	0.0039	0.0072	0.0531	BF
	S35	30.2	92.6	101.3	5849.8	1949.9	1503.2	0.0052	0.0065	0.0711	BPO
	S36	30.1	58.7	119.7	9023.1	3007.7	1817.7	0.0033	0.0040	0.0674	BPO
	S37	123.4	155.5	219.9	25981.0	8660.3	2383.3	0.0048	0.0081	0.0564	BF
	S38	55.3	84.1	146.8	20614.4	6871.5	3095.9	0.0027	0.0044	0.0505	BPO
	S39	75.6	107.0	180.7	14799.2	4933.1	1907.1	0.0051	0.0083	0.0890	BPO
	S40	40.4	107.0	121.9	9129.3	3043.1	1960.7	0.0044	0.0058	0.0613	BPO
Set1	S41	106.3	135.4	220.7	22724.2	7574.7	2174.9	0.0047	0.0078	0.0690	BF
	S42	36.1	64.9	140.2	11182.9	3727.6	2091.2	0.0032	0.0042	0.0757	BPO
	S43	66.3	98.6	174.3	12427.5	4142.5	1728.2	0.0053	0.0081	0.0905	BPO
	S44	93.3	122.5	221.6	19659.7	6553.2	2018.0	0.0047	0.0076	0.0837	BF
	S45	32.0	90.2	117.6	6873.1	2291.0	1660.2	0.0046	0.0059	0.0755	BPO
	S46	33.9	65.9	138.5	9590.9	3197.0	1967.1	0.0035	0.0045	0.0769	BPO
	S47	136.8	217.9	272.7	14789.9	4930.0	2305.0	0.0093	0.0123	0.1055	BPO
	S48	63.3	94.4	163.8	23496.1	7832.0	3285.2	0.0027	0.0042	0.0548	BPO
	S49	94.5	134.3	203.0	18979.7	6326.6	2347.9	0.0050	0.0079	0.0854	BPO
	S50	82.2	118.1	197.0	15882.5	5294.2	2039.0	0.0052	0.0081	0.0975	BPO
	S51	44.4	92.0	135.0	9970.6	3323.5	2044.4	0.0045	0.0061	0.0710	BPO
	S52	118.4	149.7	259.7	24070.8	8023.6	2252.3	0.0049	0.0086	0.1035	BPO
	S53	40.6	72.2	155.5	12040.6	4013.5	2224.6	0.0034	0.0044	0.0827	BPO
	S54	71.4	105.3	189.5	13522.8	4507.6	1815.2	0.0053	0.0081	0.1104	BPO
	S55	101.4	129.7	252.2	20888.2	6962.7	2133.7	0.0049	0.0084	0.0955	BPO
	S56	37.4	90.2	132.7	8245.0	2748.3	1860.5	0.0045	0.0060	0.0878	BPO

Note: BPO denotes Bolt Pull-Out, EPO denotes End plate Pulled Outwards, BF denotes Bolt Failure

Table A.7: Main parameters of the moment-rotation curves and the observed failure modes of Set2

Set	Specimen	Resistance (kN.m)			Stiffness (kN.m/rad)			Rotation (rad)			Failure mode
No.		$M_{j,R,FE}$	$M_{j,Rd,FE}$	$M_{j,ult,FE}$	$S_{j,in,FE}$	$S_{j,FE}$	$S_{j,P,FE}$	$\phi_{j,R,FE}$	$\phi_{j,x,FE}$	$\phi_{j,ult,FE}$	
	S57	37.7	58.2	97.8	12157.0	4052.3	1792.5	0.0031	0.0106	0.0543	BPO
	S58	27.3	58.8	83.8	12176.4	4058.8	1676.7	0.0022	0.0025	0.0286	BPO
	S59	31.8	61.8	85.6	8663.4	2887.8	1680.3	0.0037	0.0055	0.0535	BPO
	S60	37.0	63.5	96.4	8914.7	2971.6	1522.0	0.0041	0.0064	0.0613	BPO
	S61	22.8	46.3	80.9	7206.3	2402.1	1507.2	0.0032	0.0042	0.0558	BPO
	S62	29.1	50.2	94.3	9524.0	3174.7	1638.7	0.0031	0.0042	0.0663	BPO
	S63	25.9	63.0	80.0	5821.4	1940.5	1318.9	0.0044	0.0062	0.0689	BPO
	S64	18.3	41.6	79.6	6502.3	2167.4	1458.5	0.0028	0.0034	0.0613	BPO
	S65	33.4	60.1	95.2	7961.8	2653.9	1449.9	0.0042	0.0063	0.0670	BPO
	S66	43.6	70.8	100.9	10776.3	3592.1	1668.7	0.0040	0.0066	0.0516	BPO
	S67	34.9	55.9	112.9	10894.3	3631.4	1720.8	0.0032	0.0047	0.0712	BPO
	S68	27.9	55.4	99.0	8013.7	2671.2	1587.3	0.0035	0.0048	0.0669	BPO
	S69	30.7	62.4	98.6	7691.2	2563.7	1551.6	0.0040	0.0057	0.0666	BPO
	S70	37.4	62.9	112.0	9077.4	3025.8	1537.8	0.0041	0.0061	0.0721	BPO
Set2	S71	25.1	55.2	98.4	7084.9	2361.6	1512.0	0.0035	0.0048	0.0780	BPO
	S72	30.8	52.0	111.0	9414.0	3138.0	1650.1	0.0033	0.0046	0.0726	BPO
	S73	25.3	83.9	92.5	4719.6	1573.2	1227.8	0.0054	0.0065	0.0788	BPO
	S74	17.7	48.2	96.2	5693.2	1897.7	1385.4	0.0031	0.0036	0.0829	BPO
	S75	31.7	61.0	107.5	7145.7	2381.9	1390.2	0.0044	0.0061	0.0805	BPO
	S76	32.2	59.7	107.0	7064.3	2354.8	1346.2	0.0046	0.0064	0.0872	BPO
	S77	41.7	65.2	128.5	11516.9	3839.0	1834.9	0.0036	0.0055	0.0810	BPO
	S78	32.4	64.7	113.1	8675.7	2891.9	1731.1	0.0037	0.0051	0.0748	BPO
	S79	36.4	86.2	112.9	7568.6	2522.9	1666.9	0.0048	0.0065	0.0773	BPO
	S80	43.5	74.8	129.1	9714.4	3238.1	1648.2	0.0045	0.0067	0.0917	BPO
	S81	28.2	61.7	111.2	7746.5	2582.2	1647.3	0.0036	0.0049	0.0813	BPO
	S82	36.9	63.1	126.7	10173.8	3391.3	1760.6	0.0036	0.0051	0.0819	BPO
	S83	28.2	74.9	106.9	5633.5	1877.8	1322.7	0.0050	0.0065	0.0906	BPO
	S84	20.1	63.1	110.0	6154.2	2051.4	1537.1	0.0033	0.0037	0.0869	BPO
	S85	36.6	64.8	118.1	7756.5	2585.5	1428.0	0.0047	0.0068	0.0882	BPO
	S86	36.1	65.5	120.8	7669.1	2556.4	1418.4	0.0047	0.0067	0.0916	BPO

Note: BPO denotes Bolt Pull-Out, EPO denotes End plate Pulled Outwards, BF denotes Bolt Failure

Table A.8: Main parameters of the moment-rotation curves and the observed failure modes of Set3

Set	Specimen	Resistance (kN.m)			Stiffness (kN.m/rad)			Rotation (rad)			Failure mode
No.		$M_{j,R,FE}$	$M_{j,Rd,FE}$	$M_{j,ult,FE}$	$S_{j,in,FE}$	$S_{j,FE}$	$S_{j,P,FE}$	$\phi_{j,R,FE}$	$\phi_{j,x,FE}$	$\phi_{j,ult,FE}$	
	S87	82.8	103.9	103.9	10992.6	3664.2	1774.2	0.0075	0.0096	0.0360	BF
	S88	62.2	80.5	98.1	8794.3	2931.4	867.6	0.0071	0.0115	0.0620	BF
	S89	43.1	60.6	82.6	6403.1	2134.4	777.5	0.0067	0.0107	0.0835	BPO
	S90	30.9	48.0	70.3	7636.6	2545.5	1160.9	0.0040	0.0060	0.0568	BPO
	S91	22.6	41.9	62.1	5494.9	1831.6	1033.7	0.0041	0.0060	0.0678	BPO
	S92	27.2	49.6	65.9	6530.8	2176.9	1178.2	0.0042	0.0063	0.0492	BPO
	S93	76.4	97.7	101.1	10065.0	3355.0	1032.8	0.0076	0.0114	0.0531	BF
	S94	77.7	100.9	102.4	10723.4	3574.5	1227.5	0.0072	0.0106	0.0536	BF
	S95	28.4	49.8	72.9	7233.0	2411.0	1260.0	0.0039	0.0058	0.0628	BPO
	S96	57.0	79.1	99.7	7589.5	2529.8	918.4	0.0075	0.0058	0.0723	BF
	S97	109.9	126.7	150.3	11179.3	3726.4	677.8	0.0098	0.0184	0.0928	BF
	S98	73.9	90.5	127.1	9221.0	3073.7	793.4	0.0080	0.0145	0.1021	BPO
	S99	51.8	68.7	93.3	6726.8	2242.3	725.6	0.0077	0.0134	0.1064	BPO
	S100	39.8	57.6	85.4	8560.7	2853.6	1142.9	0.0047	0.0074	0.0622	BPO
Set3	S101	28.7	51.1	75.6	5792.1	1930.7	1025.8	0.0050	0.0072	0.0841	BPO
	S102	34.5	57.8	79.4	7255.0	2418.3	1177.3	0.0048	0.0072	0.0754	BPO
	S103	90.6	108.3	141.4	10228.6	3409.5	768.1	0.0089	0.0151	0.0890	BF
	S104	94.0	113.1	145.9	11270.1	3756.7	874.6	0.0083	0.0144	0.0822	BF
	S105	35.3	57.1	88.5	8427.7	2809.2	1322.8	0.0042	0.0064	0.0630	BPO
	S106	66.4	88.2	124.6	8109.3	2703.1	870.6	0.0082	0.0134	0.1100	BPO
	S107	126.8	138.7	184.3	11782.4	3927.5	555.0	0.0108	0.0244	0.1446	BPO
	S108	95.7	105.5	141.0	10263.4	3421.1	558.2	0.0093	0.0205	0.1189	BPO
	S109	73.8	82.5	105.9	7973.3	2657.8	450.9	0.0093	0.0214	0.1051	BPO
	S110	51.7	72.8	98.3	9309.9	3103.3	1164.6	0.0055	0.0094	0.0731	BPO
	S111	44.2	64.4	87.0	7756.6	2585.5	1001.1	0.0057	0.0096	0.0720	BPO
	S112	48.0	66.5	88.9	8316.2	2772.1	1018.9	0.0058	0.0108	0.0782	BPO
	S113	118.2	125.4	170.4	11100.2	3700.1	465.7	0.0106	0.0261	0.1576	BPO
	S114	117.2	133.7	177.5	11434.1	3811.4	696.0	0.0103	0.0197	0.1430	BPO
	S115	58.6	83.8	99.2	9562.1	3187.4	1193.5	0.0061	0.0103	0.0764	BPO
	S116	84.2	104.0	137.4	9355.9	3118.6	805.2	0.0090	0.0158	0.0989	BPO

Note: BPO denotes Bolt Pull-Out, EPO denotes End plate Pulled Outwards, BF denotes Bolt Failure

Table A.9: Main parameters of the moment-rotation curves and the observed failure modes of Set4

Set	Specimen	Resistance (kN.m)			Stiffness (kN.m/rad)			Rotation (rad)			Failure mode
No.		$M_{j,R,FE}$	$M_{j,Rd,FE}$	$M_{j,ult,FE}$	$S_{j,in,FE}$	$S_{j,FE}$	$S_{j,P,FE}$	$\phi_{j,R,FE}$	$\phi_{j,x,FE}$	$\phi_{j,ult,FE}$	
	S117	72.2	89.9	92.6	10901.1	3633.7	1105.4	0.0066	0.0100	0.0430	BF
	S118	49.9	60.8	89.3	7176.6	2392.2	602.8	0.0069	0.0125	0.0897	BF
	S119	26.3	40.0	68.4	4152.4	1384.1	601.6	0.0063	0.0093	0.1103	BPO
	S120	26.0	40.3	68.0	3819.8	1273.3	569.2	0.0068	0.0105	0.1257	BPO
	S121	16.9	34.4	56.6	2736.3	912.1	557.9	0.0062	0.0077	0.1056	BPO
	S122	25.3	36.4	68.3	5781.6	1927.2	820.6	0.0044	0.0070	0.0775	BPO
	S123	30.3	42.9	72.7	4266.7	1422.2	540.9	0.0071	0.0113	0.1121	BPO
	S124	21.4	35.1	64.5	3181.8	1060.6	524.3	0.0067	0.0099	0.1377	BPO
	S125	15.9	32.3	58.3	2558.0	852.7	539.8	0.0062	0.0075	0.1172	BPO
	S126	65.4	77.7	93.7	9315.5	3105.2	675.6	0.0070	0.0130	0.0738	BF
	S127	92.7	98.4	128.7	11317.3	3772.4	475.3	0.0082	0.0192	0.1036	BF
	S128	55.7	66.5	105.6	7569.0	2523.0	627.6	0.0074	0.0133	0.1340	BPO
	S129	29.8	44.2	77.1	4505.8	1501.9	643.9	0.0066	0.0096	0.1236	BPO
	S130	30.4	46.8	77.4	4074.8	1358.3	592.9	0.0074	0.0116	0.1380	BPO
Set4	S131	19.5	36.5	64.8	3084.5	1028.2	592.0	0.0063	0.0082	0.1149	BPO
	S132	29.8	44.1	79.8	6205.3	2068.4	877.9	0.0048	0.0074	0.0878	BPO
	S133	32.8	44.8	81.5	4794.0	1598.0	599.1	0.0068	0.0105	0.1251	BPO
	S134	46.3	60.0	88.3	5685.6	1895.2	577.7	0.0081	0.0155	0.1313	BPO
	S135	17.7	35.8	67.4	2804.1	934.7	585.4	0.0063	0.0085	0.1322	BPO
	S136	74.0	85.0	130.4	9651.0	3217.0	637.6	0.0077	0.0155	0.1122	BF
	S137	105.5	108.9	153.5	11342.8	3780.9	409.7	0.0093	0.0260	0.1512	BPO
	S138	60.6	74.1	116.0	8002.5	2667.5	701.8	0.0076	0.0133	0.1235	BPO
	S139	34.7	49.8	86.5	4840.4	1613.5	652.4	0.0072	0.0110	0.1303	BPO
	S140	34.9	49.8	85.5	4564.2	1521.4	597.9	0.0077	0.0125	0.1391	BPO
	S141	22.5	40.8	74.6	3475.8	1158.6	649.5	0.0065	0.0086	0.1324	BPO
	S142	37.6	52.6	89.6	6977.3	2325.8	889.4	0.0054	0.0088	0.0920	BPO
	S143	37.2	50.5	89.3	5292.5	1764.2	645.7	0.0070	0.0112	0.1227	BPO
	S144	47.0	60.0	88.3	5651.2	1883.7	567.4	0.0083	0.0155	0.1313	BPO
	S145	26.2	45.6	80.3	3946.3	1315.4	697.3	0.0066	0.0099	0.1232	BPO
	S146	86.6	97.9	149.4	10768.8	3589.6	665.9	0.0080	0.0161	0.1387	BPO

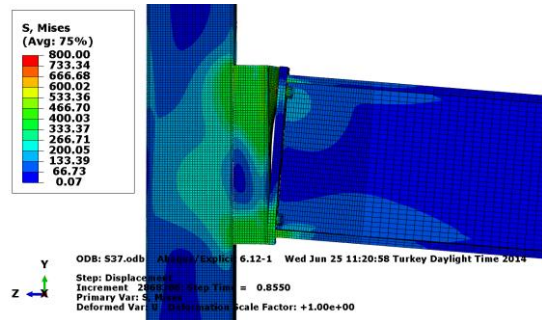
Note: BPO denotes Bolt Pull-Out, EPO denotes End plate Pulled Outwards, BF denotes Bolt Failure

Table A.10: Main parameters of the moment-rotation curves and the observed failure modes of Set5

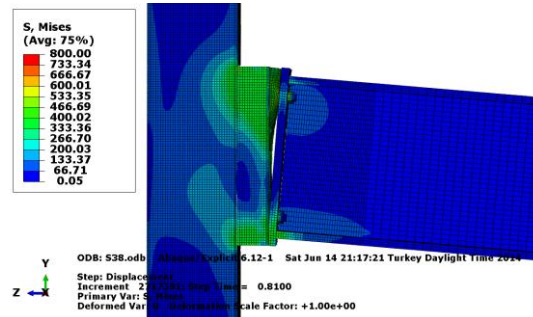
Set	Specimen	Resistance (kN.m)			Stiffness (kN.m/rad)			Rotation (rad)			Failure mode
No.		$M_{i,R,FE}$	$M_{j,Rd,FE}$	$M_{j,ult,FE}$	$S_{j,in,FE}$	$S_{j,FE}$	$S_{j,P,FE}$	$\phi_{i,R,FE}$	$\phi_{j,x,FE}$	$\phi_{j,ult,FE}$	
	S147	54.9	58.8	75.3	5682.0	1894.0	248.8	0.0097	0.0227	0.1428	BF
	S148	56.2	60.4	72.2	5948.0	1982.7	241.0	0.0094	0.0203	0.1175	BF
	S149	47.1	51.2	66.9	4397.5	1465.8	188.0	0.0107	0.0241	0.1676	EPO
	S150	38.7	46.3	63.0	4983.5	1661.2	399.1	0.0078	0.0141	0.1118	BPO
	S151	60.1	67.1	72.0	5527.7	1842.6	246.2	0.0109	0.0206	0.1066	BF
	S152	54.4	63.0	76.6	6149.9	2050.0	407.3	0.0088	0.0162	0.0868	BF
	S153	72.8	75.4	76.3	7229.7	2409.9	109.2	0.0101	0.0176	0.0527	BF
	S154	40.1	50.4	65.4	5045.4	1681.8	452.6	0.0079	0.0134	0.1002	BPO
	S155	68.7	69.4	71.8	6283.9	2094.6	52.0	0.0109	0.0297	0.0799	BF
	S156	51.2	59.6	75.4	7023.2	2341.1	448.1	0.0073	0.0139	0.0847	BF
Set5											
	S157	60.6	65.4	85.0	5942.6	1980.9	251.6	0.0102	0.0246	0.1343	BPO
	S158	61.3	67.4	87.6	6038.1	2012.7	289.1	0.0101	0.0205	0.1373	EPO
	S159	48.2	49.2	67.1	4511.3	1503.8	157.1	0.0107	0.0287	0.1764	EPO
	S160	46.1	54.0	69.9	5251.9	1750.6	376.8	0.0088	0.0166	0.1159	BPO
	S161	68.9	71.6	88.9	5608.0	1869.3	182.8	0.0123	0.0307	0.1450	BF
	S162	65.7	73.7	91.198	6357.1	2119.0	333.7	0.0103	0.0219	0.1251	BPO
	S163	85.9	94.2	105.92	7437.2	2479.1	302.1	0.0116	0.0226	0.1103	BF
	S164	47.6	59.2	71.576	5440.3	1813.4	452.5	0.0088	0.0149	0.1120	BPO
	S165	69.1	74.5	93.955	6192.3	2064.1	250.2	0.0112	0.0239	0.1364	BF
	S166	53.3	62.1	87.594	6832.9	2277.6	468.5	0.0078	0.0149	0.1234	BPO

Note: BPO denotes Bolt Pull-Out, EPO denotes End plate Pulled Outwards, BF denotes Bolt Failure

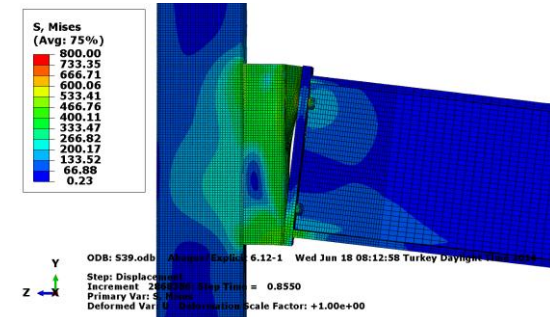
Appendix B: Von Mises Stress Distributions of Selected RCC and DRCC Prior to Failure



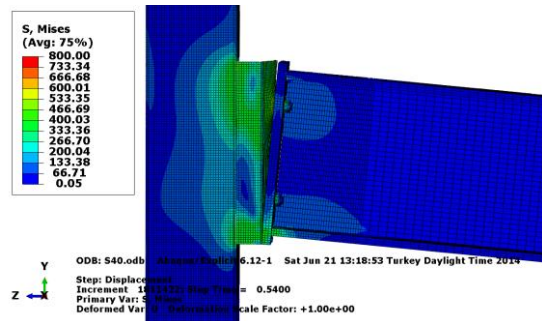
(a)



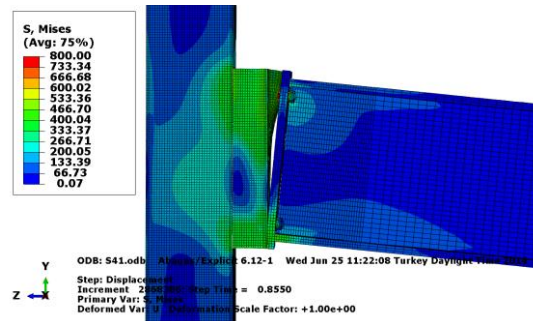
(b)



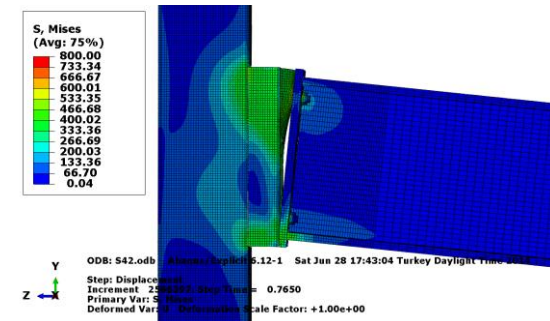
(c)



(d)

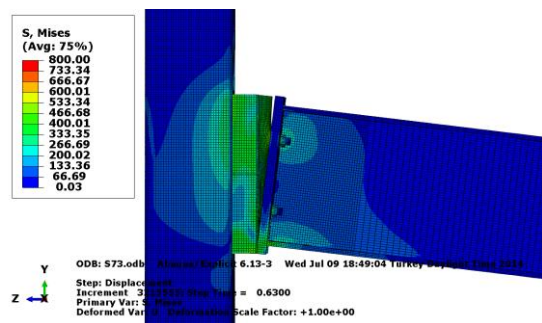


(e)

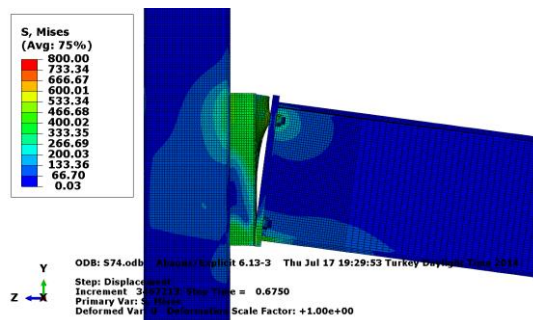


(f)

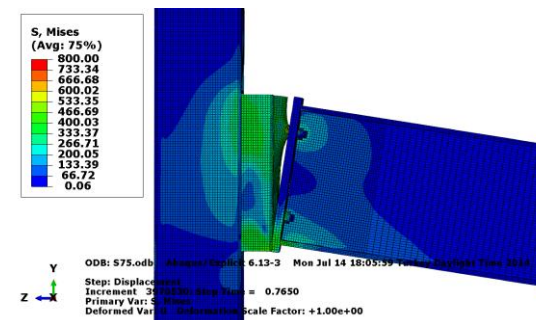
Figure B.1: Von Mises stress distributions of RCC joints prior to failure: (a) S37, (b) S38, (c) S39, (d) S40, (e) S41 and (f) S42



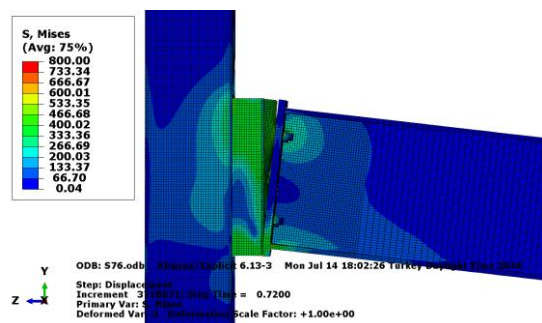
(a)



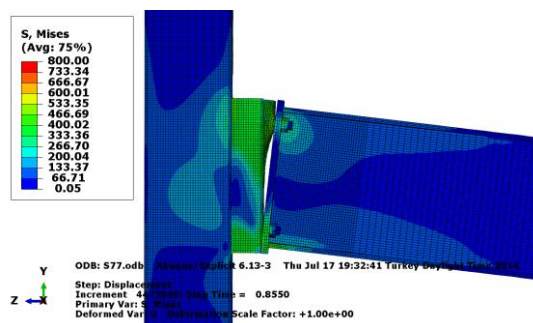
(b)



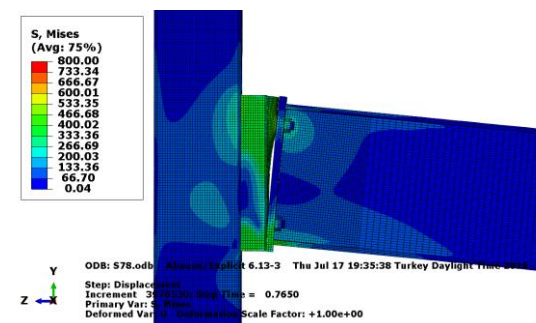
(c)



(d)

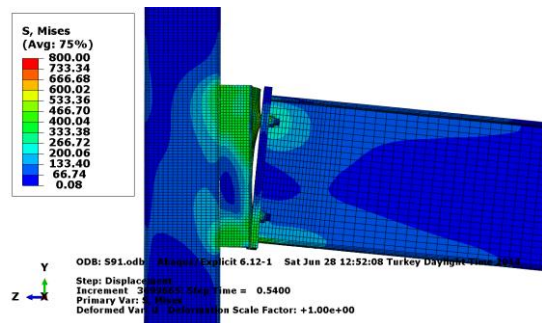


(e)

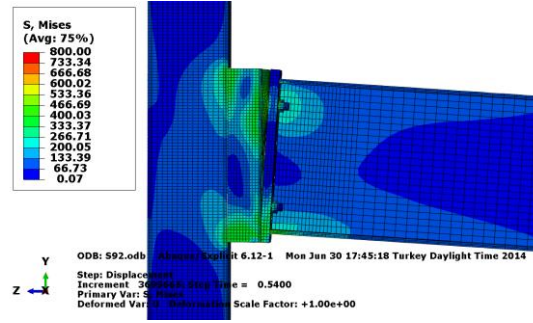


(f)

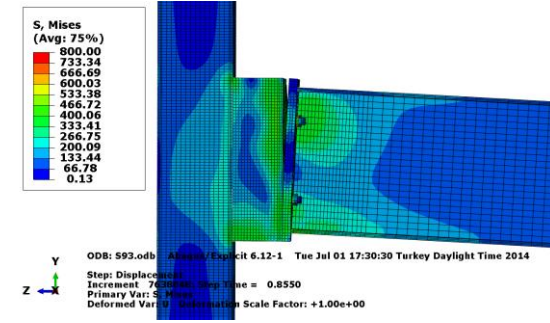
Figure B.2: Von Mises stress distributions of RCC joints prior to failure: (a) S73, (b) S74, (c) S75, (d) S76, (e) S77 and (f) S78



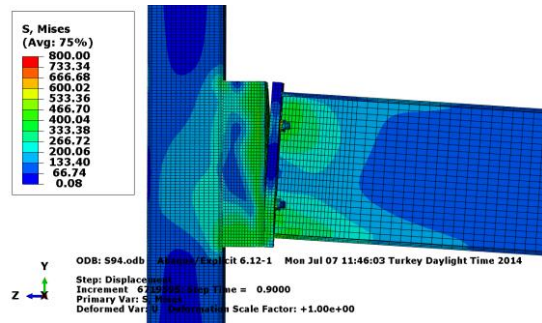
(a)



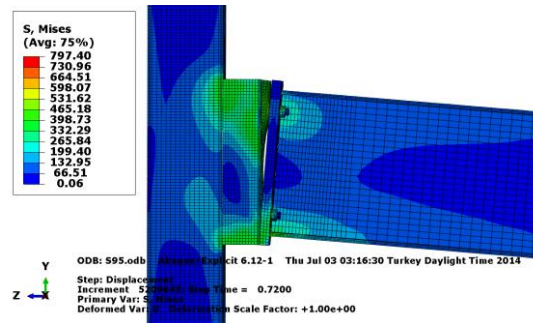
(b)



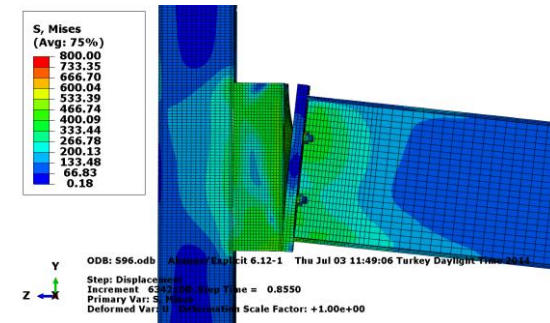
(c)



(d)

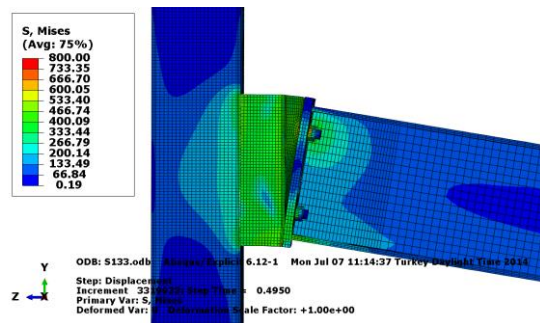


(e)

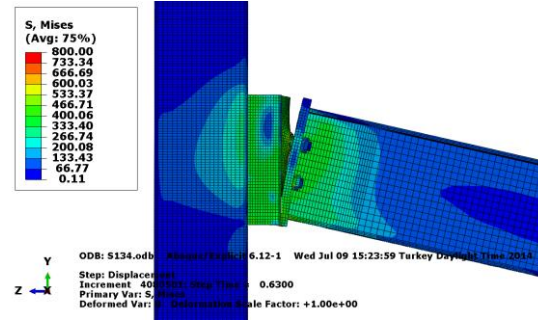


(f)

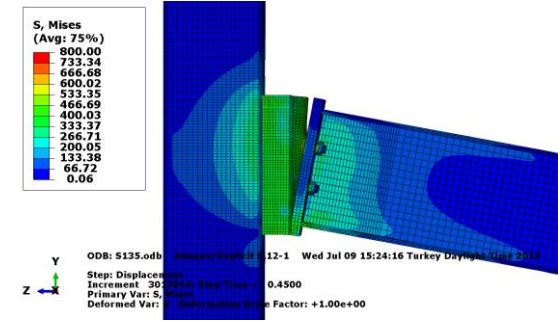
Figure B.3: Von Mises stress distributions of RCC joints prior to failure: (a) S91, (b) S92, (c) S93, (d) S94, (e) S95 and (f) S96



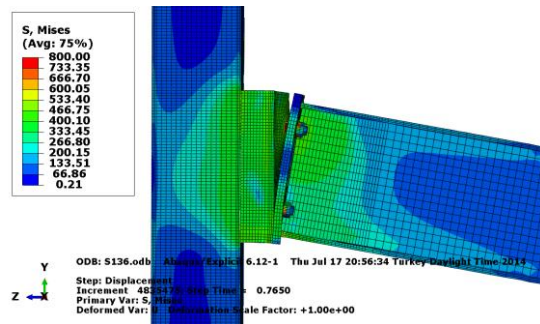
(a)



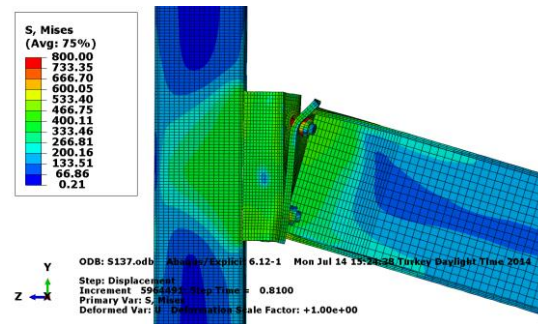
(b)



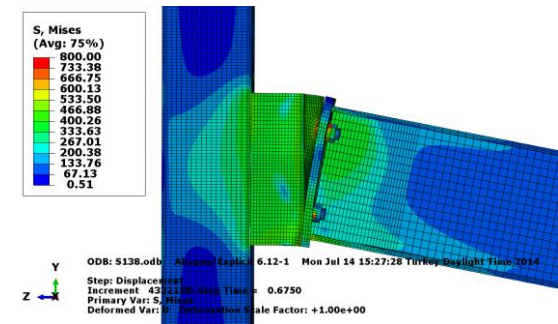
(c)



(d)

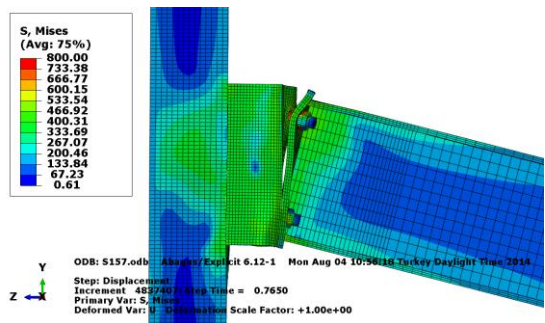


(e)

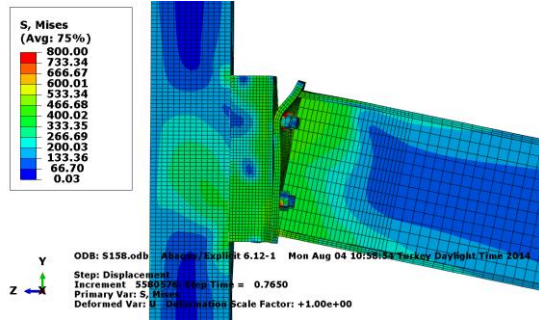


(f)

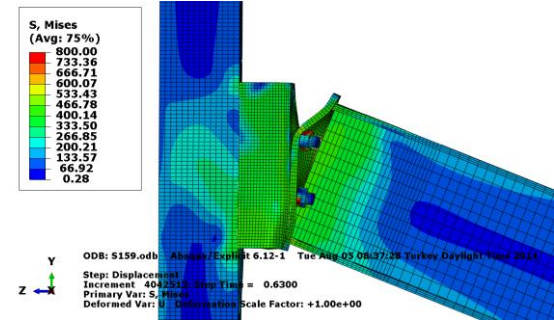
Figure B.4: Von Mises stress distributions of RCC joints prior to failure: (a) S133, (b) S134, (c) S135, (d) S136, (e) S137 and (f) S138



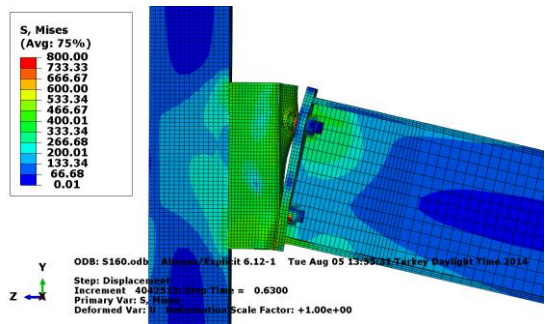
(a)



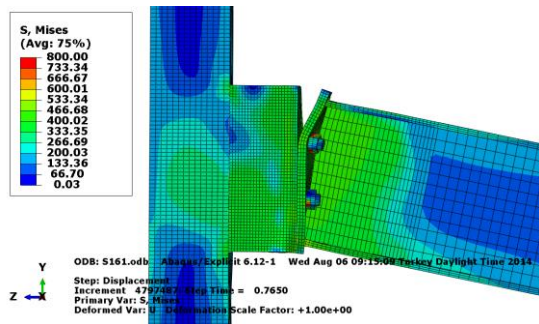
(b)



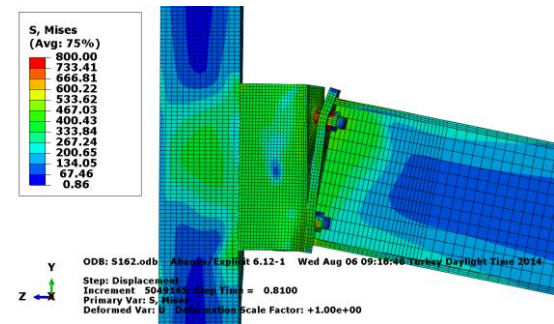
(c)



(d)

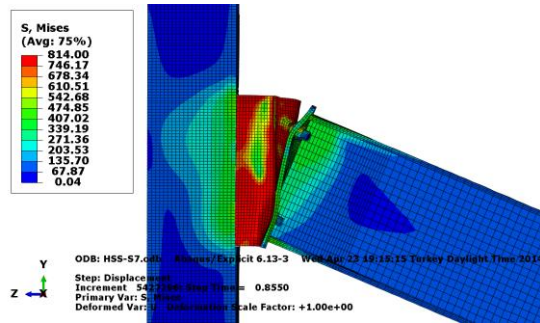


(e)

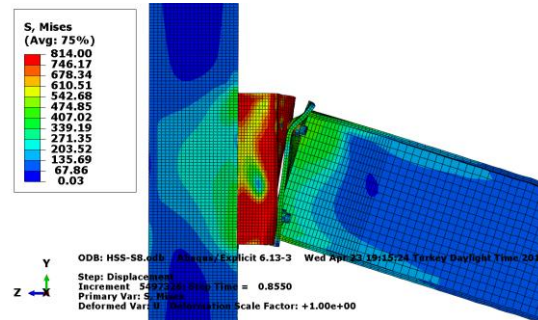


(f)

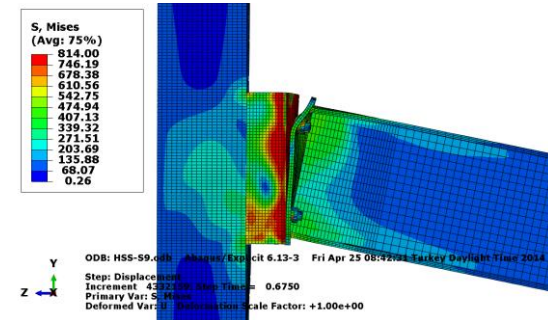
Figure B.5: Von Mises stress distributions of RCC joints prior to failure: (a) S157, (b) S158, (c) S159, (d) S160, (e) S161 and (f) S162



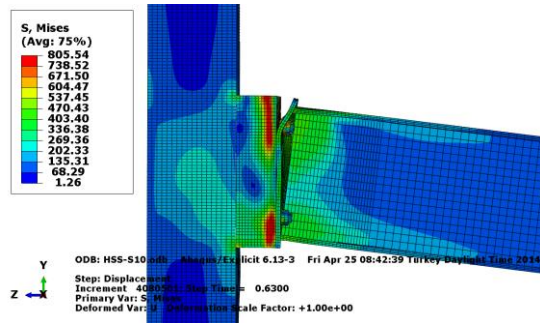
(a)



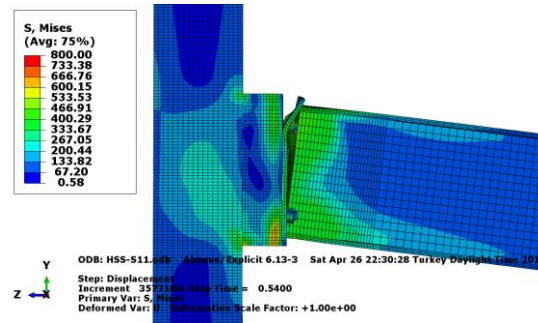
(b)



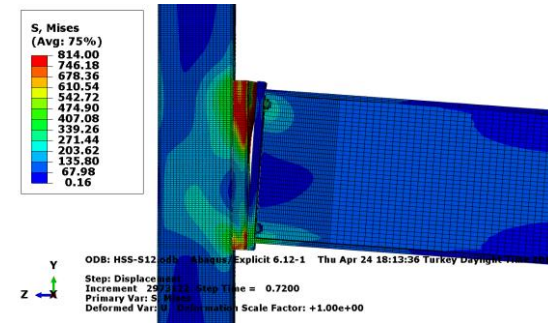
(c)



(d)

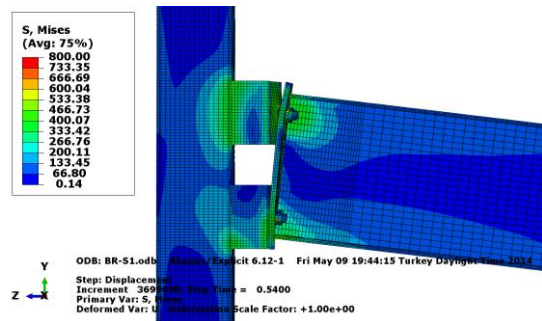


(e)

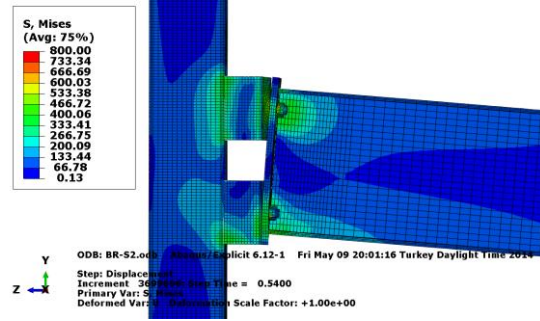


(f)

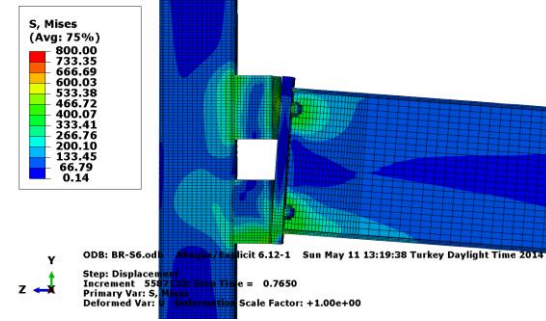
Figure B.6: Von Mises stress distributions of HSS-RC joints prior to failure: (a) HSS-S7, (b) HSS-S8, (c) HSS-S9, (d) HSS-S10, (e) HSS-S11 and (f) HSS-S12



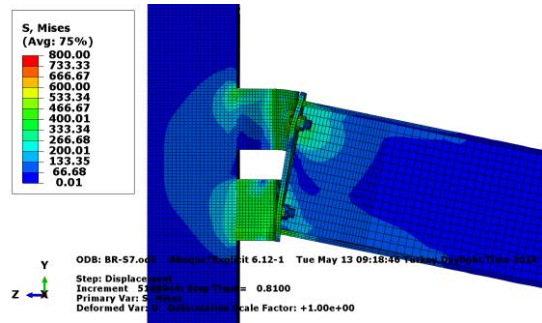
(a)



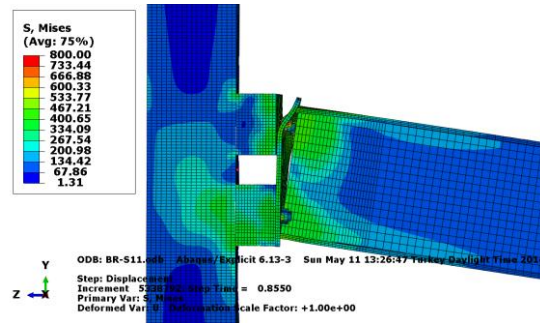
(b)



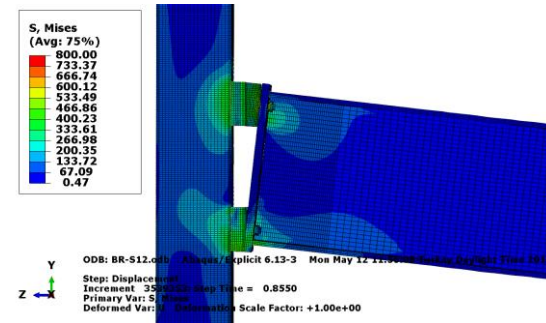
(c)



(d)

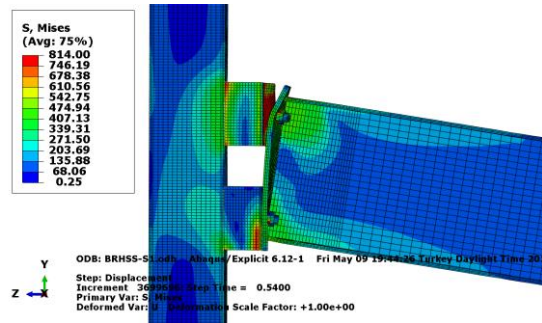


(e)

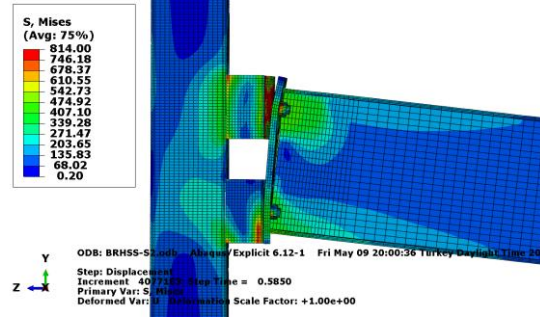


(f)

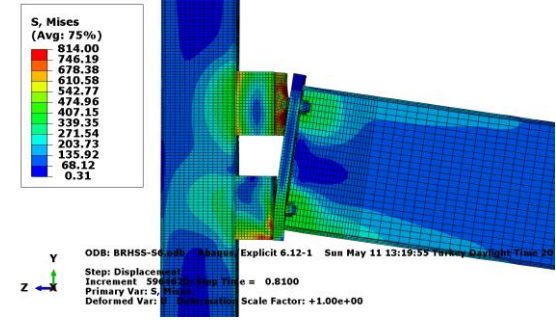
Figure B.7: Von Mises stress distributions of BR-RC joints prior to failure: (a) BR-S1, (b) BR-S2, (c) BR-S6, (d) BR-S7, (e) BR-S11 and (f) BR-S12



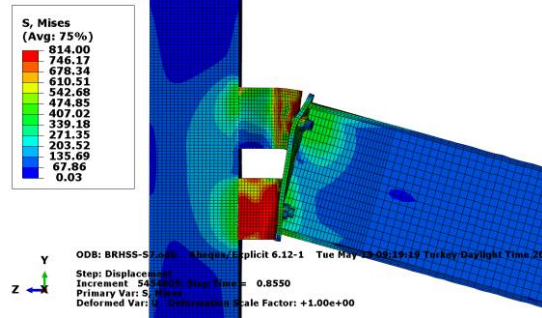
(a)



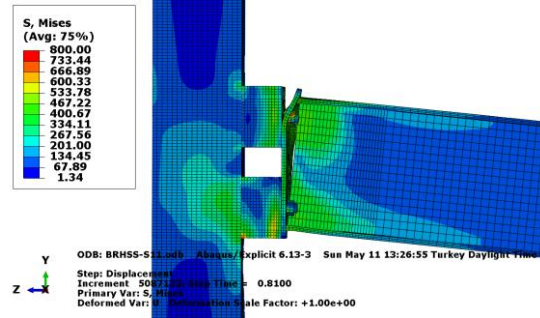
(b)



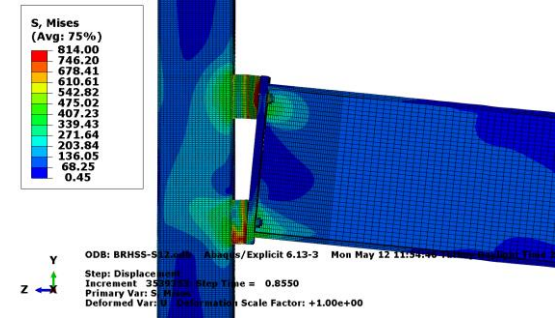
(c)



(d)



(e)



(f)

Figure B.8: Von Mises stress distributions of HSS-BR-RC joints prior to failure: (a) BRHSS-S1, (b) BRHSS-S2, (c) BRHSS-S6, (d) BRHSS-S7, (e) BRHSS-S11 and (f) BRHSS-S12

Appendix C: Dimensionless Forms of Experimental Moment-Rotation Curves with Fitted Models

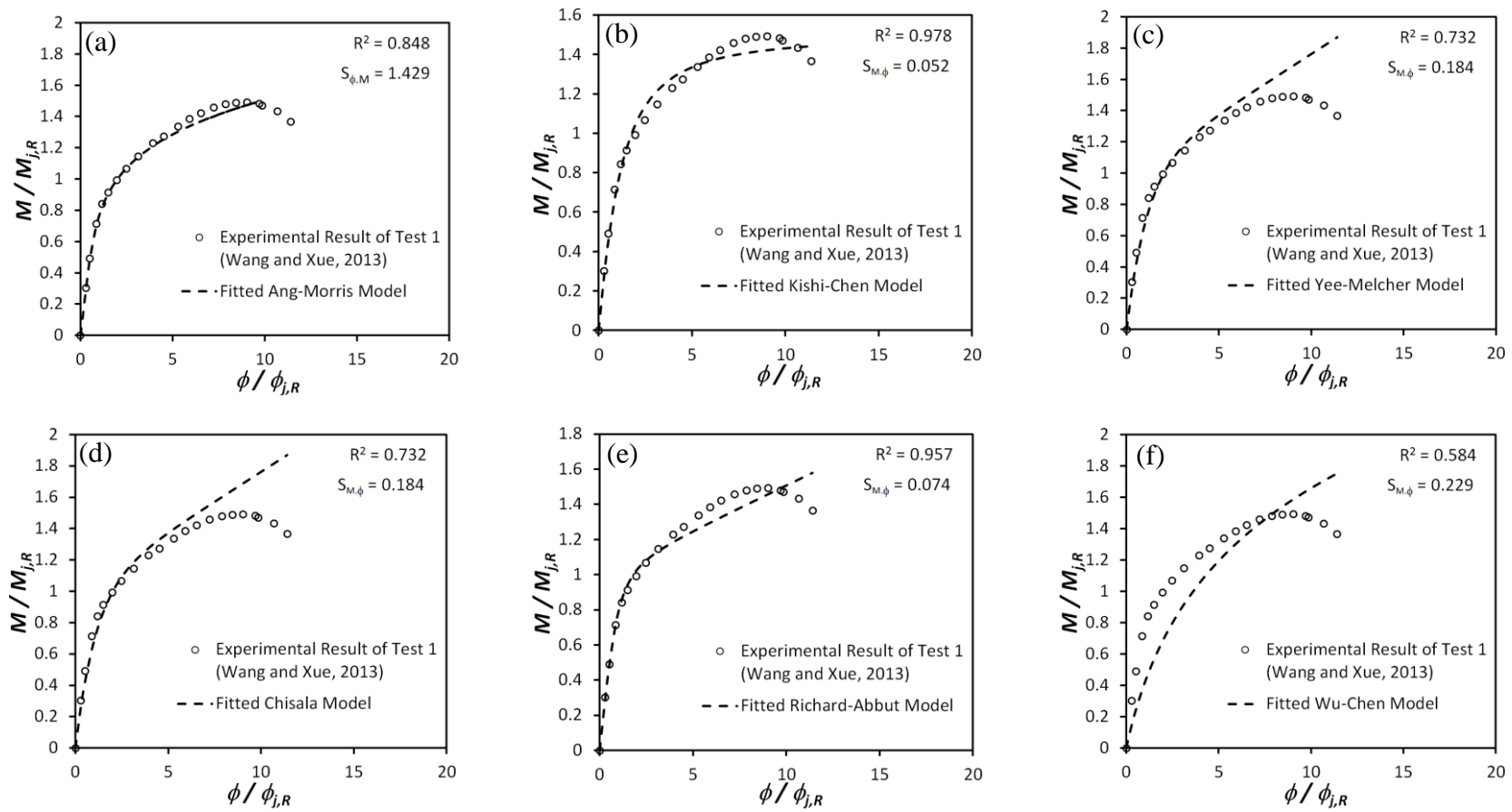


Figure C.1: Normalized moment-rotation curve of Test 1 with fitted models; (a) Ang-Morris Model, (b) Kishi-Chen Model, (c) Yee-Melcher Model, (d) Chisala Model, (e) Richard-Abbut Model and (f) Wu-Chen Model

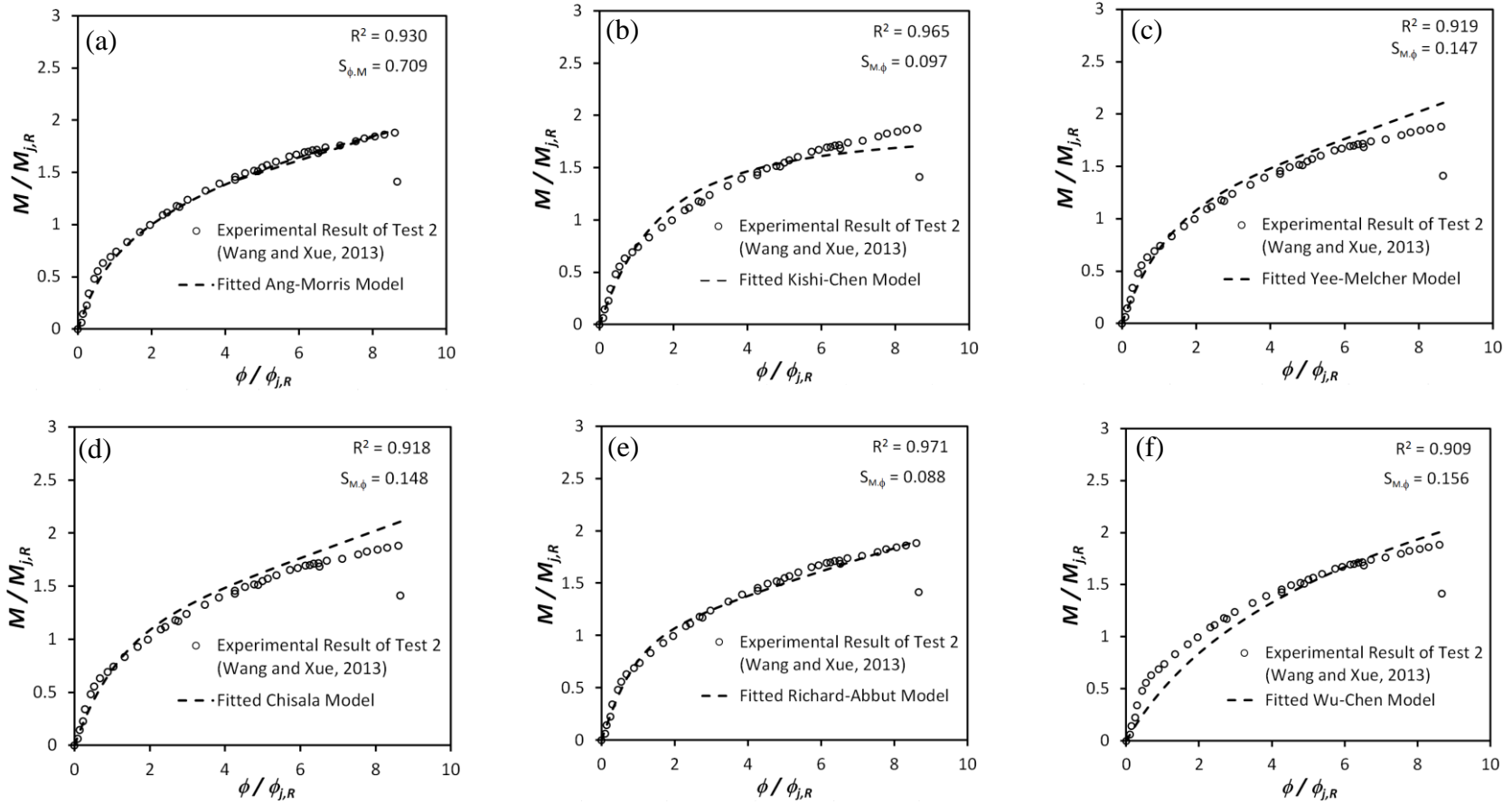


Figure C.2: Normalized moment-rotation curve of Test 2 with fitted models; (a) Ang-Morris Model, (b) Kishi-Chen Model, (c) Yee-Melcher Model, (d) Chisala Model, (e) Richard-Abbut Model and (f) Wu-Chen Model

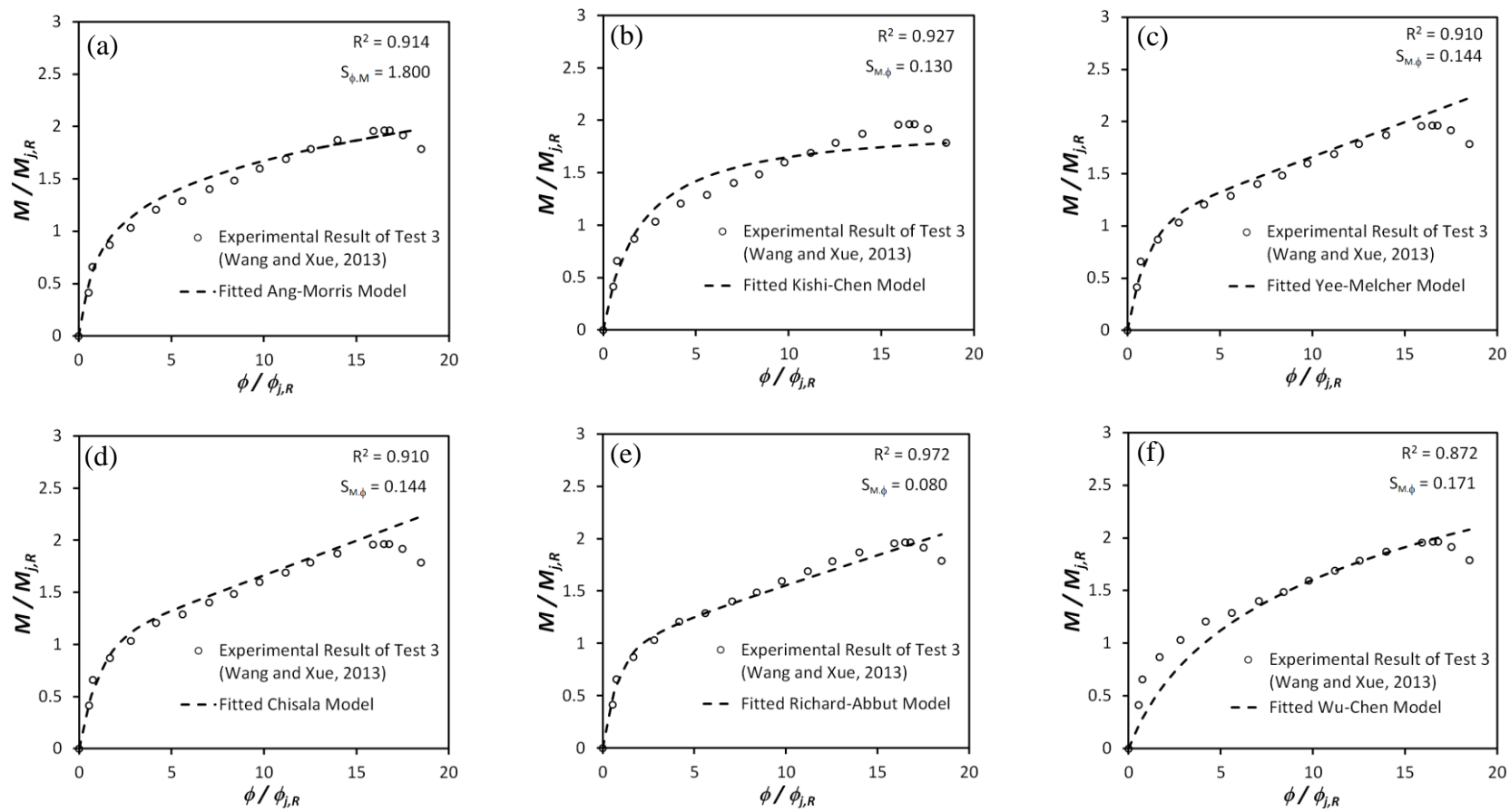


Figure C.3: Normalized moment-rotation curve of Test 3 with fitted models; (a) Ang-Morris Model, (b) Kishi-Chen Model, (c) Yee-Melcher Model, (d) Chisala Model, (e) Richard-Abbut Model and (f) Wu-Chen Model

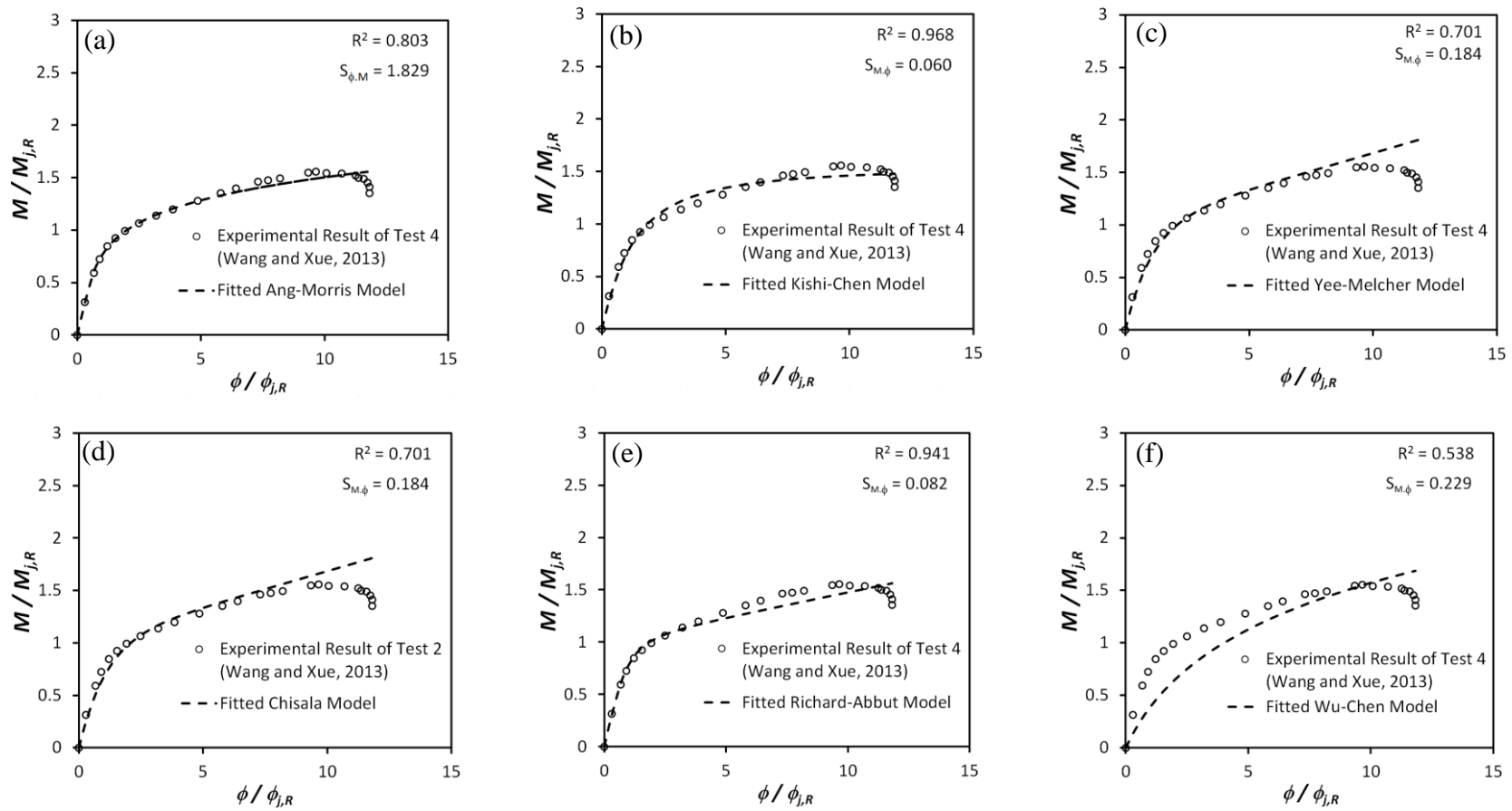


Figure C.4: Normalized moment-rotation curve of Test 4 with fitted models; (a) Ang-Morris Model, (b) Kishi-Chen Model, (c) Yee-Melcher Model, (d) Chisala Model, (e) Richard-Abbut Model and (f) Wu-Chen Model

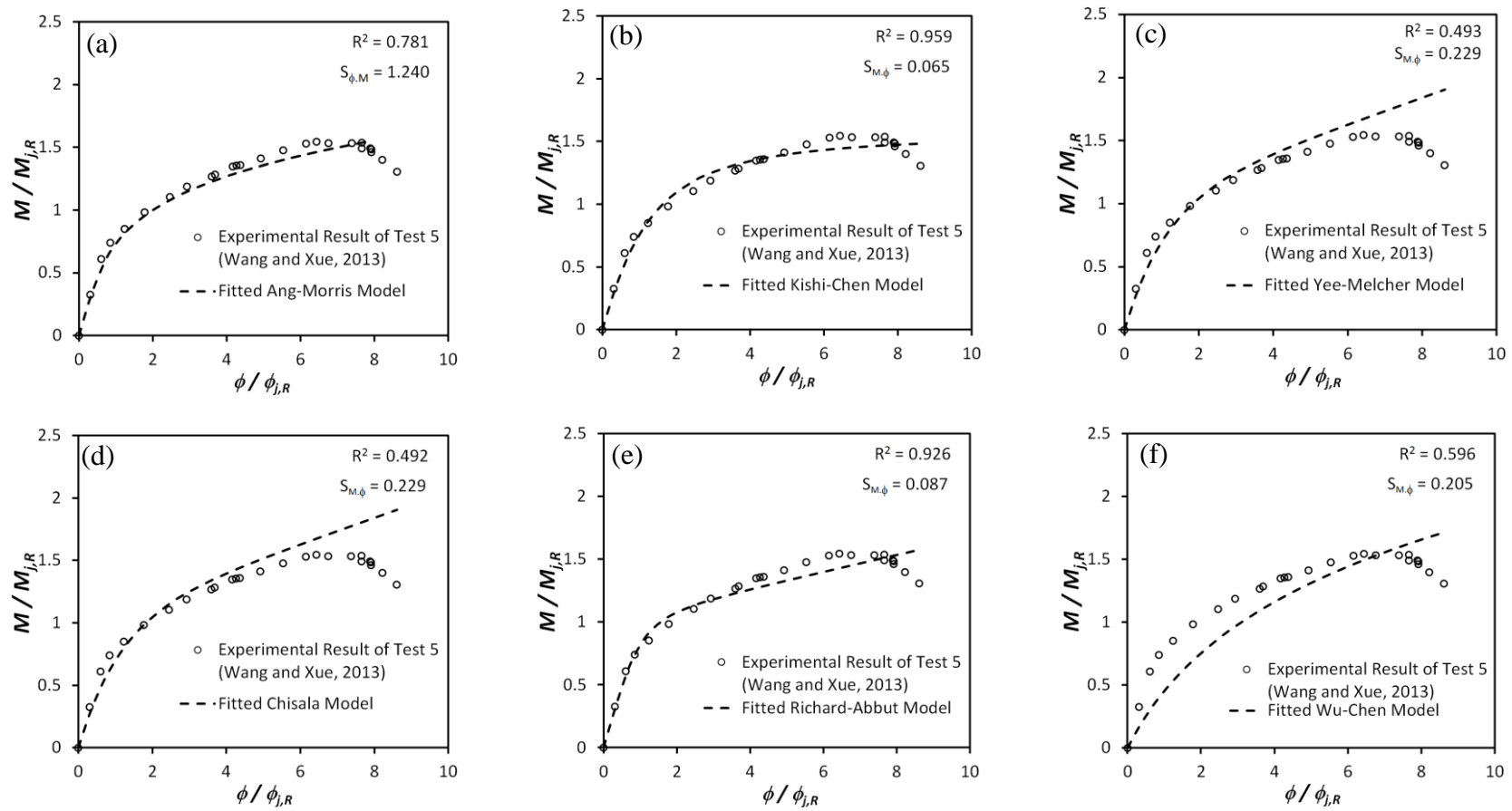


Figure C.5: Normalized moment-rotation curve of Test 5 with fitted models; (a) Ang-Morris Model, (b) Kishi-Chen Model, (c) Yee-Melcher Model, (d) Chisala Model, (e) Richard-Abbut Model and (f) Wu-Chen Model